Friedrich-Alexander-Universität
Erlangen-Nürnberg

Department für Physik
Lehrstuhl für Physik

D I P L O M A R B E I T

Development of an Automatic Response System to Gamma-Ray Burst Alerts for the H.E.S.S. Telescope Array

Tristan Nowak

Eingereicht am: 20. Oktober 2008

Gutachter: 1. Prof. Dr. Christian Stegmann
2. Prof. Dr. Uli Katz

Abstract

Gamma-ray bursts (GRBs) are short, intense flashes of γ-rays, appearing isotropically on the sky. They are the most luminous electromagnetic events that have occurred in the universe since the Big Bang. The detection of GRBs is done by satellite mounted photon detectors, which have an upper energy limit of $\approx 1\,\mathrm{GeV}$ due to their small collection area. For the study of GRBs in higher energies, ground-based experiments have to be used, which take advantage of the Earth's atmosphere as a large detection area. Below 100 TeV, the best observational performance is provided by Imaging Atmospheric Čerenkov Telescopes (IACTs).

The High Energy Stereoscopic System (H.E.S.S.) is an array of four IACTs, situated in the Khomas highland of Namibia. It has a field of view of 5°, and is sensitive to very high energy (VHE) gamma-rays from 100 GeV to 100 TeV. A source with a γ-ray flux of 1% of the Crab Nebula can be detected within 25 hours. With H.E.S.S., GRBs occurring between a declination of 17° and -62° can be observed in VHE γ-rays under good conditions.

Due to the short duration of GRBs in the order of 30 s and the limited field of view of IACTs, H.E.S.S. needs to be forewarned of incoming GRBs by satellite experiments. This is done by NASA's Gamma-Ray Bursts Coordinate Network (GCN) which provides Internet distributed satellite alerts for fast follow-up observations. H.E.S.S. is already capable of a manual reaction to GCN alerts initiated by the shift-crew. Because this reaction needed at least 6 min, an automatic response system for gamma-ray burst alerts has been integrated to the H.E.S.S. data acquisition software. This makes it possible to automatically slew the telescopes to the position of the incoming GRB while at the same time preparing the software for data-taking.

With the first version of this software extension, a total reaction time of $\approx 100\,\mathrm{s}$ after reception of an alert is reached for a GRB onsetting at an angular distance of 30° from the telescopes' momentary pointing position. Future optimizations are possible and will further reduce this time.

Kurzfassung

Gamma-Ray Bursts (GRBs) sind kurze, intensive Ausbrüche von γ-Strahlung, die eine isotrope Verteilung am Himmel aufweisen. Sie stellen die leuchtkräftigsten elektromagnetischen Erscheinungen im Universum seit dem Urknall dar. Ihre Beobachtung erfolgt mit auf Satelliten angebrachten Photonendetektoren, die aufgrund ihrer geringen Größe eine obere Energieschwelle von $\approx 1\,\mathrm{GeV}$ besitzen. Zum Studium von GRBs in höheren Energien müssen bodengestützte Experimente herangezogen werden, die die Erdatmosphäre als große Nachweisfläche für Photonen nutzen. Die beste Beobachtungsleistung unter 100 TeV zeigen dabei Abbildende Čerenkov-Teleskope.

Das High Energy Stereoscopic System (H.E.S.S.) ist ein System von vier Abbildenden Čerenkov-Teleskopen im Khomas Hochland von Namibia mit einem Gesichtsfeld von 5°. Das System kann sehr hochenergetische (VHE) γ-Strahlen mit einer Energie zwischen 100 GeV und 100 TeV beobachten und eine Quelle mit einem Fluss von 1% des Krebsnebels innerhalb von 25 h nachweisen. Mit H.E.S.S. können GRBs, die zwischen 17° und -62° Deklination auftreten, im VHE-Bereich unter guten Bedingungen beobachtet werden.

Wegen der kurzen Dauer von GRBs im Bereich von 30 s und dem eingeschränkten Gesichtsfeld von IACTs ist es nötig, H.E.S.S. über neue Satellitenbeobachtungen von GRBs sofort zu informieren. Diese Aufgabe wird vom NASA betriebenen Gamma-Ray Bursts Coordinate Network (GCN) wahrgenommen, das über das Internet verschickte Satellitenwarnungen für schnelle Folgebeobachtungen zur Verfügung stellt. Eine manuelle, von der Schichtcrew ausgelöste Reaktion auf diese GCN Vorwarnungen ist mit H.E.S.S. möglich. Wegen der langen Reaktionszeit dieser Methode von mindestens 6 min wurde ein System zur automatischen Reaktion auf Gamma-Ray-Burst Vorwarnungen in die Datennahme Software von H.E.S.S. integriert. Damit ist es nun möglich, die Teleskope automatisch auf die Position eines neu aufgetretenen GRBs auszurichten, während die Software gleichzeitig auf die Datennahme vorbereitet wird.

Mit der ersten Version dieser Softwareerweiterung kann ein GRB, der in einer Winkeldistanz von 30° zur aktuellen Beobachtungsposition der Teleskope auftritt, nach etwa $\approx 100\,\mathrm{s}$ seit Empfang der Vorwarnung beobachtet werden.

Contents

List of Figures

List of Tables

1 Introduction

Mankind has curiously watched the stars on the night sky since the dawn of human history. Eventually, the desire to understand their nature induced the search for optical instruments which would help to gather even more information about them than it was possible with the naked eye alone.

After many centuries, this led to the construction of the first refracting telescope by Hans Lippershey and Zacharias Janssen in 1608 and one year later, Galileo Galilei used their plans to build his own greatly improved, twenty-one-powered version, as seen in Figure 1.1, with which he was able to discover the four largest moons of Jupiter. This discovery clearly disproved the up to then well-established doctrine of a geocentric universe, which claimed that all objects in space had to orbit Earth at increasingly larger radii, and let to a rising acceptance of the heliocentric theory, which posited that the planets revolved around the sun and the moons around their planets.

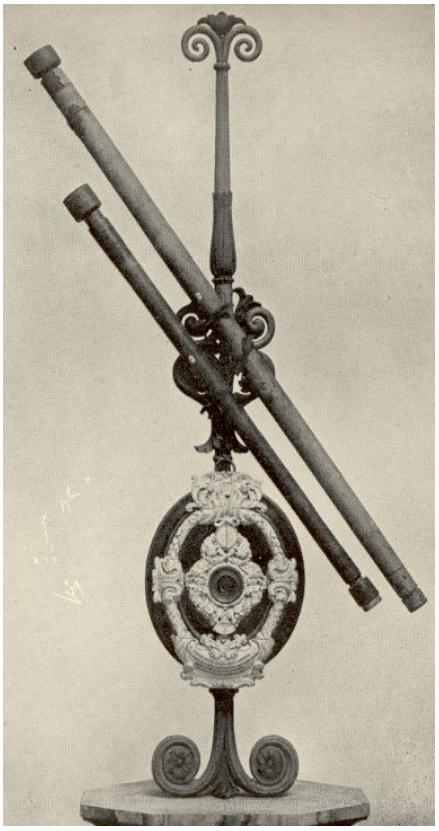

Fig. 1.1: *Galileo Galilei's famous self-constructed refracting telescopes from 1609, the smaller one being the more advanced with a 21-fold magnification*

Galilei also exchanged letters about his findings with Johannes Keppler, who analysed Tycho Brahe's precise observations of the planetary orbits and discovered their elliptical nature. Keppler also invented a new kind of refracting telescope in 1611, which had two convex lenses and a much wider field of view than Galilei's model. A few decades later, Keppler's design was realized in the first large astronomical telescope by Christiaan Huygens, with which he discovered the Saturn moon Titan in 1655 and inaugurated a new era of instrument supported astronomy.

The following Sections feature a short introduction of the astronomical field which then emerged as a natural extension of optical astronomy, the observation of the sky in invisible wavelengths, and concludes with the motivation behind this work.

1.1 Non-Optical Astronomy

With steadily improving technology it was soon possible to observe and study astronomical objects in wavelengths outside the visible range. This was pioneered in 1937, when Grote Reber built the first parabolic dish radio telescope and conducted the first sky survey in radio waves. Radio astronomy made it possible to observe objects invisible to optical telescopes, such as radio galaxies, pulsars and the Galactic center and to complement data

to already visible objects such as quasars and blazars.

The observation of ultraviolet (UV) light was more difficult, because only the near ultraviolet with wavelengths longer than 300 nm can penetrate the atmosphere, which absorbs smaller wavelengths before they reach the ground. The far UV spectrum could thus only be effectively observed from space. The first dedicated UV satellite was launched with the International Ultraviolet Explorer in 1978, which did an extensive sky survey in the ultraviolet spectrum for 18 years.

At even higher photon energies, ground-based telescopes cannot be used for direct observation, as the photons are entirely absorbed in the atmosphere, requiring the use of balloon or satellite experiments. The first astronomical observations in X-rays were conducted with sub-orbital rocket flights, already detecting X-rays from the Sun in 1948. Still using rocket mounted experiments the first two galactic X-ray sources, Scorpius X 1, a low mass binary system and the Crab Nebula, a supernova remnant, were discovered shortly after each other in 1962.

In 1970 Uhuru, the first satellite built exclusively for X-ray observation was launched. With its help the first extensive sky survey in X-rays was conducted, which led to the detection of 300 new sources in this wavelengths. Succeeding this experiment, satellites with increasingly advanced instrumentation were launched: EXOSAT in 1983, ROSAT in 1990 and Chandra and Newton in 1999.

1.2 Gamma-Ray Astronomy

In order to gain insight in the most violent events in the universe, such as supernovae, giant black holes accreting mater, pulsar wind nebulae and others, the observation of even higher energetic radiation is desirable, because whenever charged particles are accelerated to very high kinetic energies, photons in the gamma energy regime[1] are produced. This had been theoretically predicted long before cosmic rays were detected by Victor Hess in 1912 in his famous balloon experiments.

It was also posited, that the spectrum of these gamma-rays should resemble the spectrum of the charged particles producing them. As gamma-rays are not deflected by intergalactic magnetic fields and keep their directional information, their observation would open a new window to the high-energy universe.

1.2.1 Above the Atmosphere

Gamma-ray astronomy began with NASA's Explorer XI satellite launched in 1961, which detected 22 gamma-ray events during its mission time of four months, seemingly originating from random locations, implying an uniform gamma-ray background, which was expected from the interaction of high-energy particles with interstellar gas.

The OSO-3 satellite, which among others also carried a gamma-ray detector, was the first to detect solar flares as a localized source in these wavelengths. In 1972 the first dedicated gamma-ray satellite, NASA's SAS-2[2], was launched. During its short lifetime of only seven months it collected data from 55% of the sky including almost the whole Galactic plane. By this means it detected several new sources and measured the diffuse gamma-ray background.

Three years later in 1975, ESA's COS-B satellite, which could detect photons in the

[1] $E \gtrapprox 500\,\mathrm{keV}$

[2] Small Astronomy Satellite 2

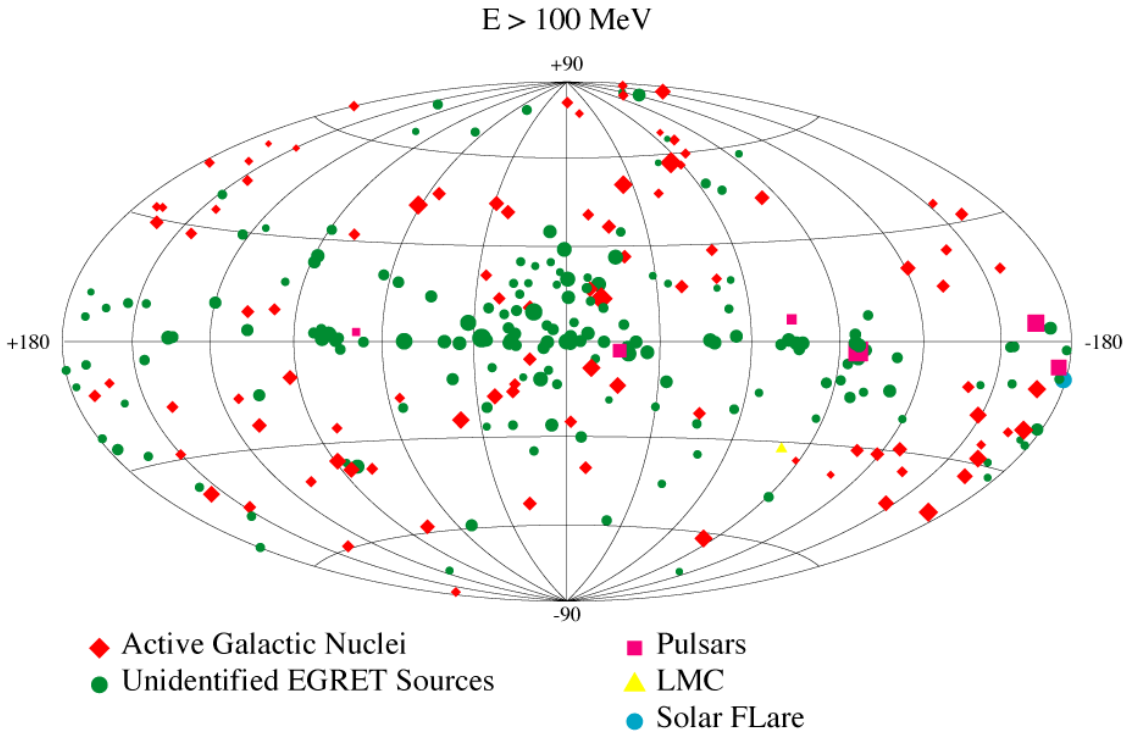

Fig. 1.2: *Sky-map of the Third EGRET Catalog[1], showing 271 gamma-ray sources*

range of 30 MeV to 5 GeV, was launched and detected 25 sources, compiling a first gamma-ray map of the sky.

With the Compton Gamma Ray Observatory (CGRO) that was launched in 1991, harboring four experiments, another milestone for gamma-ray astronomy was set. One of its instruments was the Energetic Gamma Ray Experiment Telescope (EGRET), which was sensitive from 20 MeV to 30GeV and detected 271 gamma-ray sources, depicted in Figure 1.2.

1.2.2 Ground-Based

Besides the direct observation of gamma-rays via satellites and balloons, another technique is the detection of secondary particles created by gamma-rays upon impact on the Earth's atmosphere. This mode of indirect observation takes advantage of the fact that gamma-ray photons and high energy hadronic particles colliding with atmospheric molecules produce a subsequent air shower of secondary particles, as schematically shown in Figure 1.3. This process will be further elaborated in Chapter 3. Information about these secondary particle showers can be acquired by ground based experiments in several ways. Among them one can distinguish between Extensive Air Shower (EAS) Arrays and Imaging Atmospheric Čerenkov Telescopes (IACTs).

Imaging Atmospheric Čerenkov Telescopes

This technique, which will be described in detail in Chapter 3, involves the imaging of the particle showers produced by very high energy[3] (VHE) photons upon impact on the

[3]The term very high energy (VHE) is commonly used in gamma-ray astronomy, although it is not precicely defined. In this work, VHE denotes energies above 10 GeV

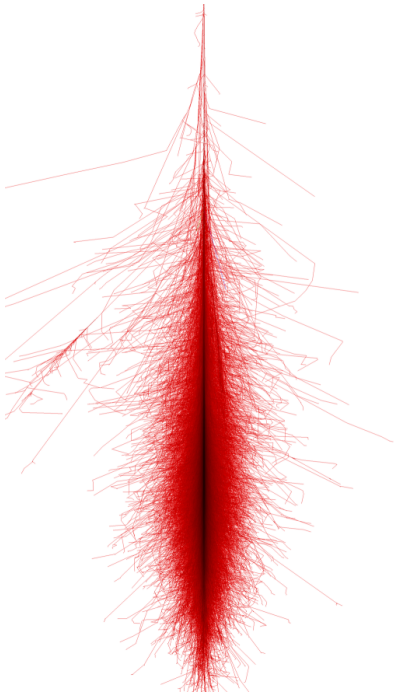

Fig. 1.3: *Simulated air shower generated by a 1 TeV photon*

atmosphere. The imaging is done with parabolic or spherical mirror dishes focusing the visible blue Čerenkov light emitted by the particles in the shower on high sensitive cameras. From these images the direction and energy of the incident gamma-ray photons can be reconstructed. The quality of the information gained in this process depends on many factors, some of which are listed in the follwing:

- The altitude of the experiment
- The clearness of the atmosphere
- The number of telescopes that imaged the same event
- The sensitivity of the cameras
- The angle under which the shower was observed
- The energy of the primary particle

The minimum energy threshold of IACTs depends on the quality of the data extractable from the showers. When, for example, the energy of the primary particle does not exceed a certain minimum, which varies with the sensitivity of the cameras, the particle's direction, and other factors, it cannot produce a shower which can be imaged with sufficient quality. Today's state-of-the-art experiments have a minimum energy threshold of around 50 GeV, while the next generation IACTs, which will soon be completed[4], are designed to achieve thresholds as low as 20 GeV.

The first two experiments utilizing this technique were the Whipple Collaborations's 10 m diameter mirror dish telescope on Mount Hopkins in Arizona, which detected the Crab Nebula as the first VHE γ-ray source in 1989 and shortly thereafter HEGRA[5], located at Roque de los Muchachos Observatory on La Palma, consisting of six dish telescopes, each with a diameter of 3.9 m.

[4] e.g. H.E.S.S. Phase II described hereafter
[5] High-Energy-Gamma-Ray Astronomy

The Whipple telescope provided the first detection of an astrophysical gamma-ray source, the Crab Nebula, using this technique while the HEGRA experiment demonstrated, that arrays of IACTs provide a further increase in sensitivity and in angular and energy resolution. HEGRA was dismantled in 2002 in favor of two follow-up experiments, one on the northern and one on the southern hemisphere.

The HEGRA successor on the northern hemisphere is MAGIC[6], which was built on the same site like HEGRA. With its 17 m diameter mirror dish, comprised of rectangular mirrors making up an area of 240 m^2, it is still the largest IACT in the world. Its light-weight carbon fiber frame construction reduces the overall weight to 40 tons and allows the slewing to any target in less than 40 seconds. At the moment a second telescope, MAGIC 2, is built 85 m from the first one and will be completed shortly.

The second follow-up experiment of HEGRA on the southern hemisphere is H.E.S.S.[7], an array of four 13 m Čerenkov telescopes, located in the Khomas highlands in Namibia at an altitude of 1800 m. Its first telescope was operational in Summer 2002 and in December 2003, the whole array was completed. H.E.S.S. was the first experiment to spatially resolve a source of VHE gamma-rays in 2004. In 2005, H.E.S.S. detected eight new sources of VHE γ-rays in the inner part of the Milky Way, doubling the number of known sources in this energy range. The H.E.S.S. telescope array will be presented in detail in Chapter 3.

Currently the H.E.S.S. collaboration is on the way of finishing its newest project, H.E.S.S. Phase II, an improvement of the telescope array in the form of a fifth large 25 m diameter telescope, which will both lower the arrays energy threshold and increase its sensitivity.

Another experiment on the southern hemisphere is the CANGAROO[8] I 3.8 m telescope, which is in operation since 1992 and discovered 4 new sources of 10^{12} eV gamma-rays. Its latest successor, the CANGAROO III project completed in 2004, encompasses an array of four 10 m Čerenkov telescopes in the Australian Outback.

On the northern hemisphere, the VERITAS[9] telescope array has been built in Amado, Arizona. It consists of four telescopes with 12 m diameter dishes, each containing 350 mirrors. The first telescope is operational since 2005 and data-taking with the full array began in the spring of 2007.

Extensive Air Shower Arrays

Another method to gather data from air showers induced by γ-rays and other highly energetic cosmic-ray particles, is to use light sealed water tanks on the ground. When a secondary particle from the air shower hits such a tank, it can penetrate its walls and will produce Čerenkov light within the water tank, in case its velocity is higher than local speed of light. This can be detected and the acquired information is used to reconstruct the energy and direction of the secondary particle from the shower.

With enough directional and energetic information about the secondary particles of a single air shower, it is then also possible to reconstruct the energy and direction of the primary particle which created it.

As these kinds of experiments require some of the secondary particles[10] to reach the ground, they have a – compared to IACTs – large minimum energy threshold in the order of 100 TeV. As the flux of gamma-ray photons at these energies is typically very low

[6] Major Atmospheric Gamma-ray Imaging Čerenkov (Telescope)
[7] High Energy Stereoscopic System
[8] Collaboration of Australia and Nippon for a GAmma Ray Observatory in the Outback
[9] Very Energetic Radiation Imaging Telescope Array System
[10] mostly light-weight leptons (electrons, positrons, muons, etc.)

compared to the flux of hadronic cosmic ray particles, EAS Arrays prevalently observe the latter, which are mostly comprised of protons.

A very early EAS array was built in Haverah Park near Harrogate, North Yorkshire, a research site operated by the Physics Department of the University of Leeds. From 1967 until 1987 it was home to one of the largest EAS arrays in the world with an area of 12 square kilometers surrounded by four water Čereknov detectors. During its lifetime four exceptionally big air showers only producable by particles of energies greater than 10^{20} eV were detected, starting much discussion as these values were not explainable by any known mode of acceleration.

In February 1997 the Milagrito experiment was started. It consisted of a single 80 meters long water tank located at an altitude of 2630 m in northern New Mexico, and served as a prototype for its larger successor Milagro. As detectors for the Čerenkov light it contained 228 submerged photomultiplier tubes (PMTs) at a water depth of between one and two meters.

Its follow-up experiment Milagro, which is seen from the inside in Figure 1.4, has two layers of PMTs in the same water tank, a field of view of 2 sr and a duty cycle of over 90%. A sparse array of 175 "outrigger" 4000 liter water tanks, each with a PMT, was added in 2002, which extends the physical area of Milagro to 40000 m^2.

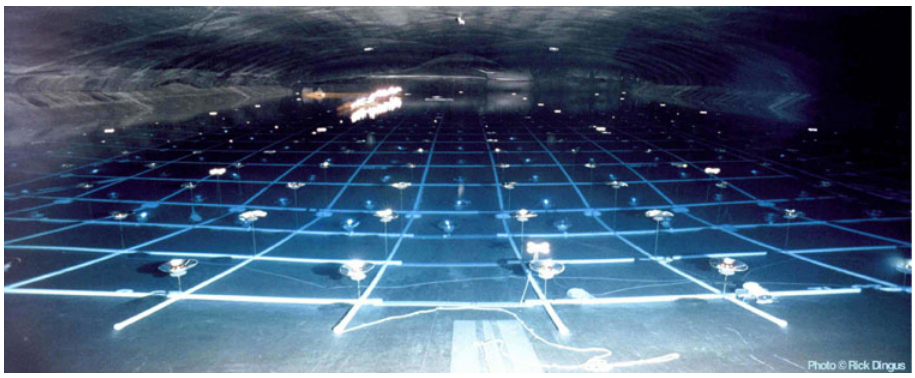

Fig. 1.4: *Inside of the Milagro water tank with inflated cover and visible lines of PMTs*

Currently the largest experiment in this field is the Pierre-Auger-Observatory located on the plain of Pampa Amarilla, near the town of Malargüe in Mendoza Province, Argentina. On 3000 km^2, it harbors 1600 water tanks, each having a volume of 12000 l and containing three large PMTs. As a hybrid experiment it additionally employs four atmospheric fluorescence detectors. These are used to observe and track trails of fluorescence light being produced as charged particles in an air shower interact with atmospheric nitrogen, causing it to fluoresce in ultraviolet light. The concept of the experiment is depicted in Figure 1.5.

1.3 Observing Gamma-Ray Bursts with Čerenkov Telescopes

With BATSE[11] the Compton Gamma-Ray Observatory also carried an experiment solely devoted to the detection of gamma-ray bursts (GRBs), a class of very high-luminosity γ-ray emitting transients of short duration, whose physical background still bears many unanswered questions.

[11] Burst and Transient Source Experiment

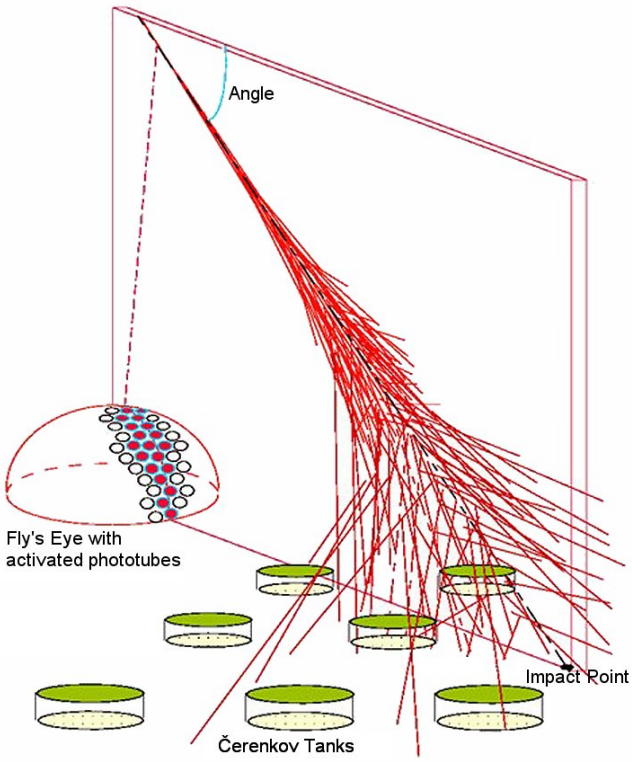

Fig. 1.5: *Conceptual design of the Pierre Auger Observatory. Fluorescence detectors overlook an array of water-Čerenkov detectors*

Today many well-established theories associate them partly with ultra-energetic supernovae and party with cataclysmic merger events in binary systems. Some GRBs are known to have occurred over 13 billion years ago, when the universe was still very young, only a few hundred million years old. This makes their study a very promising objective both for the understanding of these violent cosmic phenomena and the evolution of the universe after the Big Bang.

Currently data about GRBs is gathered by NASA's Swift satellite, launched in 2004, and most recently by the Fermi Gamma-Ray Space Telescope (Fermi)[12]. Unfortunately, satellites can only effectively observe GRBs in the energy range below 10 GeV, as the gamma-ray flux above this energies is generally much too low for their small detector areas[13] to collect enough photons.

So in order to observe GRBs in the very high energy regime, a technique involving huge detector areas has to be used. At sufficient energies, this can be achieved by using the Earth's atmosphere as a giant detector area for ground-based gamma-ray experiments.

Taking the power-law flux of most GRBs into account, a detection of gamma-rays in the lower VHE regime, i.e. in the order of 30 GeV to a few TeVs, is considered to be more likely than a detection in the high TeV range. On that account Atmospheric Čerenkov Telescopes with their lower minimum energy, higher sensitivity and much better directional accuracy compared to ground-based EAS arrays are currently the best choice for observing GRBs in very high energies.

However, due to the very short duration of GRBs in the order of 30 s and the rather

[12] formerly known as Gamma-Ray Large Area Space Telescope (GLAST)
[13] in the order of $1\,m^2$

Fig. 1.6: *Aerial view of the H.E.S.S. telescope array, arranged on a square with 120 side length*

narrow field of view of IACTs of a few angular degrees, the observation sites on the ground need to be informed of an onsetting burst immediately by satellite mounted instrumentation with a much wider field of view. The IACT's reaction to these alerts, i.e. the slewing to the location of the GRB and preparing of the data acquisition, should be as fast as possible, preferably in less than one minute, considering the timescale of the bursts.

NASA's Gamma-Ray Bursts Coordination Network, which will be described more detailed in 2.1.2, has been established in 1993 and is since then distributing satellite GRB alerts to sites on the ground.

Among the IACTs on the northern hemisphere, the MAGIC Telescope is already capable of a fast automatic reaction to these alerts, this ability being incorporated in its lightweight design from the start.

On the southern hemisphere, the H.E.S.S. telescope array, seen in Figure 1.6, is also capable of processing GCN alerts. When an alert is received, it is checked whether it is observable under sufficiently good conditions. This includes, among others, that the location of the GRB is observable under a reasonable zenith angle and that enough observation time is left in the night of the alert. If the criteria are met, the shift crew on site gets informed by an audio message and has to react manually. This human reaction consists of a number of usually relatively slow steps in comparison to an automatic system:

1. The deliberation whether or not to observe the GRB, which is usually the bottleneck of the whole procedure ($\approx$ 1 - 10 min)
2. In case of uncertainties, a phone call to the current GRB expert
3. The stopping of the current observation ($\approx$ 2.5 min)
4. The entry of the new GRB target to the database of the controlling data acquisition (DAQ) software ($\approx$ 0.5 - 5 min, depends on the shift crews experience)
5. The scheduling and starting of a new observation run ($\approx$ 1 min)

As the fastest reaction reached with this manual approach has been 6 min 31 s between reception of the alert and observation of the target, an automatic response system would pose a significant improvement.

Although this has not been initially included in the design of H.E.S.S., a fast automatic reaction to external alerts is hardware- and software-wise viable and can be incorporated smoothly in the H.E.S.S. modular DAQ software.

This work will present the software changes necessary to allow for the possibility of an automatic reaction to external satellite alerts, followed by a detailed review of several simulated automatic alert observations with the modified software. Additionally, a preceding introduction to gamma-ray bursts and the H.E.S.S. telescope array will be given in the next Chapters.

2 Gamma-Ray Bursts

Gamma-ray bursts are sudden flashes of gamma-rays appearing at seemingly random positions on the sky. They are the most luminous electromagnetic events still occurring in the universe since the Big Bang. The first of these events was observed in 1967 by the US Vela nuclear test detection satellites launched by the United States Air Force. These satellites were originally designed to monitor compliance with the Nuclear Test Ban Treaty by searching for earth-bound gamma-ray emission, which would occur during the explosion of nuclear weapons. Instead they detected flashes of gamma-rays originating from space, whose signature did not fit to that of a nuclear explosion, and thus discovered a new cosmic phenomenon.

However, because of security concerns, it was not until 1973 that Ray Klebesadel, Ian Strong and Roy Olson[2] of Los Alamos National Laboratory published their discovery, reporting 16 GRBs that occurred between July 1969 and July 1972.

With the CGRO/BATSE experiment[1] operated between 1991 and 2000, which detected 2704 bursts during its lifetime, much progress regarding the exploration of GRBs was made.

In 1996, BATSE became support by the Italian-Dutch satellite BeppoSAX, mainly intended for X-ray observations, but also carrying instruments for the detection of gamma-ray bursts.

After the HETE[2] satellite, whose primary objective was the multiwavelength observation of GRBs with UV, X-ray and gamma-ray instruments, was lost due to a miscarried launch, its successor HETE-2 was put into orbit in 2000. Its scientific payload has been designed mainly for the detection of GRBs as well as the fast calculation and distribution of their coordinates.

Although HETE-2 is still operational, most GRBs are currently detected by NASA's Swift satellite, whose BAT[3] instrument has a wide field of view of up to 4 sr, a sensitivity about three times higher than BATSE and the ability to slew on target within 100 s for rapid follow-up observations. Swift's instruments are covering the optical, ultra-violet, X-ray and gamma-ray range and allow observation up to photon energies of 150 keV. Swift has detected over 370 GRBs until August 2008.

The following Chapter will describe the phenomenon of GRBs, followed by a brief introduction to the theoretical models regarding their progenitors.

2.1 Means of Detection

Although there are theoretical calculations indicating the onsetting of around 500 GRBs per day in the whole universe, current instruments observe just about one GRB per day. Today, this has accumulated to over 3000 satellite detections, of which Table 2.1 shows an assortment of the most interesting.

[1] see Sections 1.2.1 and 1.3
[2] High Energy Transient Explorer
[3] Burst Alert Telescope

In this Section, the different techniques of detecting GRBs will be described along with NASA's Gamma-Ray Bursts Coordination Network, the forewarning system addressed in Section 1.3 needed for ground-based telescope systems with limited field of view for a fast slewing to onsetting GRBs.

2.1.1 Instruments

Since, as mentioned in Section 1.2, gamma-rays are thoroughly absorbed during their traversal through the Earth's atmosphere, the direct detection of gamma-ray bursts is only possible from above the atmosphere. This is done via Earth orbiting satellite experiments introduced before, equipped with high-energy photon detector planes. Because of their relatively small detection area, the upper limit for space-based detection is about 1 GeV.

At higher energies, ground-based detection becomes possible both with IACTs and EAS Arrays[4]. EAS Arrays have a very wide field of view and a generally high duty circle, which enables them to permanently monitor a large fraction of the sky. However, their minimum energy threshold is about 100 times higher than with IACTs and their sensitivity for gamma-rays at these energies is comparingly low. This requires GRBs to emit gamma-ray photons with a sufficient flux at several TeV to be detectable before the hadronic cosmic-rays background.

On that account IACTs with their lower minimum energy threshold and higher sensitivity for gamma-rays are thought to have a higher chance of a successful GRB observation in the VHE regime, as already mentioned in Section 1.3, although at the moment, no GRB signal with sufficiently high significance for a doubtless detection has been found with either of these methods.

2.1.2 The Gamma-Ray Bursts Coordination Network

The Gamma-Ray Bursts Coordination Network (GCN) has been established in 1993 under the name BACODINE, standing for BAtse COordinates DIstribution NEtwork, because at that time only CGRO/BATSE bursts where handled. The GCN serves two purposes. On the one hand, it provides the fast coordinates distribution of onsetting GRBs seen with satellite experiments to ground sites that registered themselves for reception (GCN Notices). On the other hand it also serves as a central administrating and distributing instance for GRB follow-up observation reports (GCN Circulars).

In the very beginning the alerts where only spread with telephone calls, however, Internet distribution methods like e-mail and TCP/IP socket connections were quickly made possible and are the most popular technique today. With time, more experiments beside BATSE were included, some of which have in the meanwhile exceeded there lifetime. Yet, there is a large number of space-bound instruments connected to the GCN service, a list of which is given in Table 2.2.

If one of the experiments connected to the GCN service receives data from a GRB, its location and other relevant data is sent to a central processing station on the ground, often through different relay satellites. Subsequently the information, including the GRB's right ascension (RA) and declination (Dec), the positional error and the time of onset, is distributed to all participating sites as a "GCN Notice" via various channels, as the sketch in Figure 2.1 indicates.

The ground-based observation sites can then react according to the information they received. Possible reactions are follow-up observations of the GRB in various wavelengths. Short descriptions about these can be sent back to the GCN, which in turn archives and

[4] see Sections 1.2.2

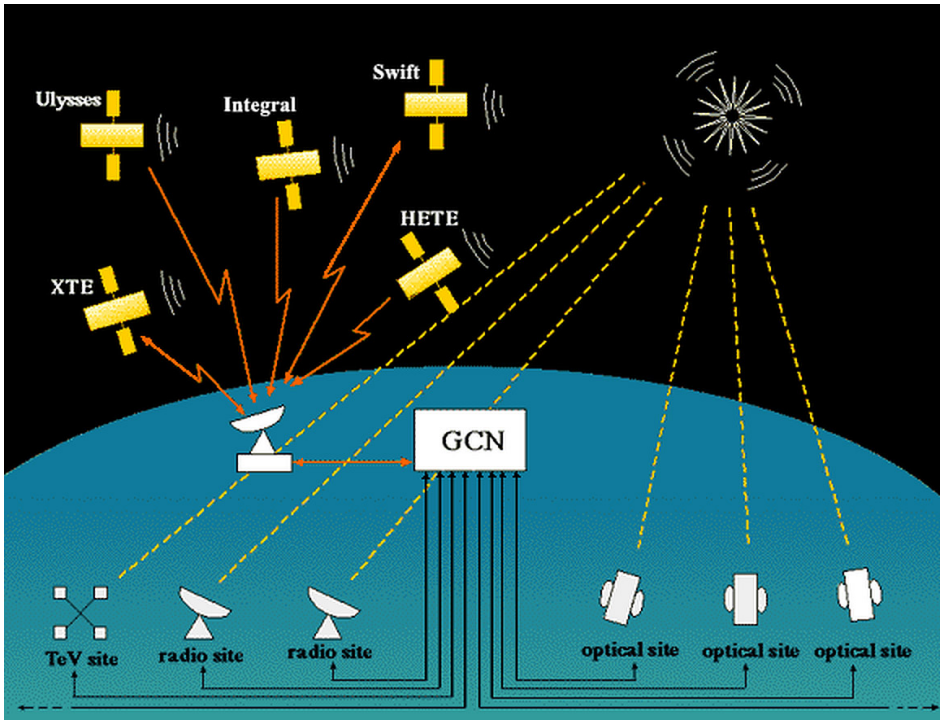

Fig. 2.1: *Alert message distribution with the Gamma-Ray Bursts Coordination Network*

distributes them to the community as "GCN Circulars" by means of e-mail lists, thus helping to coordinate further follow-up observations and other scientific efforts.

The time that passes between the onset of a GRB and the arrival of the positional information at the distributing nodes is highly dependent on the design of the different experiments and the relay stations in space and on the ground that have to be used for the transmission. With Swift, for example, the maximum delay between these stage lies between 13 s and 30 s , although its predecessor BATSE featured a much faster distribution of maximal 5.5 s. In turn, BATSE's accuracy of the GRB location in this alert messages could be as bad as 10°, whereas with Swift it is usually not worse than 3 arc minutes.

Most GCN Notices that are sent out today are alerts from Swifts Burst Alert Telescope. This could, however, change when the Fermi experiment is fully operational.

2.2 Duration and Classification

As there is no obvious way to measure the exact duration of a high energy transient[5], the BATSE[6] team introduced T_{90} as the time interval between 5% and 90% of the observed signal events. Applying this definition, the duration of GRBs reaches from a few milliseconds to several minutes, with rise times as fast as 10^{-4} s. A recorded exception has been GRB 060218 with a burst duration of 33 minutes.

A T_{90}-duration-quantity plot, as seen in Figure 2.2 for the BATSE 4 B Catalog[14], reveals an asymmetric distribution of GRBs regarding their duration. This together with the spectral properties led to a classification scheme[15], which divides GRBs into short gamma-ray burst (sGRBs) with a duration of less then 2 s, with an average of about 0.3 s,

[5] an astronomical event only temporary observable
[6] see Section 1.3

Denotation	Description
GRB 670702	First observed GRB, detected by the Vela satellites[2].
GRB 970228	Detection and first afterglow observation in X-rays by BeppoSAX. Follow-up observations were done in the optical range by telescopes on the ground, its position being found coincident with a faint galaxy[3].
GRB 970508	First GRB with a measured red shift of $z = 0.835$, confirming an extra-galactic origin[4].
GRB 971214	Very bright GRB with $z = 3.4$ initially thought to be the most energetic cosmic event ever observed. Later this was abandoned in favor of a more likely Earth directed, anisotropic jet emission modell[5].
GRB 980425	First GRB associated with an observed Supernova[6], SN 1998bw of type Ic, which has been discovered simultaneously within the BeppoSAX error-box. Currently still the nearest observed GRB with a redshift of $z = 0.0085$ and low luminosity.
GRB 990123	Optically brightest afterglow prior to GRB 080319B despite a redshift of $z = 1.6$. First detection of the optical afterglow within the T_{90} burst duration(see 2.2).
GRB 030329A	Very close and bright GRB with $z = 0.168$[7] and strong spectral similarities to core-collapse supernovae[8]. Its apparent luminosity was enough to ionize the upper atmosphere[9].
GRB 050509B	First Swift detection of a short GRB with position measurement accurate within within 9.3 arcseconds, sufficient for association with an elliptical galaxy cluster at $z = 0.225$[10].
GRB 050904	Most distant GRB ever observed to date, with a redshift of $z = 6.295$[11], corresponding to a distance of about 13 billion light-years.
GRB 060218	Exceptionally long burst time of $T_{90} \approx 2000\,\mathrm{s}$ and unambiguous association with SN 2006aj[12].
GRB 080319B	GRB with unprecedented intensity and the currently brightest observed optical afterglow, peaking at a magnitude of 5, thus visible with the naked eye[13]. Most luminous optical source ever observed to this date.

Table 2.1: *An assortment of notable GRBs from 1967 until 2008. The denotation system for GRBs is "GRB YYMMDD", where YYMMDD states the burst's date of occurrence. If there are several bursts on one day, the letters "A,B,C" and so forth are added to the name.*

Instrument	Description
Agile	Italian gamma- and X-ray satellite (Astrorivelatore Gamma ad Immagini LEggero). Alerts from the SuperAGILE instrument are handled.
IPN	The Interplanetary Network (IPN) is a group of spacecrafts (e.g. Swift, Ulysses, WIND) triangulating results from their gamma-ray detectors to localize GRBs.
INTEGRAL	ESA gamma-ray satellite (International Gamma-Ray Astrophysics Laboratory). Alerts from two instruments are handled (ISGRI, ACS)
Fermi	NASA's new Fermi Gamma-Ray Space Telescope. Alerts are handled for two instruments (LAT,GBM)
Swift	NASA GRB detection satellite. Alerts from all three instruments are processed (BAT, XRT, UVOT).
RXTE	NASA X-ray satellite (Rossi X-Ray Timing Explorer). Alerts are handled for two instruments (PCA, ASM)

Table 2.2: *List of current experiments affiliated with the GCN*

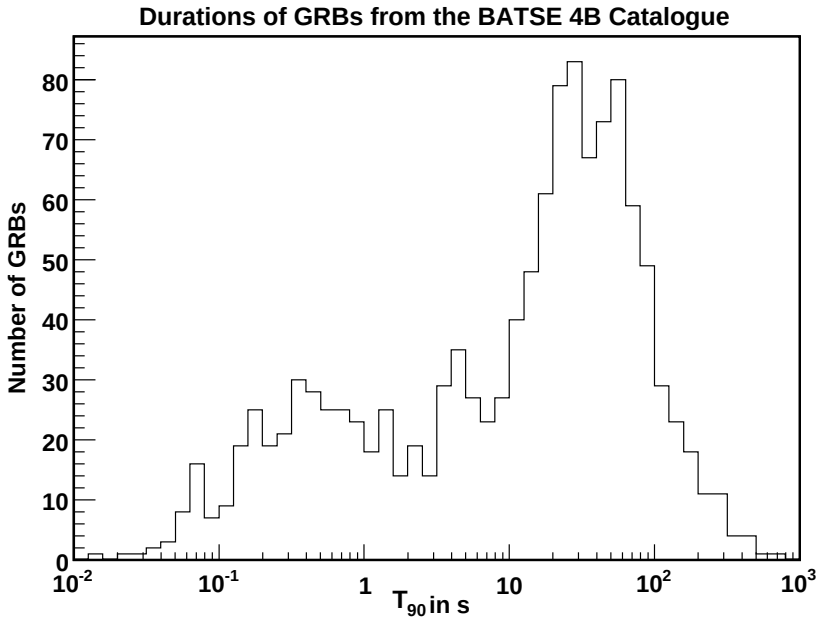

Fig. 2.2: *Number of GRBs over* T_{90} *duration for all GRBs from the BATSE 4 B Catalog*

and long gamma-ray bursts (lGRBs) which last over 2 s, averaging at about 30 s. Most of the bursts that have been observed[7] and studied in detail today belong to the latter, more data-rich type.

2.3 Prompt and Afterglow Phases

In the prompt phase of a GRB, i.e. in the few seconds of the actual outburst, most of the electromagnetic radiation is released in photons with an energy greater than 1 MeV.

Assuming an isotropic emission, the total energy amount released during that phase is unmatched by any other transients, varying between 10^{49} erg for so-called Low Luminosity GRBs and 10^{54} erg for the most violent bursts, which is equivalent to 5 times the mass of our sun converted to energy through $E = mc^2$.

The light curves (i.e. the count rate of photons over time) of the prompt phase of GRBs typically show several random peaks, but can also contain just a single peak followed by a rapid decay. This behavior is shown for two examplary BATSE lightcurves in Figure 2.3. Although some extensive statistical studies (e.g. [16]) have been undertaken, the temporal behavior of GRBs is still not understood to a satisfying degree.

In contrast to the hard-to-explain light curves, the energy spectra of GRBs are, according to [17], generally described well at low energies by a power-law continuum with an exponential cut-off

$$N_E(E) \propto E^{\delta} \exp\left(-E/E_0\right) \tag{2.1}$$

with $N_E(E)$ being the number of photons at the energy E, δ the spectral index and E_0 the cut-off energy. At high energies a steeper power law without cut-off

$$N_E(E) \propto E^{\eta} \tag{2.2}$$

[7] From all GRBs observed by BATSE only 25% have been short-duration bursts.

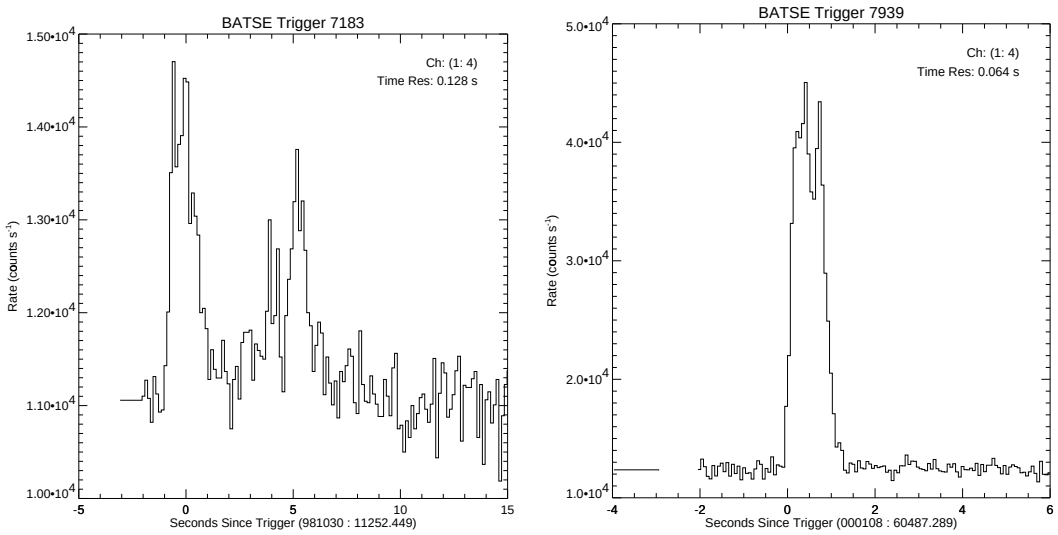

(a) GRB 981030 (b) GRB 000108

Fig. 2.3: *Exemplary GRB lightcurves from the BATSE Burst Alert Telescope. Shown is the count rate in all 4 energy channels (corresponding to energies from 20 keV upwards) over the seconds since the triggering*

with $\delta > \eta$, typically provides good fits. However, the spectral indices δ and η and the cut-off energy E_0 are not universal and vary significantly between different GRBs, excluding progenitor models depending on constant values.

For BATSE bursts, it has been found, that they are generally well described by a modified broken power law

$$N_E(E) = \begin{cases} A\left(\frac{E}{100\,\mathrm{keV}}\right)^{\alpha} \exp\left(-E/E_0\right) & \text{for} \quad (\alpha-\beta)\,E_0 \geq E \\ A\left[\frac{(\alpha-\beta)E_0}{100\,\mathrm{keV}}\right]^{\alpha-\beta} \exp\left(\beta-\alpha\right)\left(\frac{E}{100\,\mathrm{keV}}\right)^{\beta} & \text{for} \quad (\alpha-\beta)\,E_0 \leq E \end{cases}, \tag{2.3}$$

where α is the low-energy spectral index, β the high-energy spectral index and E_0 the cut-off energy[17]. A fit to the above function is exemplary shown for the BATSE detected GRB 911127 in Figure 2.4. The values for α, β and E_0 are also varying between different GRBs.

Over time it has been observed that short GRBs have a generally harder spectrum than the long kind. This can be seen in Figure 2.5 and justifies the assumption of different underlying physical processed between the two classes.

While initially GRBs had only been detected in the gamma regime during their prompt phase, on February 28th, 1997, the BeppoSAX satellite was the first to detect a fading X-ray afterglow clearly associated with the GRB 970228[3].

Within 21 hours after the onset the 4.2 m William Herschel Telescope on La Palma was additionally able to observe the afterglow in the optical range.

Figure 2.6 shows the position of the GRB in the 2 - 10 keV range, captured by the X-ray telescopes of BeppoSAX. The left panel shows the previously unknown bright X-ray source 8 hours after the prompt phase of GRB 970228. On March 3rd, three days later, the source had faded by a factor of about 20, as the right panel shows.

Data about many other GRB afterglows observed since then shows that their duration varies between days and weeks and that they emit radition from X-rays to the radio band. With the end of the prompt emission, often overlapping it, afterglows begin at various

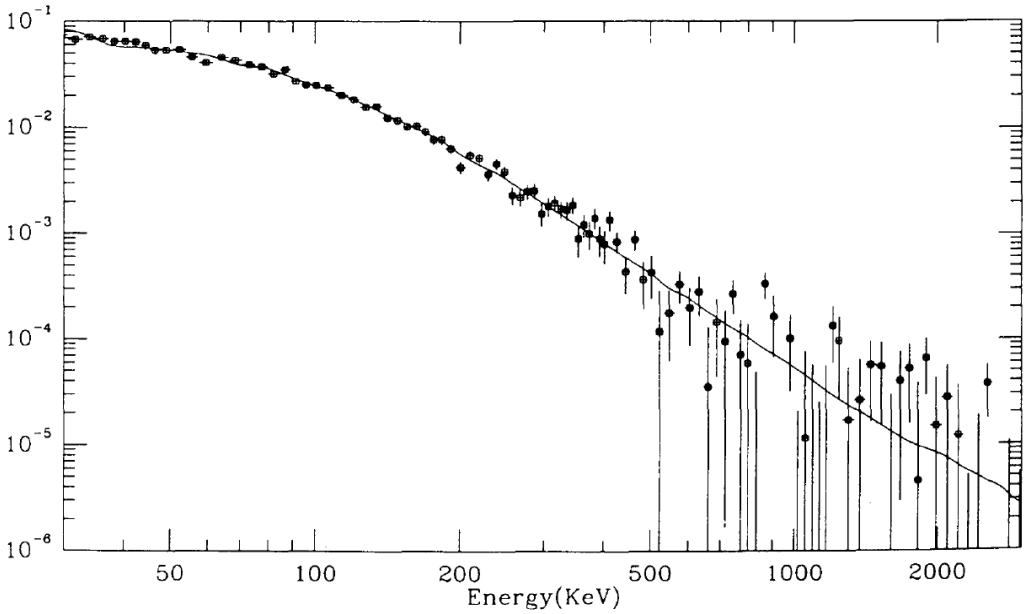

Fig. 2.4: *Fit of the spectrum of GRB 911127 to a conventional and a broken power law as defined in equations 2.1 and 2.2 respectively. The low-energy spectral index is* $\alpha = -0.968 \pm 2.1$*, the high-energy spectral index* $\beta = -2.427 \pm 0.07$ *and the cut-off energy* $E_0 = (149.5 \pm 2.1)\,keV$*.* $\chi^2 = 121.58$ *with 100 degrees of freedom. (Figure adopted from [17])*

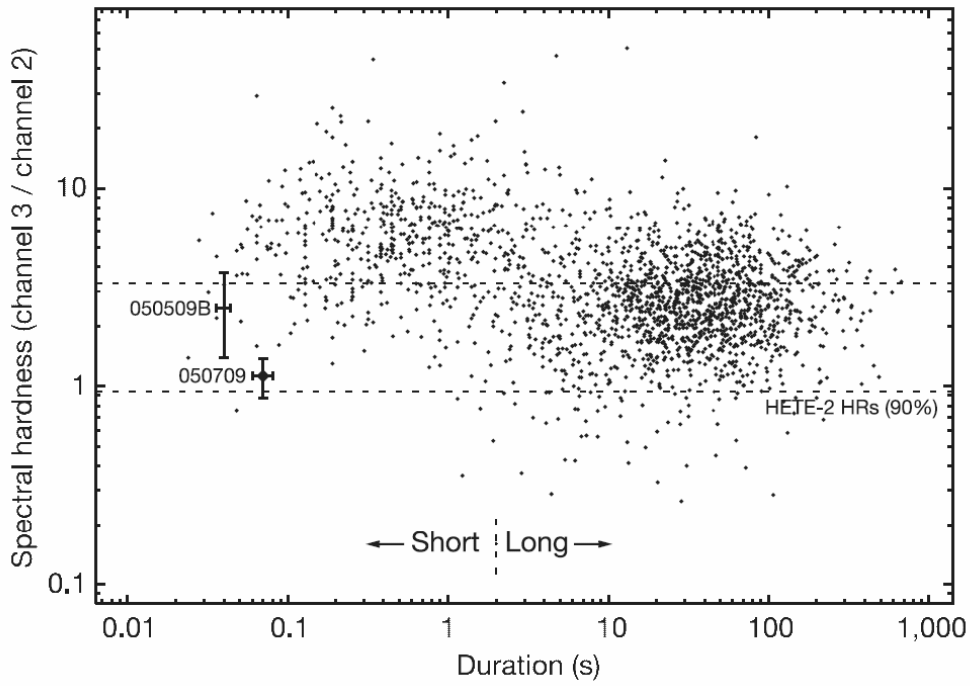

Fig. 2.5: *BATSE and HETE-2 bursts' spectral hardness over* T_{90}*. The spectral hardness is the ratio between the counts in BATSE's channel 3 (100 keV - 300 keV) and channel 2 (50 keV - 100 keV). The HETE-2 hardness ratios have been converted assuming a simple power law model (see [18])*

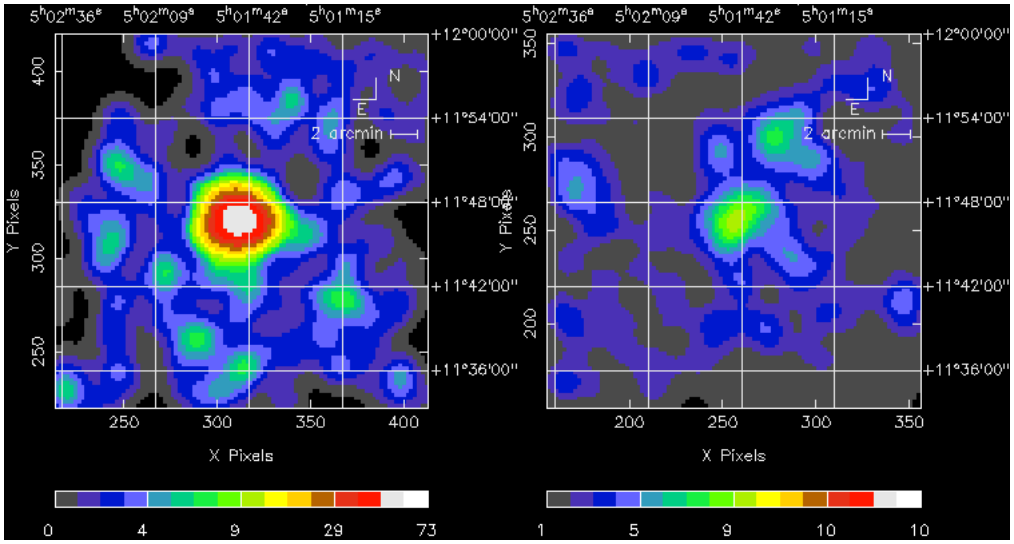

Fig. 2.6: *Two images of the BeppoSAX's X-ray detectors in the 2 - 10 keV range showing the afterglow of GRB 970228 on February 28th, 1997 (left panel) and three days later, on March, 3rd (right panel)*

times, depending on their wavelengths and fade at different rates according to a power law with variable index.

In general, soft X-ray (1 - 10 keV) afterglows start during or with the end of the prompt emission, often remaining detectable for several weeks with sensitive instruments such as Chandra and XMM-Newton.

Optical afterglows are observed for roughly half of all the long duration bursts, commonly in the hours following the burst, although there have been a few cases of simultaneous emission. In many cases the optical afterglow initially outshines the host galaxy in which it originates.

Radio afterglows are similarly detected for about half of the long bursts, but usually several days after the prompt emission, at typical levels of some tenths of a millijansky. Their duration can be longer than a year, as it has been the case with GRB 970508, which has been observed by the Very Large Array in New Mexico for 450 days[19].

2.4 Origin

Early detectors had a very low accuracy while localizing the source of gamma-rays on the sky. A way of circumvention was the triangulation of the detections from several different widely spaced gamma-ray detectors. However, even triangulation yielded too little accuracy to assign host objects like stars or galaxies to the GRBs, rendering distance estimations impossible.

This lack of information gave rise to two distinct classes of theories about the origin of GRBs. One theory, initially widely believed, stated relatively near neutron stars in our own galaxy as the origin of GRBs. This was supported by high luminosities reached by many GRBs, because an extra-galactic source would had implied hard to explain amounts of radiated energy. The other class of theories implied that GRBs occur at cosmological distances which meant that almost all GRBs occurred outside our own galaxy.

After the launch of BATSE on CGRO in 1991 more and more GRBs were recorded and their isotropic distribution on the sky began to show. As the local neutron star hypothesis

predicted that faint bursts would be localized to the plane of the Galaxy, this model was ruled out, as the faint bursts were also distributed isotropically.

After that, there were still intra-galactic theories claiming that GRBs originate in a large local galactic halo, at a large enough radius such that our offset from the center of the Galaxy is not evident.

Only the first observation of a GRB afterglow in 1997 made it possible to determine a more exact location and associate a host galaxy to the GRB, supporting the model that stated an extra-galactic origin. Two months later, absorption lines consistent with gas at z=0.835 were detected in a spectrum of the GRB 970508 optical transient[4], providing strong evidence for the extra-galactic model, which has later been confirmed by many subsequent afterglow observations.

2.5 Formation Scenarios

As gamma-ray bursts exhibit a high degree of diversity regarding both their temporal and their energetic evolution and observational constraints have been scarce when this field of research emerged, there were plenty of theories about possible progenitor scenarios in the beginning.

The short variability timescales t_v of the GRB prompt emission phase of typically under 10^{-3} s requires the volume from which it originates to have a smaller diameter than $d = c \cdot t_v$, with c being the speed of light in vacuum and t the duration of the burst, assuming the producing object moves at non-relativistic speed[8]. This strong indication that the central engine powering GRBs has dimensions in the order of only tens of kilometers, which is typical for neutron stars or stellar black holes, led to the still not invalidated assumption of cataclysmic stellar events as the progenitors of the bulk of GRBs.

This produced a range of progenitor models, including evaporating black holes, magnetic flares on white dwarfs, accretion of matter onto neutron stars, antimatter accretion, supernovae, hypernovae, and rapid extraction of rotational energy from supermassive black holes. With the increasing number of observed GRBs and the growing amount of gathered data, many theories were regarded highly unlikely or could be ruled out altogether.

The early suggested subdivision into long and short bursts with their typical spectral hardness[9] soon led to the suggestion that these two classes were fundamentally different in their progenitors.

Today a well established model for long GRBs involving the core-collapse induced explosion of supermassive stars exists, but there is still no broad consent about the progenitors of short GRBs, which is partly because of the relative scarcity of data about this class, both for the prompt phase and their rarely observed afterglows.

Independent from the particular type of progenitor, a common mechanism of particle acceleration and gamma-ray production is presumed in most models, which is described in the next Section. Thereafter, some well-established theories about the Central Engines providing the for the acceleration necessary energy are presented for both long and short GRBs.

[8] At relative velocities closer to c the volume can be slightly larger, which, however, does not change the overall outcome

[9] see Section 2.3

2.5.1 The Relativistic Fireball Model

The relativistic fireball model (see e.g. [20] or [21]) is an often applied emission model of the massive amounts of energy released in the short timescales, and thus small spatial regions, of gamma-ray bursts.

Energy released at the magnitudes reached during a GRB and deposited in a small enough a volume would lead to photon energy densities high enough to cause massive pair production and subsequent annihilation of e^+ e^--pairs via $\gamma\gamma \longleftrightarrow e^+e^-$ reactions. Because of this the mean free path for γ-ray photons inside such a fireball would be very small, trapping the radiation inside, leading to a blackbody-like thermal spectrum and a super-Eddington luminosity.

As the observed spectra of GRBs are, however, non-thermal, the fireball undertakes, according to this model, an ultra-relativistical expansion, with Lorentz factors Γ between 10^2 and 10^3, which avoids this so-called "compactness problem", which would otherwise lead to an optical depth $\tau >> 1$. Photons that have enough energy to produce pairs are thus reduced by a factor of Γ and the required compactness (according to the fast variability of GRB lightcurves) of the source volume is reduced by a factor of Γ^2. Furthermore, the presence of even a small fraction of baryons, which is limited by Γ to less than $10^{-5} M_\odot$, makes the plasma opaque to Thomson scattering, which contributes to the acceleration of the fireball until a considerable fraction of the initial energy has been converted into bulk kinetic energy of the baryonic contamination.

There are two suggested models for the subsequent conversion of the fireball's kinetic energy to gamma radiation, one involves internal shocks[22], the other external shocks[23]. The latter scenario states that the relativistic matter runs into an external medium, either interstellar gas or stellar wind earlier emitted by the progenitor, leading to the formation of shock waves, while in the former the inner engine is assumed to emit many shells with different Lorentz factors, which eventually collide into one another producing internal shocks.

A widely accepted scenario for the overall process is displayed in Figure 2.7, showing the temporal evolution of a relativistic fireball: The GRB itself is believed to be produced by the internal shock processes, while the afterglow starts when the expanding shells interact with external matter. This leads to the external shocks, which accelerate the leptons to energies describable by a power-law distribution. This results in the emission of the synchrotron radiation observed in afterglows in the residing magnetic fields.

The high Lorentz factors that are proposed by this mechanism result in unequaled ejection speeds for particles with non-zero rest mass of $0.99995\,c$ and above, not even reached by the matter jets of quasars or microquasars.

2.5.2 Progenitor Models

The fireball model described above presumes an energy supply from a central engine, which is provided by the progenitor of the GRB. It is believed that the particular progenitor scenarios are different for the two classes of GRBs.

While there is a great number of observed long GRBs, which supplied enough constraints to exclude many priorly suggested progenitor models, for short GRBs, there is still only a handful of events with associated host galaxies, both because of the short duration of the bursts themselves and because of the few corresponding afterglow observations.

However, those that could be associated show a significantly different localization than long bursts. While long bursts are mostly found in the actively star forming regions of young galaxies, e.g. in the arms of spiral galaxies[25], most short bursts are situated

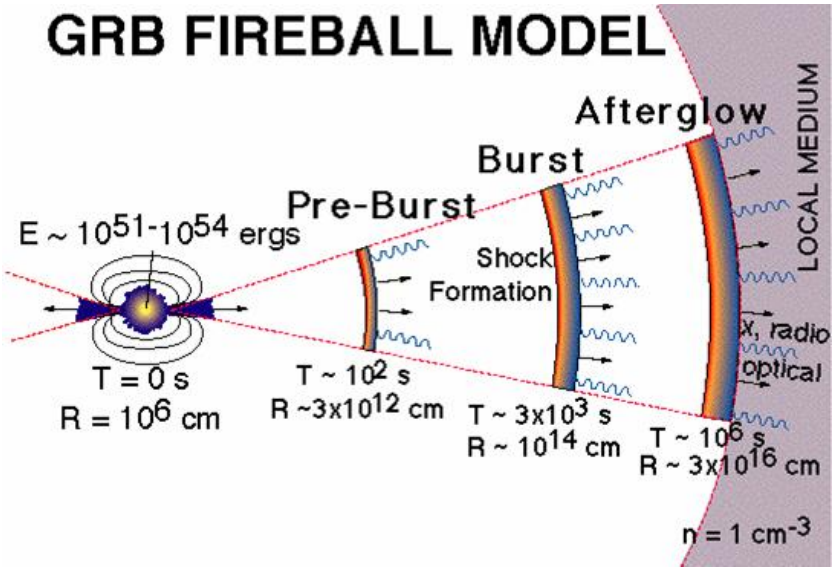

Fig. 2.7: *Schematic display of the temporal evolution of a relativistic fireball during a GRB. The different phases of the burst are shown together with their approximate distance R from the central engine and the time T of their occurrence since onset of the burst. (Figure adopted from [24])*

in galaxy regions, where star forming has long ceased, e.g. in old stellar populations of elliptical galaxies, as it was the case with GRB 050724[26]. The complete lack of supernovae associated with short bursts also contributes to the uncertainty in their progenitor scenarios.

In the following the most promising theories about the progenitors of both kinds of GRBs are introduced.

The Collapser Model for Long GRBs

The most established and widely accepted model about the progenitors of long-duration GRBs is the so-called collapser model, described in [27][28]. It states that a burst of this kind is produced during the supernova-like death of a super-massive star with low metallicity and a high enough rotational speed. At the end of such a star's fusion cycle, when the majority of the lighter elements have been fused to iron and it is no longer possible to compensate the compressing gravitation with the produced thermal pressure, its core collapses, which, in this case, leads to the formation of a black hole.

In the aftermath, stellar matter around the core falls down towards the collapsed core and, when the star is spinning at sufficient speed, swirls into a high-density accretion disk, i.e. a rotating disk of matter around the black hole. The in-falling material yields a strong heating that, in its turn, produces a copious amount of thermal neutrinos and antineutrinos, which annihilate preferentially around the rotation axis producing the fireball of e^+ e^--pairs and γ-ray photons described in Section 2.5.1

For rapidly rotating stars, the fireball is collimated towards the poles of the system by magnetic fields and subsequently ejected as a pair of highly relativistic jets along the rotational axis, where the matter density is much lower than in the accretion disk, creating leading shock waves.

For the jets' material to reach the stellar surface, the star must have stripped off its hydrogen envelope before the core collapses. This is increasingly likely with lower metallicity

of the star. If this has happened, the leading shock accelerates as the density of the star's matter it travels through decreases. Upon arrival at the surface, its velocity can account for the required Lorentz factor of $\Gamma > 100$.

When the jets break out into open space, much of their kinetic energy has been converted to gamma-rays.

Because of the high required mass, low metallicity and rapid rotation of the progenitor stars, gamma-ray bursts are far rarer than ordinary core-collapse supernovae, which only require a stellar mass high enough to overcome the internal pressure generated by a degenerate neutron gas due the quantum mechanical exchange interaction.

Double Degenerate Merger Scenarios for Short GRBs

These models involve a binary system of two degenerate objects. Many possible scenarios have been suggested, e.g. the merger of two white dwarfs, a white dwarf and a black hole, two neutron stars or a neutron star (NH) and a black hole (BH), but the latter are deemed to be the most likely to account for the rate of observed sGRBs.

In a close binary system of two compact objects, the orbiting companions permanently lose energy due to gravitational wave radiation (GWR), according to Einstein's general theory of relativity. This will reduce the mean distance of the objects, narrowing their orbits.

Eventually the neutron star (in NS-NS systems the one with the lower mass and therefore larger radius) will fill its Roche lobe[10] and matter will flow to the companion at a relatively slow rate, until the tidal forces exerted on each other are sufficient to rip one (in case of a NS-BH binary) or both (in case of a NS-NS binary) of the objects apart, drastically accelerating the mass transfer.

Below a certain critical mass, the matter-losing neutron star will be unstable and expand explosively, overflowing its Roche lobe and delivering all of its mass into a large accretion disk around the black hole or companion neutron star.

In the following, the massive disk will either fall into the BH or lead to the collapse of the remaining NS into a BH, provided the masses of both NSs exceed the critical upper limit for a NS of approximately $2.3\,M_{\odot}$. The amounts of energy being liberated in the process would then be sufficient to power a GRB. For a BH-NS merger, snapshots of a simulation taking into account general relativity can be seen in Figure 2.8, which demonstrates the final formation of a thick disk of matter around a BH, later powering the sGRB.

The final stage of the merging is thought to happen in only a few seconds, which would account for the very short durations of sGRBs. Furthermore, the lack of conventional stars in a double degenerate scenario would explain the missing supernovae, at least for the types Ib,Ic and II, as these require the collapse of a massive star's core.

A problem with this model is the observation of X-ray flares for several sGRBs[11], appearing minutes to days after the burst itself, when the merger should long have been completed. This is a strong indication that not all sGRBs originate from the merger scenario described above. A progenitor model taking into account the late X-ray flaring is described in the next Section.

[10] The Roche lobe is the volume around a binary system star in which orbiting material is gravitationally bound to it. An expansion of the star past its Roche lobe causes the material outside of the lobe to fall into the companion star.

[11] e.g. GRB 050709 and GRB 050724

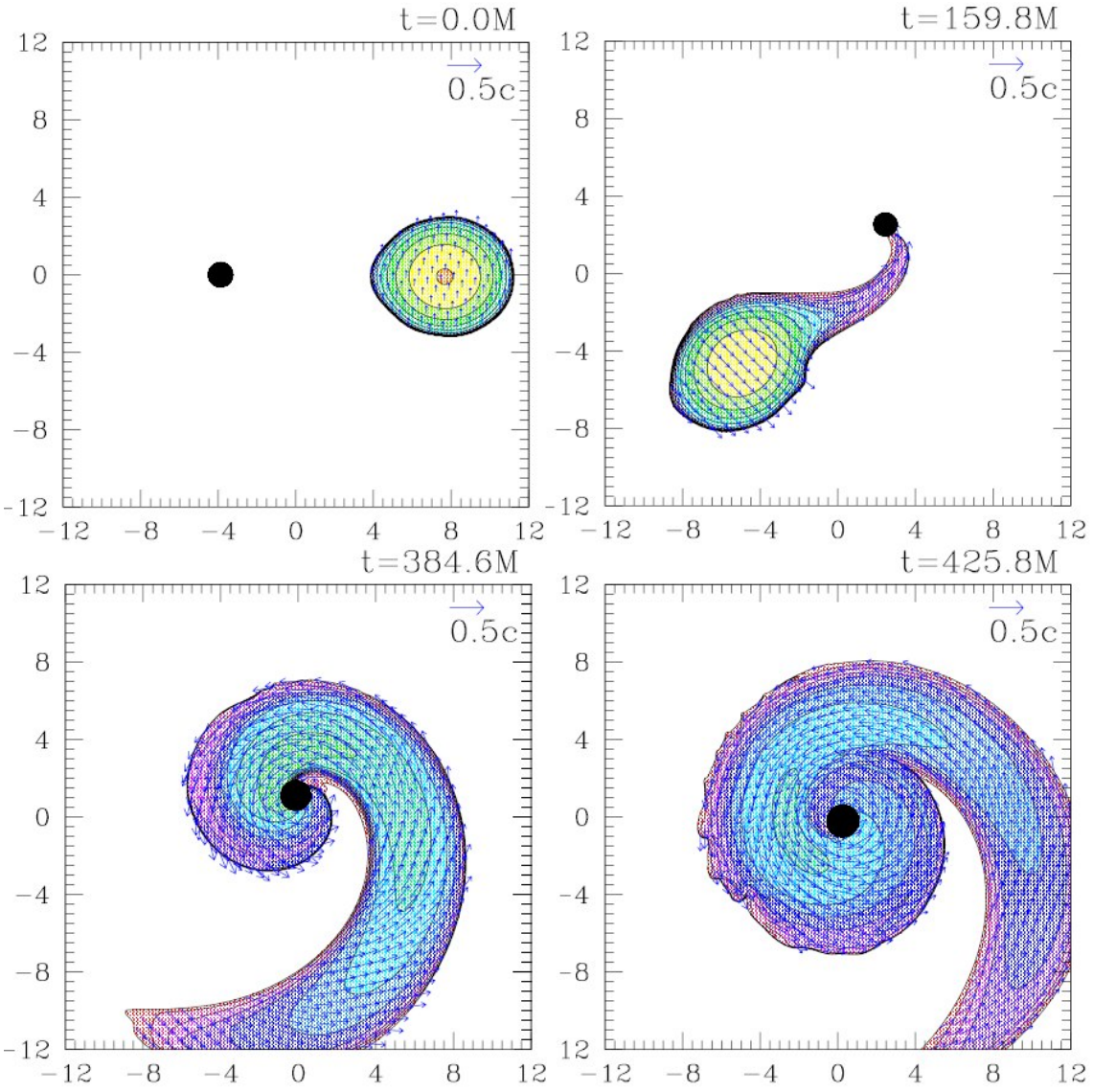

Fig. 2.8: *Snapshots at selected times of a general relativistic simulation of a BH-NS merger, with a BH/NS mass ratio of 2. The contours represent the density in the orbital plane, plotted logarithmically with four contours per decade. Arrows represent the velocity field in the orbital plane. (Figure adopted from [29])*

Magnetar Giant Flares Scenario for Short GRBs

Magnetars are rapidly spinning neutron stars with extremely powerful magnetic fields in the order of terrateslas, making them the most strongly magnetized objects in the universe. Several models involving different scenarios predict them to be another possible progenitor of at least part of the sGRBs[30][31][32].

A class of recurrent transients emitting soft gamma-rays, the soft gamma-ray repeaters (SGRs), are commonly linked with magnetars, for which their magnetic field is the dominant source of free energy, greater even than their rotational energy. According to most theories, a SGR burst is powered by this vast supply of magnetic field energy and happens when magnetic stresses build up sufficiently to crack a patch of the neutron star crust and a fireball of hot plasma particles is ejected into the magnetosphere.

Exceptionally violent SGR outbursts, called giant flares, have been emitted by three of the known SGRs by now. Giant flares begin with a short spike of gamma-rays, in the order of 0.2 s, with energies up to 100 MeV, containing most of the flare energy, followed by tails of hard gradually fading X-ray emission oscillating at the rotation period of the magnetar.

The first two observed giant flares came from SGR 0525-66 in the Large Magellanic Cloud on March 5th, 1979 and from SGR 1900+14 in our galaxy, on August 27th, 1998, but their luminosities were not high enough to account for cosmological sGRBs. On December 24th, 2004, however, an enormous burst was detected from the intra-galatical SGR 1806-20, which was luminous enough to be detected at cosmological distances.

This supported progenitor models positing that some sGRBs may be magnetar giant flares, which can be explained by a catastrophic instability involving a global crust failure and magnetic reconnection, with possible large-scale untwisting of magnetic field lines outside the star[31].

Some models also predict these flares to be emitted during the formation and evolution of new-born "proto-magnetars" which have been formed during an accretion-induced collapse of a white dwarf, or the merger of neutron stars and/or white dwarfs in binary systems[32]. Here the initial emission spike of the flare is powered by accretion onto the proto-magnetar from a small disk that is formed during the accretion-induced collapse or merger event, while the extended X-ray emission is produced by a relativistic wind that extracts the rotational energy of the proto-magnetar on a timescale of order 10^2 s. Because a supernova needs the ejection of ^{56}Ni, whose decay powers it, and proto-magnetars eject only a very small amount of this isotope, the missing association of sGRBs with supernovae can also be explained.

3 The H.E.S.S. Telescope Array

The H.E.S.S. project, for which an automatic GRB response system has been developed, is a leading experiment in the field of ground-based gamma-ray astronomy. It consists of four Imaging Atmospheric Čerenkov Telescopes, seen in close-up in 3.1 and as a whole in Figure 1.6, situated at 23°16'18" S, 16°30'00" E in the Khomas District of Namibia, 100 km south-west of the capital Windhoek on a site near the farm Göllschau 1800 m asl.

H.E.S.S. has been designed for stereoscopic imaging, which means that air showers generated in the atmosphere by in-falling particles with very high energies are observed from multiple positions on the ground. To account for that, the arrangement of the telescopes resembles a square with 120 m side length, representing a compromise between the large base length required for good stereoscopic viewing of the showers, and the requirement that two or more telescopes are hit by the light of an observed shower. H.E.S.S. can detect gamma-rays in the energy range of 100 GeV until about 100 TeV, with an energy resolution of 15 - 20% and a typical angular accuracy of less than 6 arc minutes for a single photon. Its sensitivity is high enough to detect a source with a flux one hundred times weaker than the Crab Nebular in 25 hours.

Observation is done in partitions called *runs*, usually lasting 28 minutes each. Only one target position is observed during a specific run, and all have to pass data quality

Fig. 3.1: *Two of the four 13 m H.E.S.S. telescopes, each surrounded by four lightning conductors*

criteria before they are used for analyses. This ensures that runs with hardware problems, bad weather conditions and other sub-optimal observation conditions do not degrade the quality of the analyses' results.

The following Chapter describes the observation technique employed by H.E.S.S., the stereoscopic imaging of Čerenkov light emitted by atmospheric showers, whose properties will be explained in the course. Furthermore, it contains a description of the various hardware components belonging to H.E.S.S., as well as an introduction to the standard data analysis procedure.

3.1 Air Showers

Cosmic gamma-rays as well as hadronic particles with a sufficient amount of energy will produce an avalanche of secondary particles when crashing into the atmosphere, called an *air shower*. The evolution and inner structure of these showers greatly depend on the primary particle triggering them.

3.1.1 Electromagnetic Showers

This type of air shower is produced by a high energy γ-ray photon hitting the Earth's atmosphere, starting a cascade when it decays to an electron-positron-pair in the electromagnetic field of, for example, a nitrogen nucleus after a typical mean free path called the conversion length. The produced leptons will then emit new γ-ray photons via Bremsstrahlung, each of which has the chance to do pair production once again. The mean free path of this process is the radiation length, i.e. the length after which the leptons have lost all but $1/e$ of their initial energy E_0.

The pair production and emission of Bremsstrahlung will be repeated over and over again, leaving each new generation of e^+e^--pairs with less energy. Applying a very simple model, depicted in Figure 3.2 and described in [33], already yields some basic properties of this type of air showers. The model assumes that the only particle producing processes are Bremsstrahlung and pair production, that radiation length and conversion length are equal, and that each new generation of particles get equal shares of energy from their progenitors. The conversion and radiation length, both denoted X_0, are thereby given in units of length per area, which accounts for the integrated atmospheric density traversed.

The number of particles N at an atmospheric depth X, i.e. the total atmospheric distance covered, is then given as

$$N(X) = 2^{X/X_0}. \tag{3.1}$$

The maximum shower width is reached when the particle energy falls below a critical energy $E_c \approx 80\,\mathrm{MeV}$ at a distance

$$X_{\max} = \frac{\ln E_0/E_c}{\ln 2} \cdot X_0, \tag{3.2}$$

after which the ionization of air molecules becomes the dominant mode of energy loss and the shower starts to subside. At this point, the number of particles is

$$N_{\max} = 2^{X_{\max}/X_0} = \frac{E_0}{E_c}. \tag{3.3}$$

When the minimal amount of energy needed for the production of a e^+e^--pair, $E_{\min} = 1.022\,\mathrm{MeV}$ can no longer be met by the secondary photons, the shower propagation finally ceases.

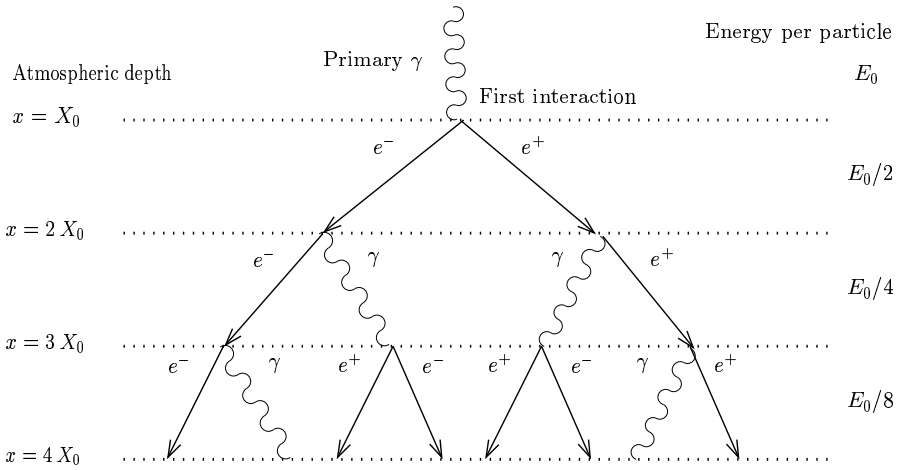

Fig. 3.2: *Simplified model of an electromagnetic shower formation triggered by a high energy gamma photon (Figure adopted from [34])*

It can thus be seen that this simple model predicts an exponential increase of particles in an electromagnetic shower until it reaches the depth $X_{\max}$. Furthermore, the proportionality between the initial energy of the primary particle E_0 and $N_{\max}$ and the logarithmic growth of the shower maximum $X_{\max}$ with E_0 is shown. Inspite of the simple assumptions made, these results are found qualitatively true even when applying more complex models which among other things account for energy loss during shower formation and higher order electromagnetic interactions.

The lateral evolution of this showers is dominated by Coulomb scattering processes, i.e. when the leptons interact with nuclei of the atmosphere. Each such event will scatter the incoming particle by a small angle, increasing the width of the shower as the particles move away from the main axis. Another process of lateral expansion is the fact, that Bremsstrahlung photons emitted by electrons are radiated in a cone in forward direction with an average opening angle of $\langle\vartheta\rangle = 1/\gamma$[1]. However, due to the highly relativistic speed of the electrons, this broadening effect is very small and can be neglected.

The lateral distribution of an electomagnetic shower can be described with the Molière radius R_{mol}, in which, on average, 90% of the energy of a shower is deposited. It can be calculated as

$$R_{\text{mol}} = 0.0212\,\text{GeV}\frac{X_0}{E_{\text{c}}} = \frac{9.6\,\text{g}\,\text{cm}^2}{\rho_{\text{air}}}, \tag{3.4}$$

where ρ_{air} is the density of the atmosphere and $X_0 = 37.2\,\text{g}\,\text{cm}^2$. Consequently, the maximum shower radius depends on the altitude where it was formed, which is, for VHE gamma-rays, typically between 8 and 10 km above sea level.

3.1.2 Hadronic Showers

As protons are by far the biggest part of the cosmic-rays, hadronic showers are significantly more frequent than their electromagnetic counterparts. In the energy range observable with H.E.S.S., there is only about one gamma-induced shower per 100 hadronic showers, making it a crucial requirement to be able to distinguish between these types.

In a hadron-induced air shower, the creation of secondary particles mostly occurs via inelastic scattering on the atmosphere's nuclei. At high energies, this leads to the creation

[1] γ is here the Lorentz factor $\left(1 - v^2/c^2\right)^{-1}$, where v is the electron's velocity.

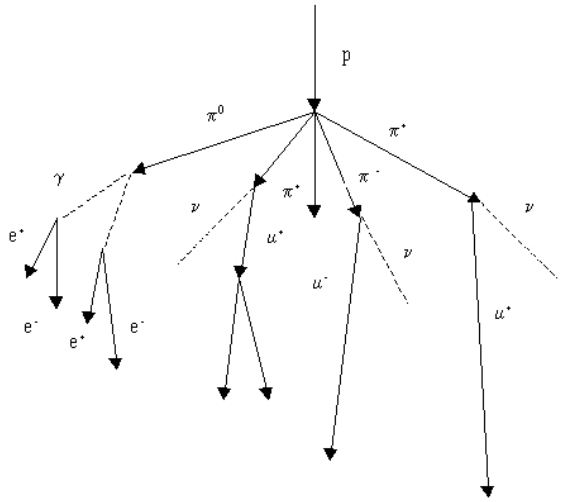

Fig. 3.3: *Schematic view of a hadronic shower formation initiated by a cosmic-ray hadronic particle*

of several secondary particles and to particle emission originating from the nuclear decay of the excited nuclei. In these interactions, the main products are neutral and charged mesons, mostly pions and kaons, as well as nucleons and hyperons. The mesons subsequently decay into high energy photons, electrons, muons and neutrinos. Therefore, this kind of shower has a hadronic as well as an electromagnetic component. While the core of the shower is hadronic, the decaying mesons constantly feed the electromagnetic part, thereby creating sub-showers of this kind, as indicated in Figure 3.3.

The long-lived muons and the neutrinos do not contribute to the shower cascade and are thus dissipating a part of its energy. An additional part gets lost in nucleus interactions. Thus a proton with the same initial energy than a gamma photon produces a shower whose electromagnetic component contains only one third of the particles of the gamma-induced shower.

In contrast to the electromagnetic showers, the lateral evolution of hadronic showers is dominated by weak and strong interactions of the secondary particles, giving rise to larger transverse momenta. This accounts for a significantly larger spread compared to gamma-induced showers, which evolve mostly near the shower axis due to the, on average, small Coulomb scattering angles.

Another difference are the larger fluctuations of hadronic showers, caused by the occurring complex multi-particle processes as opposed to the dominating three particle processes of electromagnetic showers. This irregularities lead to a larger variance in the possible forms of this showers, making their identification more difficult. A comparison of the two types, generated with Monte Carlo[35] simulations is shown in Figure 3.4.

3.1.3 Emission of Čerenkov Light

Most of the relativistic electrons[2] in the shower move at a velocity v higher than the local speed of light c_l, which is slightly lower than the vacuum lightspeed c. This movement of charged particles through an insulating medium leads to the emission of Čerenkov light in a similar fashion as an object that moves at supersonic speed emits a cone of sound waves. This happens because under such circumstances its electromagnetic (EM) field polarizes

[2] in the following also referencing positrons

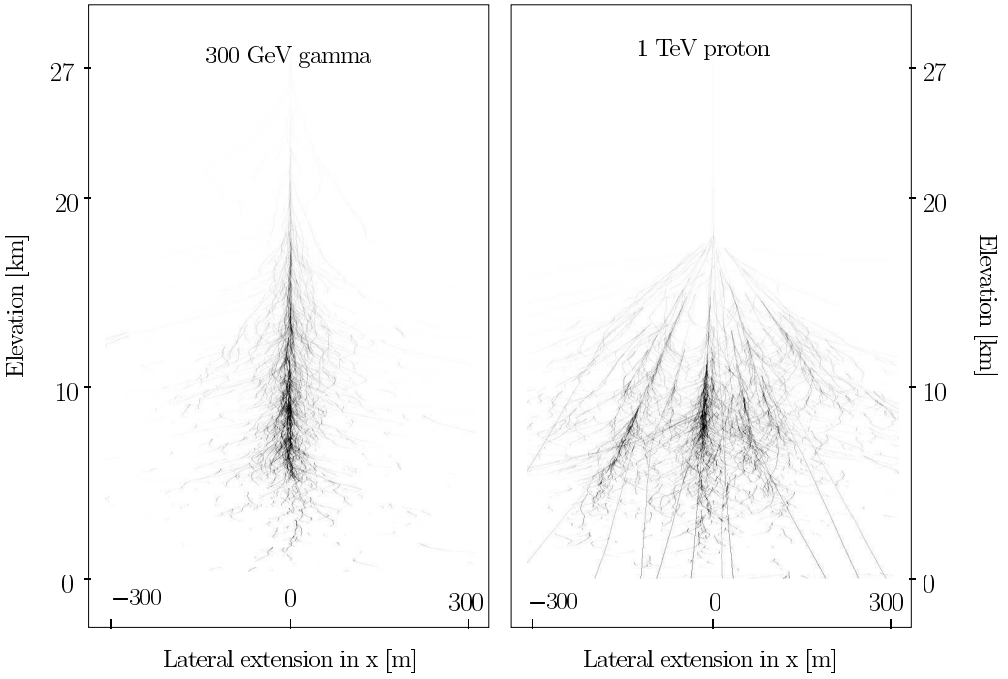

Fig. 3.4: *Comparison between the longitudinal evolution of an electromagnetic and a hadronic shower. Shown are the tracks of individual secondary particles generated via Monte Carlo simulations and projected into the picture plane. (Figure adopted from [34])*

the insulator atoms it passes by shortly displacing their electrons and thereby producing dipoles. While restoring the equilibrium, these atoms emit EM waves themselves, which is not the case in a conductive medium. At velocities exceeding the local phase speed of light, these waves interfere constructively, entailing an overall dipole field and thus EM emission. Figure 3.5 shows a schematic view of the geometry of Čerenkov radiation.

The opening half-angle θ of a Čerenkov light cone can be calculated as

$$\theta = \arccos \frac{c_{\mathrm{l}}}{v} = \arccos \frac{1}{n\beta} \tag{3.5}$$

where n is the refractive index of the medium and $\beta = v/c$. As this equation shows, a threshold velocity exists at $v = c/n$ below which no radiaton it emited.

The spectrum of Čerenkov light is continuous and the more intense the shorter the wavelength. Because for a given medium the refractive index n generally decreases with increasing frequency, there is a cut-off at some point when n falls below $1/\beta$. This normally happens in the UV range, where the spectrum has its peak.

The majority of gamma-ray induced air showers reach their maximal extension at an altitude of 8 to 12 km, so most of the ultra-violet light is absorbed by ozone before it reaches the ground. IACTs therefore see Čerenkov light mainly at the blue end of the visible range and are optimized for these wavelengths. Atmospheric extinction processes like Rayleigh and Mie scattering further reduce the flux of the photons that reach the ground. At an observation altitude of 2000 m asl., a primary 1 TeV gamma-ray produces only 100 Čerenkov photons per square meter.

As the paths taken by the secondary particles of an air shower are not parallel to its axis, the region on the ground that is illuminated by Čerenkov light cones from a certain

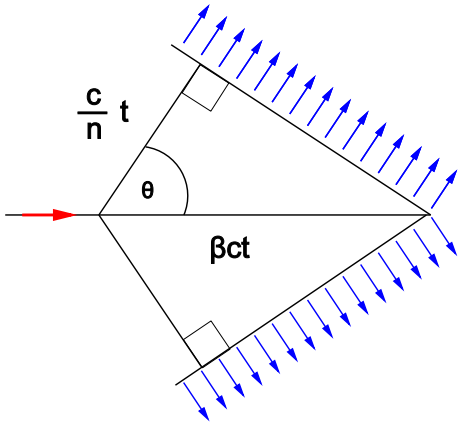

Fig. 3.5: *Schematic view of the geometry of Čerenkov radiation*

shower is not a circular ring, as it is for example for single muons emitting Čerenkov light, but an almost homogeneously filled circular area with a blurred boundary. Depending on the shower parameters, the radii of the circles vary, in case of electromagnetic showers, between 80 m and 150 m and the time between the arrival of the first and the last photon is only a few nanoseconds.

3.2 Imaging of Čerenkov Showers

Like other IACT experiments[3], H.E.S.S. uses large tessellated spherical reflectors to focus the Čerenkov light from air showers onto the focal plane of a highly sensitive camera. As air showers can be observed when some of the telescopes are situated anywhere in the shower's circular light pool, its area of roughly 50000 km^2 is regarded as the effective detection area of IACTs and is thus much larger than for satellite experiments.

The optical aperture of the H.E.S.S. telescopes focuses light rays viewed under the same opening angle towards the optical axis of the reflectors onto the same point in the camera's coordinate system. If the position of the camera center is at $(x, y, z) = (0, 0, 0)$, then a light ray from an atmospheric shower at (x,y,z) is mapped to the angular camera coordinates

$$\begin{pmatrix} u \\ v \end{pmatrix} = -\frac{f}{z} \begin{pmatrix} x \\ y \end{pmatrix} \tag{3.6}$$

where f is the focal length of the reflector.

The basic principle of how an air shower is imaged is shown in Figure 3.6, which shows a telescope imaging a shower and the corresponding camera image. It can be seen, that points along the shower axis, which is also the major axis of the imaged ellipse, are mapped to a straight line into the camera plane.

A point at infinite altitude on the shower axis would be mapped to the coordinates $(u, v) = (-\theta_x, -\theta_y)$, which resemble the angular offset of the telescope's optical axis from the position of the source, i.e. the direction where the shower came from. For gamma-rays, this is identical with the origin of the particles, as has been mentioned before.

The approximately elliptical shapes of gamma-ray induced showers get imaged on the camera plane as ellipses, that are the more elongated the farther they are away from the center of the camera, which is based on the non-linear nature of Equation 3.6. Energy,

[3] see Section 1.2.2

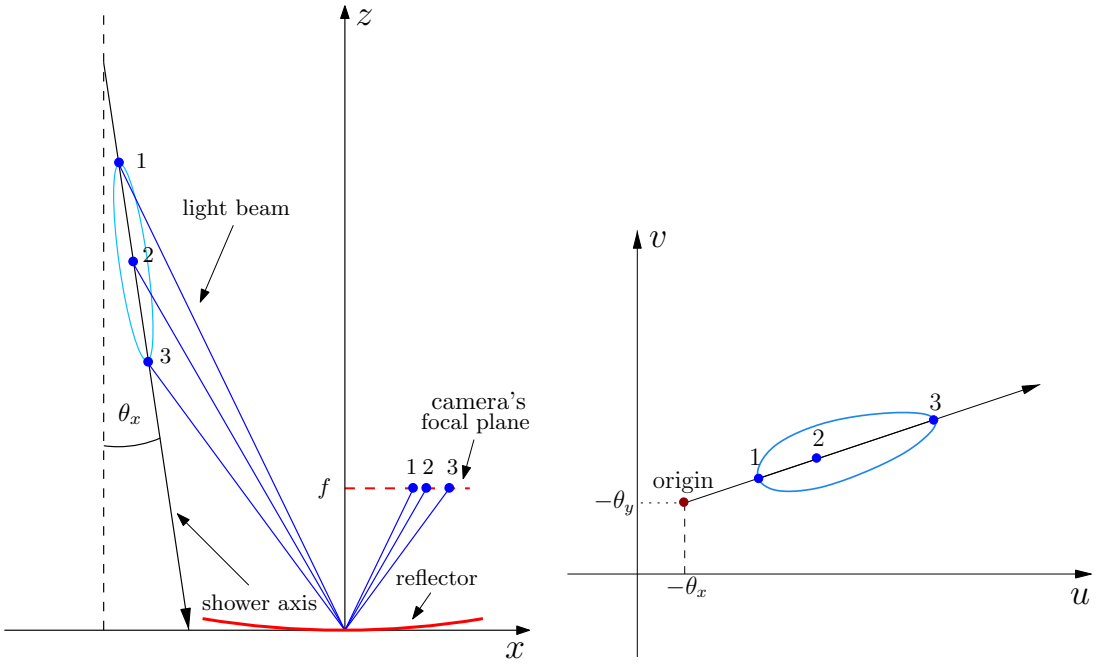

(a) Shower image mapping

(b) Corresponding camera image

Fig. 3.6: *The imaging of an incident Čerenkov air shower on a H.E.S.S. camera*

direction and type of the primary particles can later be extracted from the shape and intensity of the ellipses.

H.E.S.S. uses stereoscopic imaging to improve the quality of the information extracted from the showers, which means their observation is done with at least two telescopes. This leads to a number of advantages over single telescope systems:

- The viewing of the showers under different angles allows a stereoscopic reconstruction of their geometry, i.e. it is for example possible to triangulate the source of the shower[4]. Since single shower images are in many cases inaccurate and ambiguous, for example regarding the impact point on the ground, this poses a great improvement.
- Many non-gamma events that are only visible in one telescope at a time can be rejected. This is for example the case with the narrow Čerenkov light cones generated by local muons, which for single telescope setups constitute a large part of the background.
- The separation between electromagnetic and hadronic events is much more effective when different viewing angles can be considered. A hadronic shower image that looks like it is gamma-induced from one side can often be identified as background under a different perspective.

In summary, stereoscopic imaging leads to improved sensitivity, a lower minimum energy threshold and a better reconstruction of the directions of the primary particles. For more details on the approach, see [34].

[4] see Section 3.4.5

3.3 The Telescope Array

In the following, the essential parts needed to run the H.E.S.S. experiment are introduced. This comprises the telescopes, the tracking system, the cameras as well as the central trigger hardware. A detailed description of the data acquisition software follows in Chapter 4.

3.3.1 Reflector Dishes

For cost efficiency, the reflector dishes of the H.E.S.S. telescopes each feature a setup consisting of 380 small round mirrors, as shown in Figure 3.7, aligned on a hexagonal dish with a flat-to-flat diameter of 12 m. The mirrors are arranged on a sphere with radius $f = 15\,\mathrm{m}$, the focal length of the dish, in a Davies-Cotton design[36], which provides good imaging of off-axis rays. Each has a radius of 30 cm and reaches a reflectivity of 80% - 90%. Their mount to the telescope frame is done at three suspension points. For two of these points the distance to the frame can be adjusted via servo motors, which makes it possible to individually change the orientation of every mirror. With this arrangement, the total area covered with each telescope dish sums up to $108\,\mathrm{m}^2$.

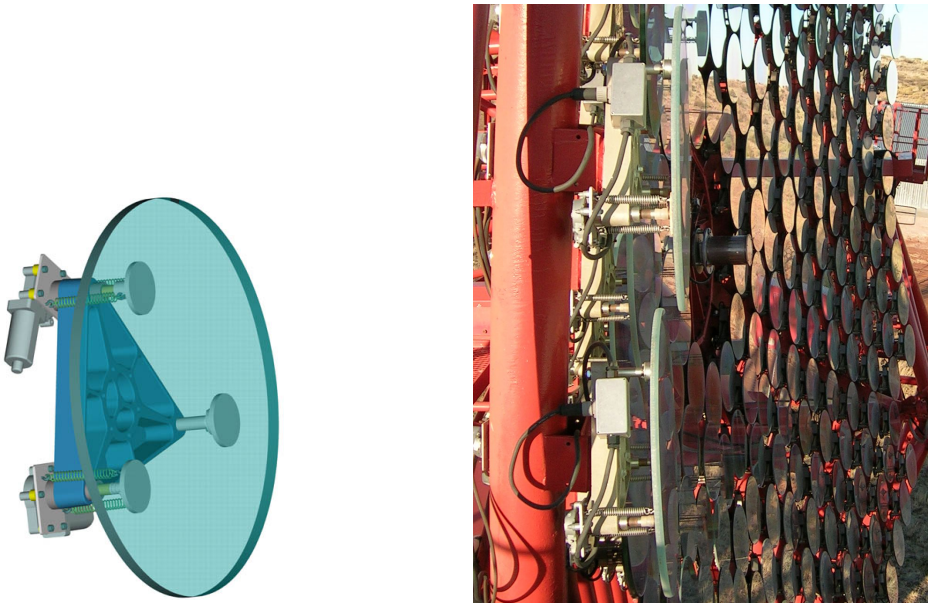

(a) A CAD schematic (b) Photograph

Fig. 3.7: *H.E.S.S. mirror facets with the adjustable mounting visible*

3.3.2 Tracking System

The telescope's tracking system basically consists of an altitude-azimuth mount. For azimuthal slewing, each mount can rotate on a circular rail with a diameter of 13.6 m, impelled by servo motors. The elevation is controlled via friction drive systems acting on altitude rails at about 7 m radius from the axes. A maximum speed of 100° per minute can be sustained in both directions. Elevation is covered in the whole range and can also drive the telescopes directly over the 90° position, thereby orienting the dishes "head first". This is, however, usually avoided in order to keep the coordinate system of the cameras upright, which simplifies the analysis.

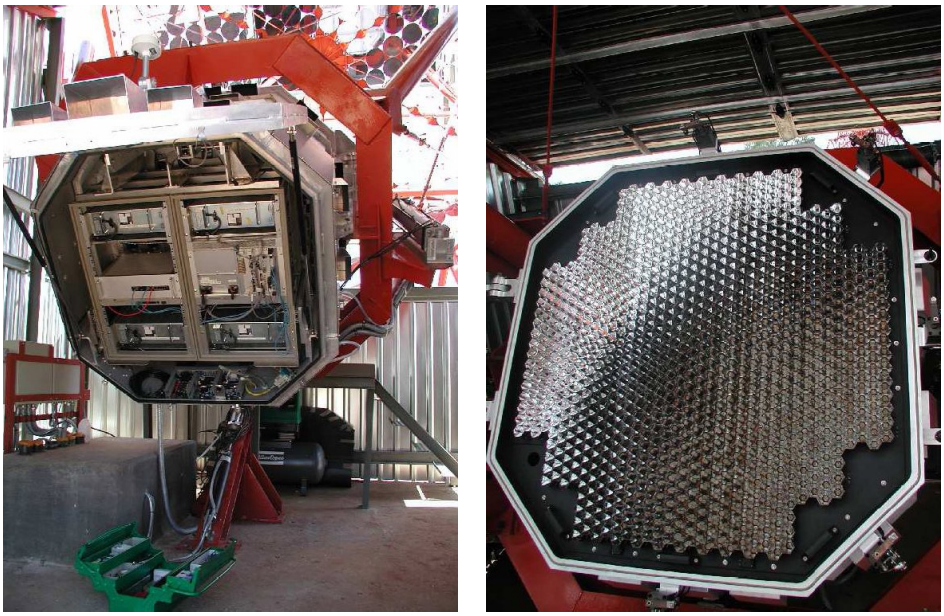

Fig. 3.8: *A view of the second H.E.S.S. camera. The left picture shows the opened housing with the four power supplies and internal electronics, while the right picture displays the dish faced side of the camera with open lid, exposing the 960 Winston cones covering the PMTs.*

The momentary orientation of the telescopes is constantly monitored via shaft encoders, theoretically reaching an accuracy of under 3 arc seconds. However, the real precision is strongly depended on wind or gravity induced deformation of especially the camera steel mounting, but also of the whole structure. To measure this misalignment, each telescope is equipped with two digital CCD cameras, of which one directly photographs the night sky in a direction parallel to the telescope's optical axis and one the reflection of the stars on the closed camera lid. By comparison of the two pictures and the contained bright stars, whose positions are known at high accuracy, the alignment error can be corrected. This is regularly done in dedicated pointing runs of the H.E.S.S. array, thus reaching a total pointing accuracy of better than 30 arc seconds.

3.3.3 Cameras

The four identically constructed telescope cameras, which are designed to record Čerenkov light flashes of only a few nanoseconds duration, provide a large field of view of 5° each. This allows optimal observation also of extended gamma-ray sources. As Figure 3.8 shows, each camera is housed in a 1.6 m diameter body, containing the whole fast data-readout and processing electronics. Furthermore it contains 960 photomultiplier tubes (PMTs) operated at high voltage (HV) with an average quantum efficiency of about 15%, each constituting a pixel of the camera covering 9.6 arc minutes of the sky. Photon losses are minimized by hexagonal Winston cone light collectors, which focus the incoming photons on the circular active PMT areas.

When the camera is in operation, the analog signal amplitude of each PMT is amplified by two different gains, a high gain (HG) and a low gain (LG), which are digitalized via analog-to-digital converters (ADCs) and permanently written into fast, 128 ns deep analog ring samplers (ARSs) at a sample rate of 1 GHz. The two different amplification gains

are used to allow a high bandwidth of possible ADC counts. The HG channel is good for signals corresponding to up to 200 p.e. while the LG channel covers a range from 16 to 1600 p.e.. The conversion of the ADC counts to p.e. numbers is discussed in Section 3.4.1.

A modular design has been applied for the cameras, subdividing them into 60 drawers of square blocks containing 16 PMTs each. Additionally, the camera's internal trigger electronics partition the PMTs into 38 overlapping sectors, each containing 64 pixels. Only if, in a time window of 1.5 ns, one of them contains more than 4 pixels (sector threshold) exceeding a value of 5 photo electrons (pixel threshold) each, a possible event is assumed[5]. If this happens, the camera sends a trigger signal via fiber optical cable to the central trigger system, which will have the final decision on whether to read out the event or not. Additionally, the readout of the pixel intensities corresponding to the event is triggered. This means that for each PMT the ADC counts stored in the respective ARS is integrated over a time-window of 16 ns, beginning from a certain time in the past, which is chosen to accommodate the delay between the event and the central triggers readout signal.

3.3.4 Central Trigger

The central trigger system, described in more detail in [37], as second stage of the H.E.S.S. hardware trigger receives trigger signals from all telescopes and serves as a final decision maker of whether an event will be accepted. The main purpose of the central trigger is to enforce the requirement of multiple telescopes triggering on the same event.

For a final acceptance of an event, at least two telescopes must have coincidently triggered within a time window of 50 ns. When this happens, the central trigger tells the cameras to transfer the 16 ns of PMT signal data acquired for every pixel to the processing programs called called the *CameraReaders*[6] running on the experiment's computer cluster .

3.4 Analysis

For a better understanding of how the telescope-gathered raw data is processed to gain gamma-ray views of the sky, the following Section will give an introduction to the procedures applied during a standard H.E.S.S. data analysis in the order of their practical application. As the unprocessed data from the cameras' pixels, i.e. from the PMTs, comes in the form of ADC counts, the first thing that must be done is to convert this data into a number of photo electrons (p.e.) for each pixel. This calibration process, which will be shortly introduced in the following, is done first in the chain of analysis steps. A comprehensive description can be found in [38]. After that, the calibrated data is used to extract, if possible, the parameters of the primary particle that caused the shower and hence the camera image. This reconstruction process, especially of the primary particle's energy, is explained in more detail in [34].

3.4.1 Calibration

When the data output that makes up a full camera image is read out upon the triggering of an event, two ADC counts are produced for each pixel, a high gain and a low gain value. These ADC counts are converted to a physically meaningful quantity, namely the number

[5] These numbers can be changed on hardware level
[6] see Section 4.3.2

of p.e. in each pixel. Before this calibration process has been done, no shower information can be extracted from the camera images.

For the conversion of the ADC counts to numbers of p.e., a series of parameters have to be determined, which are then used for the following calculations:

$$A^{\mathrm{HG}} = \frac{C^{\mathrm{HG}} - P^{\mathrm{HG}}}{\gamma_{\mathrm{e}}^{\mathrm{ADC}}} \cdot \gamma_{\mathrm{FF}} \tag{3.7}$$

$$A^{\mathrm{LG}} = \frac{C^{\mathrm{LG}} - P^{\mathrm{LG}}}{\gamma_{\mathrm{e}}^{\mathrm{ADC}}} \cdot \frac{\mathrm{HG}}{\mathrm{LG}} \cdot \gamma_{\mathrm{FF}} \tag{3.8}$$

Here A^{HG} and A^{LG} are the amplitudes in photo electrons for HG and LG, C^{HG} and C^{LG} are the raw ADC counts for both channels and P^{HG} and P^{LG} are the pedestal positions, i.e. the HG and LG ADC count of the corresponding PMT at background level illumination. Furthermore, the ADC-to-p.e. coefficient $\gamma_{\mathrm{e}}^{\mathrm{ADC}}$ is the HG ADC count which equals one photo electron. As this parameter can be determined only for the HG, A^{LG} has to be additionally multiplied with the ratio of the amplifications between HG and LG, here denoted HG/LG. Lastly, γ_{FF} is the flatfield coefficient which corrects for differences in the single PMTs not yet covered by the ADC-to-p.e. coefficient.

For the final amplitude, A^{HG} is chosen for values up to $\approx 150\,\mathrm{p.e.}$ and A^{LG} above $\approx 200\,\mathrm{p.e.}$ For intermediary numbers, a proportionally weighted average A between the two channels is calculated thus:

$$A = (1 - \epsilon) \cdot A^{\mathrm{HG}} + \epsilon \cdot A^{\mathrm{LG}}, \qquad \text{where } 0 \leq \epsilon \leq 1. \tag{3.9}$$

The pedestal values P^{HG} and P^{LG} as well as the HG/LG factor are calculated for every run. For the former, two the mean ADC counts of the pixels containing no signal are periodically computed. In the off-line analysis, i.e. the analysis that is done after data-taking, this is done by first identifying which pixels of a camera image are contaminated with Čerenkov light. Thereafter, a per-pixel average over ≈ 5000 events is calculated for the ADC counts of pixels containing only background light. The so gained averages are used as pedestal values for an observation period of about one month.

HG/LG is determined for every pixel by dividing the HG by the LG counts for values in the overlapping regime, where both channels are usable (30 - 150 p.e.). To gain enough statistic, this is done for a large number of events using all runs taken during four weeks. The calculated values are periodically updated by repeating this process.

In contrast, the gain factor $\gamma_{\mathrm{e}}^{\mathrm{ADC}}$ and the flatfield coefficient γ_{FF} are not calculated for every observation run. Instead they are regularly determined in dedicated calibration runs. For $\gamma_{\mathrm{e}}^{\mathrm{ADC}}$, a so-called "single photo electron run" is done, where the camera, whose lid is closed, gets illuminated uniformly by an inbuilt LED pulsing at 70 Hz and set to provide approximately one p.e. for every pixel. Every pulse triggers the camera to read out all pixel intensities and from the gathered events $\gamma_{\mathrm{e}}^{\mathrm{ADC}}$ is calculated by fitting it to a function describing the theoretical distribution.

To determine γ_{FF} special flatfield runs are taken, in which the camera gets homogeneously illuminated with a telescope dish mounted laser, which can be set to provide between 10 and 200 p.e. per pixel. In the later calibration the collected events produced from the laser flashes are used to calculate the flatfield coefficient for every pixel p according to

$$\gamma_{\mathrm{FF}} = \left(\frac{1}{N_{\mathrm{ev}}} \sum_{i=1}^{N_{\mathrm{ev}}} \frac{A_i(p)}{\langle A \rangle_i} \right)^{-1}, \tag{3.10}$$

where N_{ev} is the number of events in the run, $A_i(p)$ is the intensity determined for pixel p in event i through Equation 3.7 (with $\gamma_{\mathrm{FF}} = 1$) and $\langle A \rangle_i$ is the mean intensity for all pixels of the event i.

For the different calibration procedures, only the fully functioning, non-broken pixels of every event are used for the calculations. Broken-pixels are marked unusable and will be excluded, also from the later analysis. This marking can happen for various reasons, including bright stars in the field of view, hardware damage, intolerably fluctuating HV, too frequent or infrequent occurrence of large signals (> 30 p.e.), shooting stars, etc. The usability of pixels is permanently monitored when the cameras are in use. In case a pixel is unusable for one gain, it is often still possible to switch to the other.

3.4.2 Image Cleaning

Before the actual reconstruction of the shower parameters can be applied, the noise that is still remaining in the camera images after calibration must be dealt with. This noise is mostly caused by the usual electronic fluctuations of the PMTs and by diffuse light, e.g. from faint stars called the night sky background (NSB). To eliminate it, the H.E.S.S. analysis applies a tail-cut algorithm, comprehensively described in [39], which takes advantage of the fact, that pixels containing only NSB are distributed entirely random on the camera image, while pixels with Čerenkov light most likely appear in clusters.

This algorithm demands that pixels assumed to contain a signal have at least 10 p.e. or 5 p.e. themselves while at the same time at least one of their neighbors has more than 5 p.e. or 10 p.e. respectively. All pixels not meeting this requirements are excluded from the analysis.

3.4.3 Shower Image Parametrization

For the later reconstruction of the origin and energy of the primary particle as well as its identification as gamma-ray or hadronic background, a number of parameters are calculated from the elliptical shower images, as suggested by Hillas in [40]. These so-called Hillas parameters, which are depicted in Figure 3.9, consist of:

- the *length* and the *width*, representing the lengths of the shower ellipse's semi-major and semi-minor axes
- the *orientation*, i.e. the angle θ between the semi-major axis and the camera's abscissa
- the *image size*, defined as the total number of p.e. within the ellipse
- the image's *center of gravity* (COG), which is the first moment of the ellipse
- the *local distance* meaning the distance of the camera center from the COG

3.4.4 Event Selection

To improve the quality of the later reconstruction, the events recorded have to be filtered against certain criteria. As a first step, low quality events that would lead to poor reconstruction results are sorted out. This is done by applying cuts to the extracted Hillas parameters. The values for these cuts have been optimized using Monte Carlo simulation studies in combination with real data. As these studies showed that optimal cuts depend on the nature of the source, especially its luminosity and spectrum, different sets of cuts exist for different source types, including a standard set that is also used when searching for new sources.

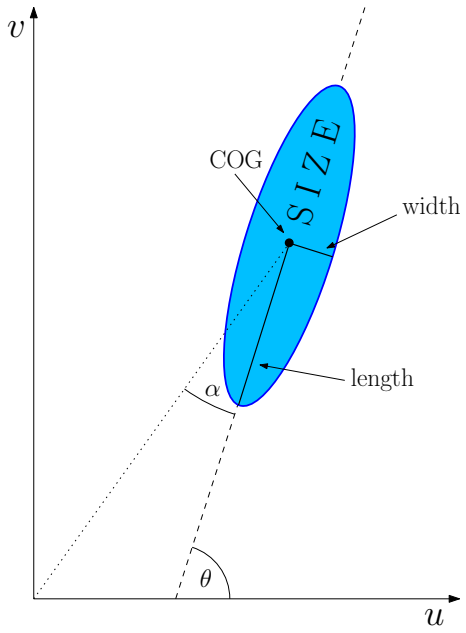

Fig. 3.9: *Sketch showing the Hillas parameters used to describe the elliptical images of the air showers*

For discarding low quality events, cuts on the local distance, the image size and the telescope multiplicity are used. This is because events below a certain overall p.e. count are difficult to reconstruct and images too far from the center of the camera get cut off at the edges. Lastly, the telescope multiplicity, which is for all cuts at least 2, filters out the single telescope events for which no stereoscopy can be used.

The second step is to filter out as much cosmic-ray background, i.e. mostly proton events, as possible before the events undergo the reconstruction algorithms. This is highly important as the background events would otherwise massively outshine the gamma-ray signals. Here the applied cuts take advantage of the more lateral-spread nature of the background events' hadronic shower images[7]. If all air showers observed would occur at the same height and under the same angle to the telescopes, simple cuts to only the width and length Hillas parameters would be possible. However, the shape of an air shower also depends on the relative direction of the shower axis, the primary particle's energy, the shower's impact parameter, i.e. the distance of the shower axis to the telescopes, and the zenith angle[8]. With increased energy of the primary particle, more particles are produced in the cascade, leading to a larger image size, width and length of the ellipses. Furthermore, with increasing zenith angle the shower maximum is further away from the telescopes and thus a larger area on the ground is illuminated, which means a smaller percentage of light is collected by the telescopes.

To avoid the mentioned dependencies in the parameters used for event selection, the so-called *mean reduced scaled width* (MRSW) and mean reduced scaled length (MRSL) are calculated. This makes it possible to use the same cut limits for all events. The formula is here presented only for MRSW as it is analogously defined for MRSL:

$$\mathrm{MRSW} = \frac{1}{N_{\mathrm{tels}}} \sum_{i=1}^{N_{\mathrm{tels}}} \frac{w_i - \langle w \rangle_{\mathrm{MC}}}{\sigma_{\mathrm{MC}}} \tag{3.11}$$

[7] see Section 3.1.2

[8] i.e. angle between the zenith and the optical axes of the telescopes

Cut	Image Size	θ^2	Local Distance	MRSW		MRSL	
	min.	max.	max.	min.	max.	min.	max.
Standard	80 p.e.	0.0125°	2°	-2.0	0.9	-2.0	2.0
Hard	200 p.e.	0.1°	2°	-2.0	0.7	-2.0	2.0
Loose	40 p.e.	0.4°	2°	-2.0	1.2	-2.0	2.0
Extended	80 p.e.	0.16°	2°	-2.0	0.9	-2.0	2.0

Table 3.1: *Overview of the different image quality cuts applied by H.E.S.S.*

In this equation, N_{tels} is the number of telescopes that have recorded the event, w_i is the width of the shower ellipse imaged by telescope i, while $\langle w \rangle_{\text{MC}}$ and σ_{MC} are the width's expectation value assuming a gamma-induced shower and its standard deviation respectively.

For the determination of the values $\langle w \rangle_{\text{MC}}$ and σ_{MC}, lookup tables for electromagnetic showers are generated via extensive Monto Carlo simulations with varying impact parameter, size and zenith angle of the observing telescopes. The term in the sum is thus a measure of how different the width of a particular shower is from the expected width of a gamma-ray shower with the same set of Hillas parameters.

Through the application of cuts on the MRSW and MRSL, it is possible to scale down the background-to-signal ratio by a significant factor, from around 100:1 to approximately 1:1 under good conditions. Their minimal and maximal values also depend on the used set of cuts, which Table 3.1 gives an overview of.

3.4.5 Geometric Reconstruction

After the raw data has been calibrated and most of the background events have been filtered out through the event selection procedure, the remaining camera images are put through the reconstruction algorithms to extract the physically relevant data about the primary particle that caused the imaged air shower, i.e. its energy and its direction.

As one side of the semi-major axis of a shower ellipse points towards the source of the shower, there is a straightforward approach to reconstruct the origin of the primary particle applicable with stereoscopic observation. Several camera images of the same shower are superimposed and subsequently the intersection point of all axes is determined. When using more than two shower images, several intersection points exist, as the calculated orientations of the ellipses are not free from errors. For N camera images from distinct telescopes there are $N(N-1)/2$ intersection points. These points are added up to a weighted average with weighting according to their precision in reconstruction as defined by the following formula:

$$w_{ij} = \frac{\sin\left(\theta_i - \theta_j\right)}{\left(\frac{1}{s_i} - \frac{1}{s_j}\right)\left(\frac{w_i}{l_i} - \frac{w_j}{l_j}\right)}. \tag{3.12}$$

Here, w_{ij} is the weight of the intersection point for two different camera images i and j, $\theta_{i/j}$ the orientation, $s_{i/j}$ the size, $w_{i/j}$ the width and $l_{i/j}$ the length of the ellipses respectively.

This weighting favors intersection points with perpendicular angles, as these have, for trigonometry reasons, the highest precision, as well as images with large size and ratio of length to width, as such images have the most accurate reconstructed parameters. Four superimposed camera images from a 7 TeV gamma-ray event as well as their shower axes and reconstructed ellipses are shown in Figure 3.10.

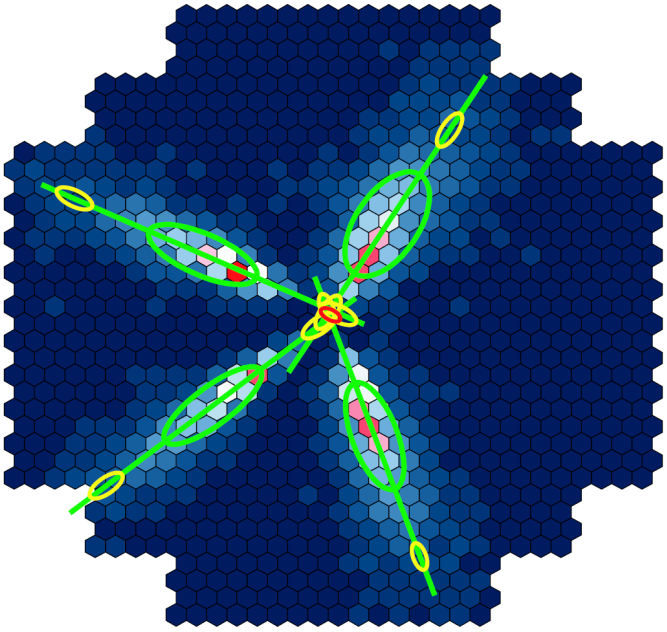

Fig. 3.10: *Geometric reconstruction technique applied to a simulated 7 TeV γ-ray event. Shown are the four camera images superimposed on one common plane. The reconstructed Hillas ellipses and shower axes are overlain in green, the estimated source regions on both side of the ellipse in yellow and the weighted average of all intersection points as red error ellipse. (Figure adopted from [34])*

The impact parameter, i.e. the distance of the shower axis to the telescopes, is also reconstructed using this geometric approach. It is determined by the intersection of the shower axes on a plane perpendicular to the telescopes' pointing direction in a common coordinate system. Using this method, the impact parameter can usually be determined with an accuracy of 10 m for showers falling within 200 m of the telescope array's center. The knowledge of this parameter is crucial for the later estimation of the total amount of Čerenkov light in the shower, which is proportional to the energy of the primary particle.

3.4.6 Estimation of Gamma-Like Background

Even with the event selection cuts described in Section 3.4.4, the maximum ratio of background to signal events that can be reached is about 1:1. The remaining background is either comprised of hadronic events that are "gamma-like" in shape or diffuse gamma-rays that did not come from the observed source. Unlike gamma-ray events from real sources, the latter are distributed uniformly across the sky and are produced from cosmic-ray interactions, e.g. with interstellar gas or photon fields.

Before quantitative results about the observed sources can be given, this remaining background has to be removed from the data. This is done by collecting events from two regions on the sky, the first containing the source, called the "on region", and the second, observed under conditions as equal as possible and containing no known localized sources, called the "off region" and then subtracting the gathered off from the on events as described in 3.4.7.

There are different methods to obtain off events for a given source. One approach applied less often by H.E.S.S. is the ON/OFF method, with which, for one source, two observations

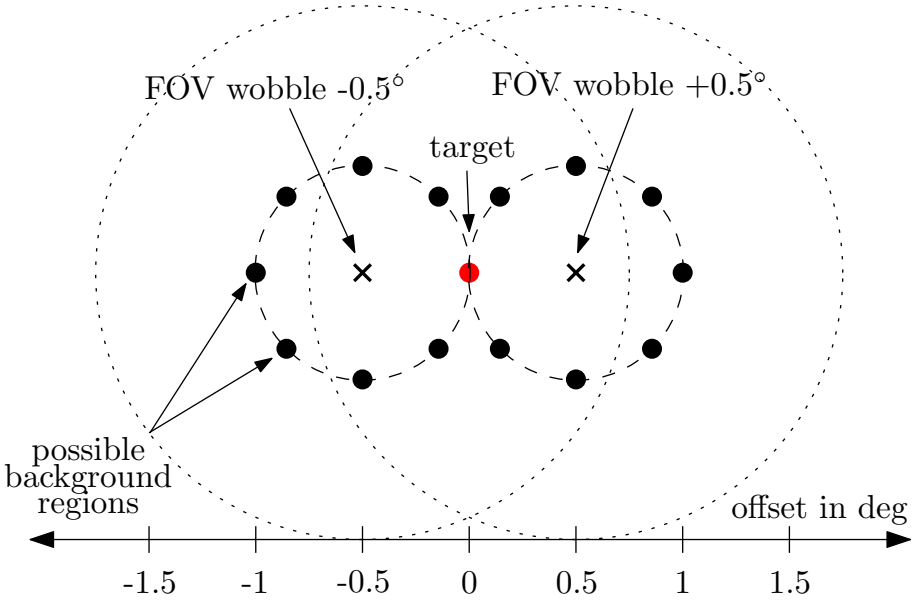

Fig. 3.11: *Sketch of possible good background regions (black discs) for an observation in wobble mode with ±0.5° offset. The dotted circles enclose half of the possible field of view (2.5°)*

are scheduled. One targets the source directly and the other aims at an adjacent region in the sky known to be devoid of sources. The disadvantages of this method are that more observation time is needed and the fact that it is difficult to ensure equal conditions in both observations. Therefore, H.E.S.S. mostly uses a technique for gathering off data called *wobble mode*, which takes advantage of the array's large field of view. Here the telescopes do not target the source directly, but under a certain angular offset, typically 0.5°. This provides several good off regions inside the field of view, assuming a radially symmetric behavior of the cameras. Figure 3.11 shows possible background locations for a wobble mode observation, which are located on circles with the wobble offset as radius around displaced camera centers.

3.4.7 Statistical Interpretation

The number of on events N_{on} and the off events N_{off} gathered for a test region are used to calculate a quantitative measure, the excess count, that represents the gamma-ray signal strength over the background, according to the following equation:

$$N_{\mathrm{ex}} = N_{\mathrm{on}} - \alpha N_{\mathrm{off}}. \tag{3.13}$$

α is a normalization factor required to compensate for the possibly unequal conditions under which the off data has been gathered, namely differences in exposure time as well as in the size and system acceptance ϵ^{γ} of the detection region. It is defined as

$$\alpha = \frac{\int \epsilon^{\gamma}_{\mathrm{on}}(\theta_x, \theta_y, \phi_{\mathrm{zen}}, t)\mathrm{d}\theta_x \mathrm{d}\theta_y \mathrm{d}\phi_{\mathrm{zen}}\mathrm{d}t}{\int \epsilon^{\gamma}_{\mathrm{off}}(\theta_x, \theta_y, \phi_{\mathrm{zen}}, t)\mathrm{d}\theta_x \mathrm{d}\theta_y \mathrm{d}\phi_{\mathrm{zen}}\mathrm{d}t}, \tag{3.14}$$

where θ_x and θ_y denote the position in the field of view, ϕ_{zen} the zenith angle and ϵ^{γ} the system acceptance, which describes the probability that a γ-event is triggered on and passes the selections cuts. It is dependent on a variety of conditions. To start with, the

Earth's magnetic field influences the shower development, which results in a dependency to the orientation of the telescopes. This dependency is also due to the fact that increasing zenith angles lead to the detection of more showers with large impact parameters, as they are produced further away from the telescopes and thus illuminate a larger area on the ground. Another variable is the local distance, which strongly influences the acceptance as events that occur near the edges of the camera tend to get filtered out more often. A last contribution comes from the primary particle's energy, because higher energies lead to larger camera images which normally are more likely to pass the cuts, if they are not exceptionally big. $\epsilon^{\gamma}_{\mathrm{on}}$ and $\epsilon^{\gamma}_{\mathrm{off}}$ can be determined on a run-by-run basis or with suitable off runs. While doing so, a radial symmetry is assumed which can be done in good approximation and reduces the problem to one dimension.

As the excess count gives no direct information on the probability that a signal comes from an actual gamma-ray source and is not just a background fluctuation, the statistical significance S for the former case is an important measure. A straightforward approach of calculating it, is with the following formula, which represents the ratio of excess events over their standard deviation

$$S = \frac{N_{\mathrm{ex}}}{\sigma(N_{\mathrm{ex}})} = \frac{N_{\mathrm{on}} - \alpha N_{\mathrm{off}}}{\sqrt{\alpha\,(N_{\mathrm{on}} + N_{\mathrm{off}})}} \tag{3.15}$$

However, the approach above is inaccurate for low excess event count rates. To attain better results, the H.E.S.S. standard analysis usually calculates the significance as suggested by Li and Ma in [41], i.e. as a hypothesis test with the null hypothesis being that the signal is only a background fluctuation. S can then be expressed as:

$$S = \sqrt{2\left\{N_{\mathrm{on}} \ln\left[\frac{1+\alpha}{\alpha}\left(\frac{N_{\mathrm{on}}}{N_{\mathrm{on}} + N_{\mathrm{off}}}\right)\right] + N_{\mathrm{off}} \ln\left[(1+\alpha)\left(\frac{N_{\mathrm{off}}}{N_{\mathrm{on}} + N_{\mathrm{off}}}\right)\right]\right\}}. \tag{3.16}$$

As it has been shown by Monte Carlo simulations, this approach is more stable with low event numbers, particularly if $\alpha \neq 1$.

4 The H.E.S.S. Data Acquisition Software

The H.E.S.S. data acquisition software (hereafter HESSDAQ) performs the various data handling processes between the hardware components of the telescope array. This includes the readout, flow control, monitoring, storage and processing of gathered data. It has been implemented in the programming languages `C++` and `Python`, taking full advantage of their object-orientated functionality, and was designed as a system of distributed processes, each of which is designated for a particular task. The modular approach chosen for the HESSDAQ allows its programs to run on an arbitrary number of computers. All programs base on the object-orientated library `DASH` developed by the H.E.S.S. collaboration as a framework for all DAQ processes. For a good overall stability, flexibility and performance, the software has been designed for and runs on Linux-based operating systems, although it is not internally dependent thereon and could also be ported to other systems.

In the following Chapter, the functionality and architecture of the HESSDAQ will be explained. Thereafter, the new automatic response system for GRB alerts distributed through the GCN will be presented along with a discussion of the changes that had been necessary to the software. For easier reading, the names of HESSDAQ processes are written in *italic* letters (e.g. *CameraReader*), software states and transitions[1] with SMALL CAPITALS (e.g. PAUSED) and the `typewriter` font is used for actual software names (like `Python`), programming related classes and class libraries (e.g. `Distributor`, `DASH`) and nameserver entries[2] (e.g. `CT4/Tracking`).

4.1 Specifications

In the following, the basic specifications of the HESSDAQ will be described, including the framework for inter-process communication, the hardware of the computer cluster and the system and format of data storage.

4.1.1 Inter-Process Communication

The distributed nature of the HESSDAQ requires a way of data exchange between its comprising processes. This has been implemented through the use of the open-source project `omniORB`[3], an implementation of the stable and reliable industry standard CORBA, which provides programming language interfaces to both `C++` and `Python`. `omniORB` provides a convenient interface for inter-process communication (IPC) of processes both on the same and on different, but networked, machines. For easy organization of the participating programs, a central nameserver is also supplied which hierarchically manages the communication partners in a tree-like structure where every leaf is a process and and every branch is a logical part of the DAQ system, called Context. Entries are in the form `Branch/SubBranch/Leaf`, e.g. `CT1/Camera`, referring to the process controlling the camera of the first Čerenkov telescope (CT), or `Array/RunManager` for the process scheduling all calibration, test and observation runs.

[1] see Section 4.2.1
[2] see Section 4.1.1
[3] more information can be found at `http://omniorb.sf.net`

4.1.2 Computer Cluster

The on-site computing hardware is a mixture of very different systems as it has undergone a number of partial modernizations. This inhomogeneity does not compromise the functionality of the system due to the modular, hardware-independent approach. The current list of hardware comprises around 30 individual PCs, ranging from the early 800 MHz single CPU[4] systems, to modern 2.8 GHz quad-cores. All are connected to a 100 MBit Ethernet network with 1 GBit hardware switches that route the data flow.

4.1.3 Data Management System

For a fast and efficient centralized data access and storage, the HESSDAQ utilizes the MySQL[5] database (DB) management system. To further ease the database handling during programming, a front-end[6] to the MySQL interfaces called `simpletables` has been developed and is available both for `C++` and `Python`. This front-end has several advantages, among them the often employed possibility to create so-called *sets*, which are subtables linked to rows inside conventional MySQL tables. This is used for example in the table that stores the scheduled observation runs, as there is a row for each day in this table and each of these rows also constitutes a set containing the telescope runs made on that day. Furthermore, if a set has to be updated, nothing has to be deleted from the database. Instead, the old set is hidden by the updated version, which is then the only one externally visible. Yet, it is easily possible to recover the old underlying versions, if need be. Thus this contributes a good backup solution and the possibility to trace back changes in time.

For consistency, all database access by the HESSDAQ is done via `simpletables`, and every process that needs to be configured or needs to write updated configurations reads the data from and stores it to the central database.

4.1.4 Data Format

From the outset, both the design of the H.E.S.S. offline analysis software, i.e. the programs later applying the reconstruction algorithms to the data and building the skymaps, spectra, etc., and the design of the HESSDAQ incorporated ROOT[7], an object-oriented data analysis framework developed at CERN. This allows for convenient handling of graphical offline and online analysis, compressed data storage, buffered data flow among other things. Data from the various hardware components gets converted to the H.E.S.S. internal ROOT format as early as possible, which ensures homogeneity in the handling of data by all involved HESSDAQ processes.

4.2 Components

In this Section, the common features every HESSDAQ process incorporates will be introduced. These comprise the process control, a messaging system and a way of data transport. All of these are implemented through inheritance[8] form various `DASH` routines,

[4] Central Processing Unit

[5] extensive documentation available at `http://www.mysql.com`

[6] A front-end is an interface, that is more user-friendly than the underlying software it provides access to.

[7] visit `http://root.cern.ch` for more information

[8] Inheritance is an object-oriented programming concept, making it possible to reuse already programmed routines for new parts of the software. For example, most processes of the HESSDAQ inherit the possibility to send and receive messages, making it unnecessary to reprogram that functionality for every process. Thus inheritance is intended to help reuse existing code with little or no modification.

taking advantage of the softwares object-oriented design.

4.2.1 Process State Management

To coordinate the efforts of the HESSDAQ processes each of them inherits an interface from the `DASH` class[9] `StateController`, which allows them to indicate their current progress to the outside with an externally visible software state. The list of allowed states comprises four elements: SAFE, READY, RUNNING or PAUSED. Transitions between these four are also handled by this interface, which also checks for the validity of a requested state transition, initiating it only for allowed requests. Possible state transitions are: CONFIGURE, GOTOSAFE, START, STOP and RESUME. Figure 4.1 displays which transitions are allowed between the four states.

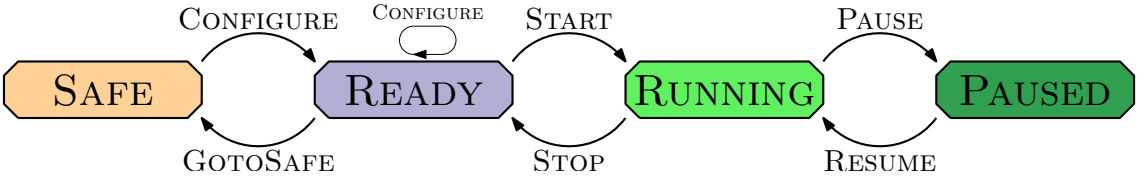

Fig. 4.1: *Sketch of possible process states and allowed transitions between them*

All external process controlling is done via the `StateController` interface and only the mentioned states of a process are visible from the outside, which helps to keep the system in well defined overall conditions.

As this interface is provided by every process and their tasks in the HESSDAQ are profoundly different, the meaning of a state or state transition is not fixed but dependent on the particular processes. Table 4.1 gives a comprehensive overview of all processes with their names as they are registered at the `omniORB` nameserver (in the form `Context/Name`), their function inside the HESSDAQ and the respective meaning of the available states. The meaning of the transitions can be derived from this list as the actions necessary to transfer the processes back and forth between the particular states. The PAUSED state with the corresponding PAUSE and RESUME transitions is not listed, because it is normally only used by the *CameraReader* processes, which receive the data from the Čerenkov cameras and will be described in Section 4.3.2. While other processes can also undergo the transitions PAUSE and RESUME, i.e. change to and leave the state PAUSED, this will normally not entail any special action, which means that the same conditions apply as in the RUNNING state.

However, the GRB alert response system, uses the PAUSE and RESUME transitions of various processes for implementation specific purposes, which will be described comprehensively in Chapter 5.

[9] A class is a object-oriented template describing an amount of data and the routes to modify it.

Name	Task	SAFE	READY	RUNNING
`Array/ResourceHandler`	Starts and monitors the HESSDAQ processes	No action	DB configuration read & monitoring started	Same as in READY
`Array/CentralTrigger`	Controls and monitors the central trigger hardware	Trigger deactivated	Configured from DB & trigger initialized	Checking trigger status
`CT/Camera`	Main interface for the following four camera subprocesses	All components SAFE	All components READY	All components RUNNING
`CT/CameraTrigger`	Controls the camera trigger	Stopped	Configured from DB	Running
`CT/CameraLid`	Controls the camera lid	Closed	Open	Open
`CT/CameraLidLED`	Controls the positioning LEDs on the inside of the camera lid	LEDs switched off	Configured from DB & LEDs on	LEDs on
`CT/CameraHV`	Controls the camera HV (nominal value is set in database)	Off	400 V	Nominal value
`CT/FlatField`	Controls the flatfield LEDs and filterwheels in flatfielding runs	Hardware connection closed	LED and filterwheel configured & running	Running
`CT/Tracking`	Controls the telescope tracking	Stopped	Received coordinates & slewed on target	Tracks on target
`CT/LidCCD`	Controls the CCD mounted on each camera lid (used in pointing runs)	Stopped	CCD Configured from DB	Running
`CT/SkyCCD`	Controls the CCD mounted beside each telescope (used in pointing runs)	Stopped	CCD Configured from DB	Running
`CT/Radiometer`	Controls the paraxial radiometers mounted on the telescopes	Readout stopped	Configured from DB & readout running	Like READY
`CT/StarController`	Checks for necessary moonless astronomical darkness, looks for bright stars in the field of view	Stopped	Configured from DB & registered at *CameraReaders*	Running
`Node/Analysis`	Receive data from according *CameraReaders* and perform online analysis. Results are pushed to the *AnalysisServer*	Stopped	Configured from DB	Connected to the *CameraReaders*
`Node/Receiver`	Receive and convert camera raw data	All files closed	Configured from DB & prepared for data reception	Receiving or converting data
`SlowControl/ Receiver/...`	Receive data from various *Controllers* and save it on hard disk	Stopped	Configured from database and registered at *Controllers*	Running
`SubArray/Receiver/...`	Same as above	Same as above	Same as above	Same as above
`SlowControl/ Displays/...`	Show various monitoring diagrams for the shift-crew	Display windows closed	Configured & registered at *Receivers*	Display windows are drawn
`SubArray/Displays/...`	Same as above	Same as above	Same as above	Same as above
`SubArray/Trigger/ Connector`	Looks for unoccupied *CameraReaders*	Stopped	Configured the central trigger	Periodically sending next `Node` ID to central trigger
`SubArray/Services/ AnalysisServer`	Gathers data from the *Analysers* and shows displays for the shift crew	Stopped, Displays closed	Configured from DB	Collecting data, displays are shown
`SubArray/Services/ CameraConfig`	Provides configuration for the camera *Controllers*	Configuration cleared	Configured from DB	Configured all cameras
`Services/Summary`	Writes a summary of finished runs for Internet distribution	No action	Configured from DB	Writing summaries for unprocessed runs
`Atmosphere/Meteo`	Collects data from the weather monitoring instruments	Receives data	Receives data	Receives data
`Atmosphere/ Transmissiometer`	Collects data from the sky temperature measuring Transmissiometer	Receives data	Receives data	Receives data

Table 4.1: *Listing of processes with their nameserver names, their tasks, possible states and their particular meanings.*

4.2.2 Contexts and Managers

The Context scheme already mentioned above simplifies the organization of the currently around 150 independent processes making up the HESSDAQ. Each Context is filled with several processes that belong to the same logical task group. The `CT1 - CT4` Contexts e.g. contain all processes controlling the particular telescope's hardware.

Communication with processes belonging to different Contexts is not done directly. Instead, every Context has its own *Manager*, whose standard functionality is inherited through the `DASH ManagerBase` class. A *Manager* is responsible for all other processes in the same Context and acts as an interface to the outside. This encapsulation strategy helps to provide a standard way of communication with different software parts as only the respective *Manager* needs to now how to deal with its "active", i.e. affiliated processes.

Another task of the *Managers* is to keep all their active processes in the same state, namely the momentary state of the *Managers* themselves. So when another process invokes a state transition on a *Manager*, it has to invoke the same transition on all its processes. While doing so, it is also responsible for enforcing adherence to the dependency scheme stored in the central database. This scheme has entries in the form of: `ContextA/ProcessX` depends on `ContextB/ProcessY` (e.g. `CT/Tracking` depends on `SubArray/Receiver/Tracking`). When the dependencies are in the same Context, the particular *Manager* simply waits for `ProcessY` when invoking START, CONFIGURE or RESUME on `ProcessX` and the other way round for the remaining transitions. If the Contexts are different, both involved *Managers* communicate to ensure the proper starting and stopping order. The currently employed dependency scheme is shown in Table 4.2, in which all processes are listed with their respective nameserver entries[10].

When a *Manager* invokes a state transition on its affiliated processes, for each of them a separate subroutine is started, in which the transition is invoked. These subroutines are processed simultaneously, which has the advantage that independent processes do not have to wait for each other when performing their respective state transition.

4.2.3 Data Transport

For data exchange between two processes A and B of the HESSDAQ, two different transport modes are provided by `DASH` through several classes.

Push Mode: Data gets "pushed" from a `Sender` inside A to a `Buffer` inside B in a way that ensures the correct transfer of every byte and therefore excludes data loss. The `Buffer` caches the data blocks coming from A and forwards them to a `MemoryManager`, which sorts them into the process memory and also provides an interface for external data "skimming". Push mode is used for example when hardware components send their data to the controlling processes.

Pull Mode: The interface provided by the `MemoryManager` of A can be used when only some of the data available for this process is needed by B and data losses are tolerable. In such a case, A and B can connect their `MemoryManager` instances directly and B "pulls" data form A in desired portions and intervals. This mode is for example applied when monitoring data for the various displays in the H.E.S.S. control room is obtained by the particular processes.

[10] compare with Table 4.1

Process	Depends On
CT/Tracking	SubArray/Receiver/Tracking
CT/CameraTrigger	Node/Receiver
CT/CameraTrigger	CT/CameraHV
CT/CameraTrigger	CT/CameraLid
CT/CameraTrigger	CT/Camera
CT/CameraHV	CT/Camera
CT/CameraLid	CT/Camera
CT/CameraLED	CT/Camera
CT/CameraLid	CT/Tracking
CT/CameraHV	CT/CameraLED
CT/Camera	SubArray/Receiver/Trigger
SubArray/Trigger/Connector	Node/Receiver
SubArray/Trigger/Connector	SubArray/Receiver/Trigger
Node/Receiver	SubArray/Receiver/CameraRate
Node/Receiver	SubArray/Services/CameraConfig
SubArray/Trigger/Connector	CT/CameraTrigger
CT/Radiometer	SubArray/Receiver/Radiometer
Node/Receiver	Node/Analysis
SubArray/Services/AnalysisServer	SubArray/Services/CameraConfig
Node/Analysis	SubArray/Services/AnalysisServer
SubArray/Receiver/Camera	SubArray/Services/CameraConfig

Table 4.2: *Currently employed dependency scheme of the H.E.S.S. data acquisition software*

4.2.4 Messaging Interface

With the `Message` class the `DASH` library also provides a communication interface for the broadcasting of messages. Each HESSDAQ process that inherits from the `StateController` class (i.e. "is" a `StateController`) indirectly also inherits from the `Message` class. Therefore, every process with software states as described in Section 4.2.1, which is the case for nearly all HESSDAQ programs, incorporates this feature.

Before messages can be exchanged, an one-way connection between the sender and the receiver, which can already have other associated senders, has to be established. After that, every message composed at the sender side will also be transmitted to all its registered receivers. During this procedure it is not possible for the sender to choose which of its receivers should get the outgoing message, i.e. the message is always sent to all of them. When a message is distributed, it is prefixed with date and time and subsequently written to the receivers' and sender's output stream, which by default is written in respective log files named after their nameserver entries (e.g. `CT1_Tracking.log`).

Messages are classified into five different types, each with an arbitrary explanatory text attached to it. Upon reception a type specific action to inform the shift crew is performed by the respective process. The available types and standard reactions are listed in Table 4.3

In addition to these type specific actions, the displaying of a notification window for the shift crew can be enforced upon reception of an arbitrary message type. To do this, the message text must begin with certain symbols (`***` or `+++`) and a message connection has

Message	Action
Info	No action
Caution	Sound is played
Warning	Sound is played and a pop-up windows displayed
Error	Warning reaction plus stop of data taking
Fatal	Error reaction plus sending all processes to SAFE state

Table 4.3: *List of different message types and their standard reactions*

to be open between the graphical user interface[11] and the process sending the message[12].

4.3 Architecture

In this Section the different tasks of the HESSDAQ along with the processes accomplishing them will be explained. This comprises the control of all its processes, the control and readout of the hardware in general and for the Čerenkov cameras, the method of data storage and organization of stored data, the visualization of observation data for the shift crew and the online analysis.

4.3.1 Process Control

The distributed nature of the HESSDAQ with its many processes running on a fair number of individual computers makes a central process controlling instance necessary. This service is rendered by two types of programs, the *ResourceHandler*, which is started only one time, and the *HostHandlers*, of which there is one instance per cluster computer. As the central instance, the *ResourceHandler* informs each *HostHandler* about the processes that are supposed to run on the same host. The actual work is done by the *HostHandlers* by performing the following actions:

- Starting all affiliated processes if requested by the `ResourceHandler`, e.g. when the HESSDAQ is powered up.
- Monitoring of their affiliated processes' status, e.g. if they are still running and responsive.
- Restarting an affiliated process in case of both intentional termination and unwanted crashes.
- Notifying the *ResourceHandler* of disappeared and restarted processes, which then spreads this information to all other processes in case some of them need to react accordingly.

Thus, when a fresh start of the complete DAQ system is required, which is accomplished in under 2 minutes at the moment, the *ResourceHandler* and the *HostHandlers* are the only processes that need to be started externally.

4.3.2 Hardware Readout and Control

All hardware components of the experiment are connected to the HESSDAQ with specialized `Controller` processes. Their task is to receive the data from their affiliated hardware

[11] see Section 4.4.1

[12] This is by default the case for the *RunManager*, the *ResourceHandler* and the *GCN-Alerter*, described in Sections 4.4.2 and 4.3.6

resource. For this, every *Controller* understands the communication protocol of its assigned component. The remaining readout procedure is standardized for every hardware component with the exception of the telescope cameras, for which it is described separately.

Standard Procedure

For regular hardware components, the *Controllers* immediately convert all received data to the H.E.S.S. data format. After that, they "push" this data into so-called *Receiver* processes, which both write it into `ROOT` container files on hard disk and supply a "pull" interface via a `MemoryManager` object. This can be used by other processes of the HESSDAQ to acquire parts of the data stream for their purposes, for example the displaying of monitoring graphs for the shift crew, the real-time monitoring of critical values (e.g. the temperature of the camera drawers) or the online analysis. The concept is schematically depicted in Figure 4.2.

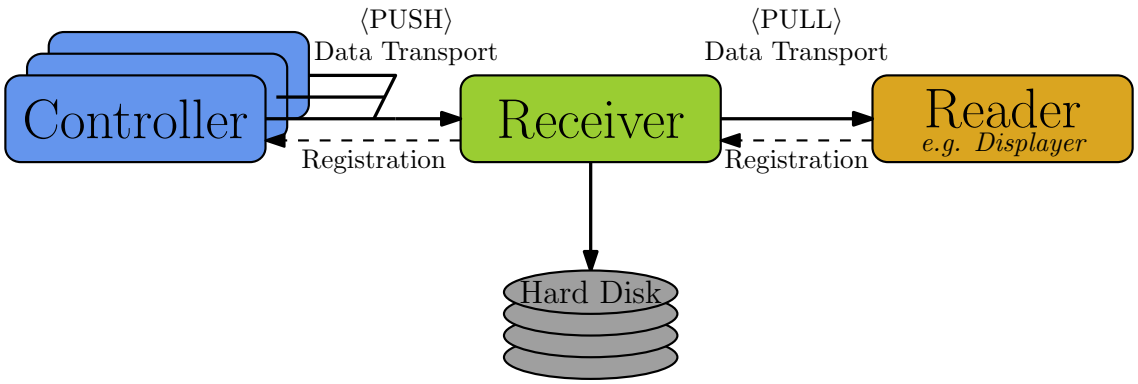

Fig. 4.2: *The H.E.S.S. standard hardware readout and data distribution chain*

To organize the various *Receiver* processes, they are all registered within the `SlowControl/Receiver` subbranch of the `SlowControl` Context.

Readout of the Čerenkov Cameras

The straightforward readout chain of the remaining hardware cannot be applied for the Čerenkov cameras because of their large data bandwidth. Even though a big part of the recorded events gets discarded by the hardware trigger system, the bandwidth of outgoing camera data is still too large to be handled in real-time by just one *Controller* process. This is because with today's technical standing the computing power of a single cluster PC is not sufficient for this task.

To compensate for that shortage, the camera *Controller* does not do the data conversion into the H.E.S.S. format itself but delegates this task to several instances of a specialized receiver process, the *CameraReader*. Each of them is running on an individual computer or has at least one processor core for itself and is registered as `Node01/Receiver`, `Node02/Receiver`, etc. at the central nameserver. The only other software part inside this Context, besides the always present *Manager*, are the `Node/Analysis` processes, which are responsible for the real-time online analysis of the data received by the *CameraReaders*[13]. Therefore, it is common to use the term *Node* to refer to one independent Context of camera data processing programs, especially the contained *CameraReader*.

[13] described in more detail in Section 4.3.5

While in normal operation, the cameras will send their raw data stream for a fixed time interval t_{send}[14] to one of the available *Nodes*. A process part called `Connector` inside the *Controller* for the central trigger system, which is called *CentralTrigger*, is responsible for maintaining a list of unoccupied and occupied `Node/Receivers` and assigning free instances to the cameras at the chosen time intervals. The distinction between a busy and a free *Node* is done by self-invoking of the PAUSE transition of idle *CameraReaders*, which are in the RUNNING state during data processing. Thus the `Connector` collects unoccupied *Nodes* by looking for PAUSED instances and sends them to RUNNING if they are next in line.

After a camera is finished sending to one particular receiver, another software part of the *CentralTrigger* process dubbed `Distributor` sends the triggering information of the last t_{send}-block to the Node that received it. This information is needed by the *CameraReaders* for the proper packing of the data into H.E.S.S. data files and contains, among other things, the total number of events in the block alongside with the number of telescopes that triggered and had valid data for each event. When the conversion is done, the data files are written to hard disk, as can be seen in Figure 4.3, which depicts the whole readout chain.

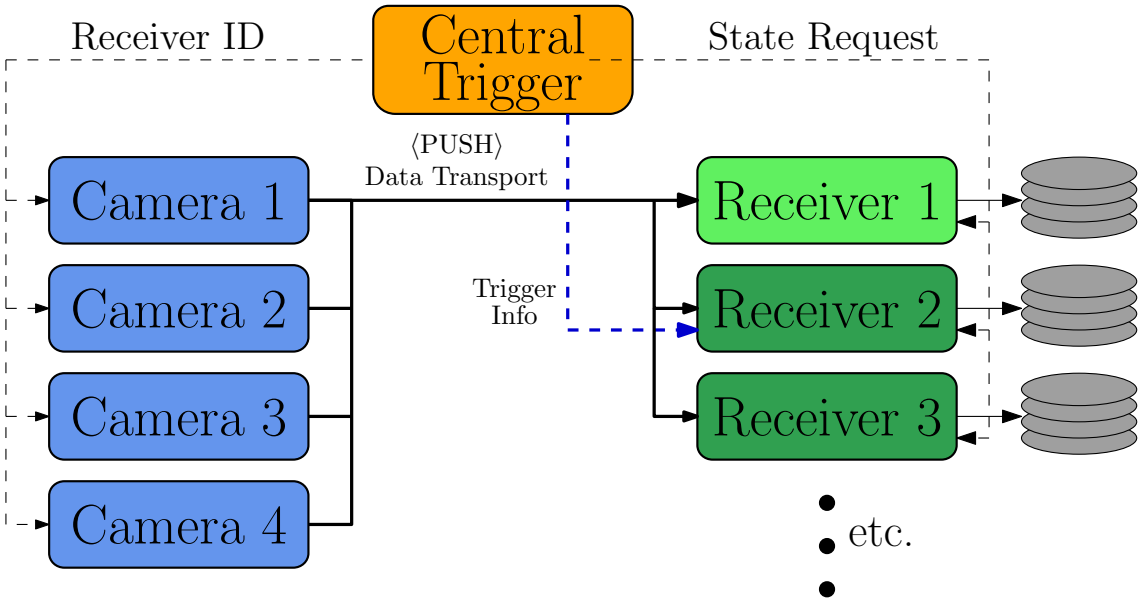

Fig. 4.3: *The data readout chain for the H.E.S.S. cameras*

Like the standard receivers, the *CameraReaders* also supply an interface for pulling selected data out of the stream. This is for example used by the software parts performing the real-time preliminary online analysis, described later in Section 4.3.5.

As an exception to all other hardware handling *Controllers*, the *CameraControllers* harbour several subprocesses handling different camera components, e.g. internal trigger system, the high voltage and the flatfield LEDs. Nevertheless, these subprocesses appear to the HESSDAQ as single *Controllers* with separate nameserver entries, e.g. `CT2/CameraTrigger`.

[14] t_{send} is usually 4 s and can be configured in the central database

4.3.3 Data Storage

The mechanism to store the data collected by the various hardware *Controllers* works with several instances of a non-specific *Receiver* process, one for each logical group of hardware controllers, i.e. one for all tracking related hardware and one for all weather monitoring devices. For this purpose, every *Receiver* can simultaneously and asynchronously deal with data from several *Controllers*, each of which it priorly has to register with.

After registration the *Controllers* send their data using the push mode, described in Section 4.2.3. When the data recording is finished, the *Receivers* will unsubscribe from the *Controllers*. This leads to the emptying of all buffers and the stopping of the transfer. If one of the involved processes has to be restarted for whatever reason, the data transport channels will automatically be reestablished.

4.3.4 Data Visualization

To supply visual feedback for the on-site shift crew during data taking, a generic program called *Displayer* is provided. During normal observation runs, several *Displayer* processes are running simultaneously. These are registered alongside with the *Receivers* that supply their data in the subbranch `Displays` of the `Slowcontrol` context. Each of them can use all of the `ROOT` provided methods to graphically display different parts of the observation data, which are fetched from the particular *Receivers* using the pull mode.

The configuration of the different *Displayers* is done via the central database and contains, among other things, the desired mode of graphical display. Possibilities are scatter plots, value-over-time graphs, bar charts, one and two dimensional histograms and more. Through a patch developed by the H.E.S.S. cooperation, all of the `ROOT` graphics displayed can by resized and moved dynamically while their content changes, which provides additional flexibility for the shift crew. A snapshot of the graphical output of several commonly used *Displayers* is shown in Figure 4.4.

4.3.5 Online Analysis

For immediate feedback on observation results, the HESSDAQ also incorporates a method of on-the-fly calibration and analysis of raw data. This so-called online analysis is performed by a single *Analyser* process in each of the `Node` Contexts. They are registered as `Node01/Analysis`, `Node02/Analysis`, etc. and get their particular data from the accompanying *CameraReader* processes.

To calculate the desired results in real-time, the *Analysers* makes use of an accurate and fast one-pass algorithm to calculate the pixel pedestals while setting the flatfield and ADC-to-p.e. coefficients to estimated nominal values.

The *Analysers* periodically send their results to a special process called *AnalysisServer*, which will generate an excess skymap via a simple background estimation approach. This skymap is displayed on-site on a control room monitor, alongside with selected calibrated camera images and a plot showing the number of excess events over the squared angular distance from the pointing position.

Additionally, the excess skymap is permanently scanned for regions with high significance and notifications are displayed to the shift crew in case of a valid signal. Originally, this scanning was only done for the position where the source was assumed. Recently, however, this system has been extended to be able to scan the whole field of view.

The online analysis is especially useful for the quick validation of the presence of variable

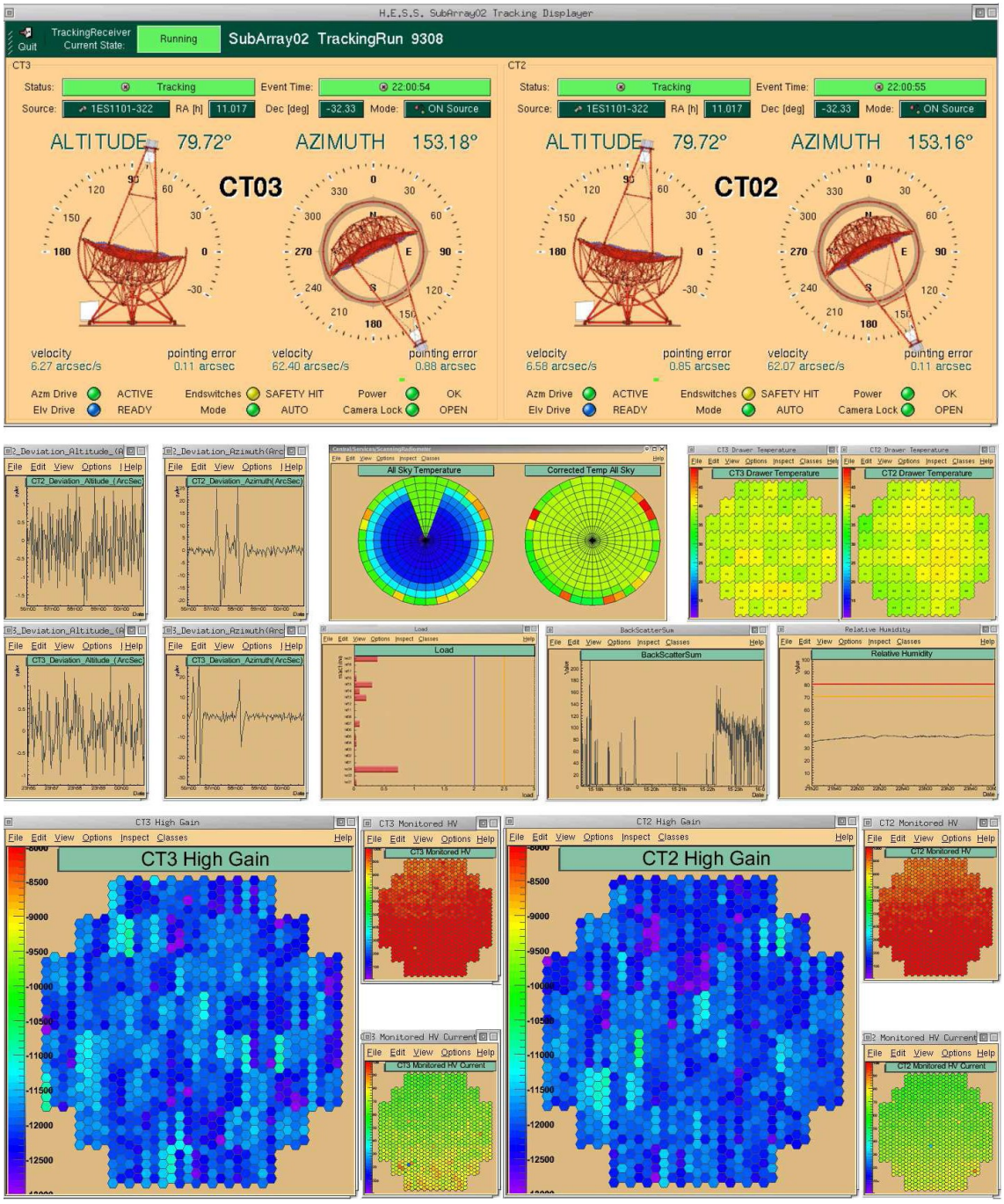

Fig. 4.4: *Snapshot showing some of the* Displayers *used during H.E.S.S. data-taking. The upper part shows two of the tracking windows, which display the telescopes' current pointing direction. In the central part, among others, the* Radiometer *output can be seen alongside with the drawer temperatures of two camera drawers. The lower part contains two displays showing camera images alongside to HV monitoring diagrams.*

sources such as blazars, flaring AGNs[15] or GRBs. As a consequence, the alert system described in this can be extended to dynamically react to the results of a particular alert observation by e.g. scheduling further observations to the alert target or tracking to the refined position in case of a positive finding.

4.3.6 GCN Notice Handling

As mentioned in Section 1.3, the HESSDAQ is already capable of a manual reaction to GRB alerts from NASA's Gamma-Ray Bursts Coordination Network. This is implemented through a HESSDAQ program called *GCN-Alerter*, which watches out for Internet distributed GCN Notices on a certain IP[16] address and port, which is registered at the GCN.

When a GRB is detected, the GCN sends a "GCN Notice" to all registered addresses, including the host of the HESSDAQ *GCN-Alerter*. This process then checks the information contained in the received packet against several filter criteria defined by the H.E.S.S. GRB observation policy described in Section 5.1. In case observation of the GRB is possible under satisfying conditions, the *GCN-Alerter* will react with a sound warning and a pop-up window for the shift crew. This happens for alerts that have been approved for both "prompt observation" and "afterglow observation" (see Section 5.1).

4.4 Standard Data Taking

As already mentioned in the last Chapter, data acquisition is not done continiously with H.E.S.S., but divided into runs of usually 28 min duration. The procedure how these runs are scheduled by the shift crew, and how they are processed by the parts of the HESSDAQ described in the previous Sections will be introduced in this Section. Furthermore, the data acquisition software's graphical user interface used by the shift crew to control the experiment will be explained.

4.4.1 Graphical User Interface

The H.E.S.S. central graphical user interface for data acquisition (hereafter DAQGUI), contained in the `daqgui` module of the HESSDAQ, is implemented in the program `HESS-Array.py`. As a `GTK`[17] based graphical utility written in `Python`, it acts as the central software interface that allows the on-site shift crew to control and monitor all HESSDAQ processes. Furthermore the DAQGUI is used to power up the HESSDAQ and it performs the scheduling and starting of new observation and calibration runs. A snapshot of the DAQGUI during data-taking can be seen in Figure 4.5.

For the starting and stopping of the HESSDAQ, the DAQGUI executes an external `Python` program called *Watchdog* that has been especially written for this tasks. For powering up the HESSDAQ, the *Watchdog* first checks if the system is not running already and, if necessary, starts the *ResourceHandler* and on each participating cluster computer one *HostHandler*. The further start-up of the remaining processes is then handled by the *ResourceHandler* and the *HostHandlers* as previously described in Section 4.3.1. When the HESSDAQ is shut down, the *Watchdog* first terminates the *ResourceHandler* and the *HostHandlers* and then all other participating processes on every cluster PC. The

[15] active galactic nuclei

[16] The main communication protocol of the Internet, the Transmission Control Protocol/Internet Protocol (TCP/IP), uses four digit *IP addresses* to identify every participant. To allow for multiple communication channels, every IP owner can send and receive data through 65355 different *ports*.

[17] more information at `http://www.gtk.org`

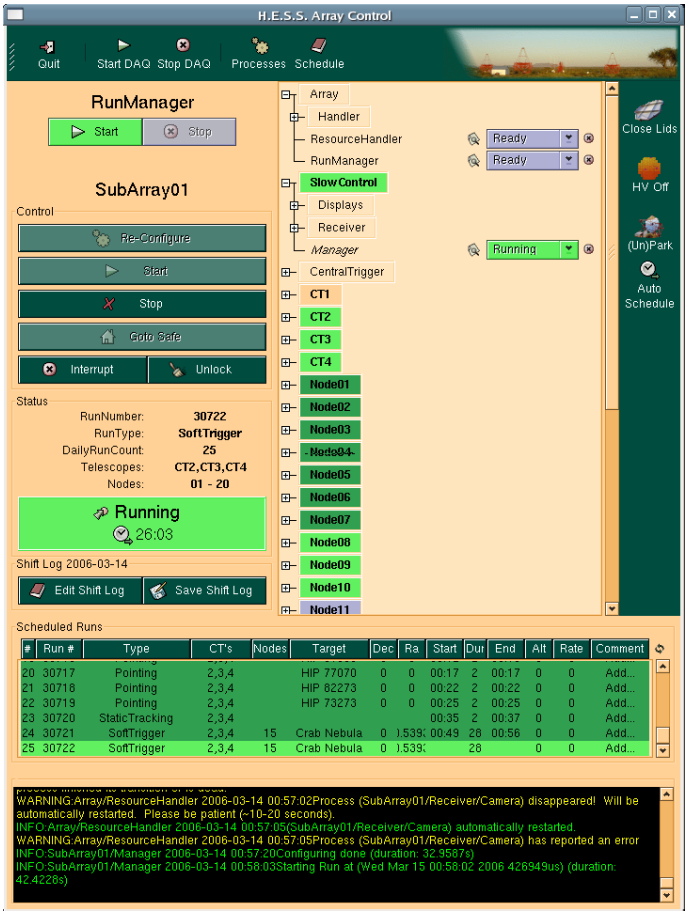

Fig. 4.5: *Snapshot of the graphical user interface used to control the H.E.S.S. data acquisition*

Watchdog usually runs unnoticed by the shifters, as all of its functions can be invoked through the DAQGUI.

Upon a complete restart of the system, the initial state of the processes is usually SAFE, although there are a few exceptions. One example is the *CentralTrigger*, which is configured and started immediately, and thus initially in the state RUNNING. Another exception is the *ResourceHandler*, which undergoes the CONFIGURE transition at start-up, during which it reads the whole Context tree from the database as well as the current cluster configuration, i.e. which computer to start what process on. The latter is needed so that the particular *HostHandlers* can be informed about what processes they should start and monitor. Finally all processes in the Context `SlowControl`, which are most of the *Receivers* and the *Displayers*, are immediately brought to the RUNNING state upon start-up.

When the HESSDAQ is running, the DAQGUI displays the Contexts and the processes therein, each with its current state both printed beside it and indicated by a special coloring (see Figure 4.1). Although this is not necessary during normal operation of the system, allowed process transitions can be manually invoked for each process. Thus the DAQGUI provides a full manual control of the soft- and hardware, meaning that the shift crew can, for example, close the camera lid, reconfigure a *Displayer* because of a changed database entry or stop the flatfield *Controller* if necessary.

For each night with available moonless darkness (also called darktime), a schedule of

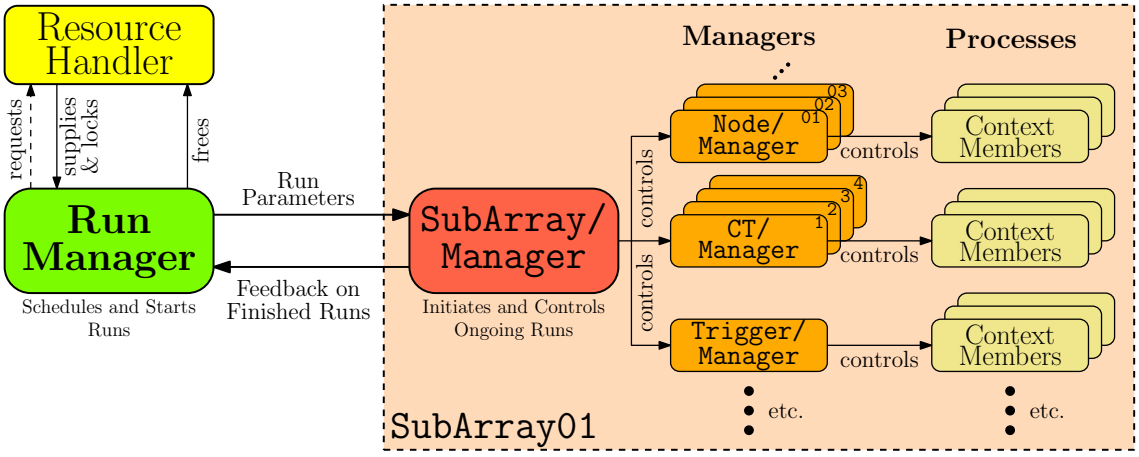

Fig. 4.6: *Sketch of the interactions between the* RunManager*, the* ResourceHandler*, the* SubArrayManger *and all processes controlled by the latter.*

observation runs that should be commenced therein has to be entered by the shift crew on-site. Although the DAQGUI provides the possibility to do this manually with a built-in subprogram, this task is normally accomplished by starting a so-called *AutoScheduler* process, which reads the previously decided observation timetable from database and schedules the runs for the coming night

To initiate the processing of the observation plan, the shift crew finally starts the *RunManager*, via a simple button click on the DAQGUI. From that point, everything that follows is automated and needs no human interaction.

4.4.2 Run, Resource and Array Management

When the *RunManager* is started via the respective DAQGUI button, it first undergoes its CONFIGURE transition. Therein it reads the complete schedule of runs that have been planned for the current observation day[18] and a list of runs already commenced from the central database. It then compares these data to generate a list of still unprocessed runs and initiates its START transition. Once it is in the RUNNING state, the *RunManager* takes the first valid run from this list and performs a number of actions necessary for the observation to start. This will be described in the following and is schematically shown in Figure 4.6.

First the *RunManager* needs to make sure that all hardware components necessary to perform the new run are available and not busy. For this, it requests the list of desired resources, e.g. `CT` Contexts (i.e. telescope hardware) and `Node` Contexts (i.e. *CameraReaders*) at the *ResourceHandler*, which at every times knows which hardware parts are in use. If even one resource is unavailable, the run is marked as pending, which means that it is entering a queue, where it waits until a run using the same resources has finished. This described resource check is done every second in an independent subroutine, even if a run is in progress, which ensures that two adjacent runs with totally different required hardware can be processed at the same time (for example two distinct observations with only two telescopes each).

If the resources are free, the *ResourceHandler* locks them, i.e. marks them as busy, and

[18] For the H.E.S.S. DAQ software, an observation day per definition lasts from 12 a.m. of the current until 12 a.m. of the follwing day. This avoids software and database difficulties caused by switching dates at midnight

allows to use them for the upcoming run. Further actions are now delegated to another process, the *SubArrayManager*, which is a specialized *Manager* residing in a `SubArray` Context and responsible for initiating all state transitions necessary for the starting of the run. Although this is a rare scenario, the simultaneous observation of more than one target is possible using more than one instance of this process, each responsible for one or more telescopes, assigned computing nodes and other resources. That is why a subarray is also a resource needed by every process and requested by the *RunManager*, although there is commonly only one Context of that kind named `SubArray01`.

Before a new run is assigned to the *SubArrayManager*, the *RunManager* sends it the so-called run parameters, i.e. a list of required resources and basic information about the run. This is done via the `TakeRunParameters` interface, which is inherited by every Manager. The *SubArrayManager* now distributes this information by calling the `TakeRunParameters` interface of all its affiliated *Managers*, which in turn call this interface on all their affiliated processes.

When this is done, the *RunManager* invokes the CONFIGURE transition of the *SubArrayManager*. Subsequently, the *SubArrayManager* does a database lookup and reads the parameters of the active run, such as its duration, its type (e.g. FlatFielding, SinglePE, Observation, etc.), the observation target, the wobble offset and many additional hardware settings. Thereafter, by invoking the CONFIGURE transition of its *Managers*, it distributes this parameters among all involved Contexts, because the *Managers* themselves send the parameters to their affiliated processes when configured. As already mentioned, the *Managers* are responsible for fulfilling the inter-process dependencies during every state transition.

After all *Managers*, and therefore also all their assigned processes, reached the READY state, the *SubArrayManager* notifies the shift crew and the *RunManager*, which in turn removes the currently processed run from its internal lists. When this has been done, the *SubArrayManager* starts itself, and in the process it stores information about the processed run in the central database. Among other things this means that it creates a new entry in a table listing all runs ever started, which will increase a counter in this table and therefore provide the so-called "run number". This information is not only used by other HESSDAQ processes when reading database entries about a particular run, but it is also important for the later association of analysis data with targets and observational parameters.

Next, the *SubArrayManager* informs its *Managers*, which again inform their active processes, about the acquired run number. Subsequently it starts several parallel running subroutines, each of which will invoke the START transition of one participating *Manager*, which will use the same technique to start all processes it is responsible for.

When the last process arrives at the RUNNING state, the start-up of the system is finished and the observation in progess. The *SubArrayManager* now informs the shift crew that the run has successfully started and begins with the countdown of its duration. The remaining time is displayed in the DAQGUI and when it reaches zero, all participating processes undergo the STOP transition, which is invoked in the same way as the START transition described above.

When all participating processes have reached the READY transition the *SubArrayManager* informs the shift crew and the *RunManager* that the run has stopped and again writes tables to the central database, which will later help to find out which of the started runs has been finished successfully. As a last step, the *RunManager* marks the finished run as "produced" and tells the *ResourceHandler* to free the according locked hardware components.

5 Integration of the GRB Alert Mode

The original H.E.S.S. data acquisition software described in the last Chapter had to be modified in several of its modules in order to integrate the new gamma-ray burst alert response system (GRBARS). These changes will be discussed in detail in this Chapter. Furthermore, the current H.E.S.S. GRB observation policy will be outlined and the preceding requirements posed to the GRBARS to ensure its efficient and safe operation will be addressed.

5.1 GRB Observation Policy

The currently pursued H.E.S.S. observation policy for GRBs states that only Swift GCN alerts will be considered for observation[1]. It also specifies the shift crew reactions to this external alerts. These are dependent on the information contained in the packages coming from the GCN and received and interpreted by the *GCN-Alerter*. At the moment the incoming GRBs are classified into three categories, which allow for different shift crew reactions:

Prompt Observation : The shift crew is authorized to immediately take all actions necessary to observe the onsetting GRB as soon as possible. This requires that its zenith angle is smaller than 45°, the time of the alert is at maximum one hour before H.E.S.S. darktime and at least 30 minutes of observation must be possible. When all actions have been taken the H.E.S.S. GRB expert on charge must be informed, which may halt the observation or schedule additional runs as seen fit.

Afterglow Observation : The GRB falls in this category if the prompt observation criteria are partly not met, but the GRB is still observable in the upcoming or ongoing darktime. If a GCN Notice categorized into this class arrives outside darktime, the GRB expert in accordance with the H.E.S.S. OC[2] has to decide whether to schedule appropriate runs at the beginning of the upcoming observation period. If already available, the red shift z is a factor in this decision. Observation is then by default commenced up to 24 h after the trigger when $z < 0.1$, up to 12 h after the trigger when $z < 0.3$ and up to 6 h after the trigger when $z < 1$.

No Observation : Under certain conditions, GCN Notices are discarded upon arrival and no actions are taken, namely when the GRB is out of view with a declination greater than 17° or smaller than -62°. Besides that, GRBs with a positional error of larger than 2.5° or with a known redshift of $z > 1$ are not observed. Lastly, events marked as coming from a known non-GRB ground or flight source are also discarded.

The GRBARS described in this work also adheres to this policy and only acts in the case of a GCN Notice suitable for "prompt observation".

[1] This may change in the near future to also enclose the Fermi satellite.
[2] Observation Committee

5.2 Requirements

The requirements to the GRBARS that have been considered in its implementation on the one hand arise from the short-lived nature of GRBs, but are also due to safety requirements of the various hardware components. Additionally, several software design constraints have to be met.

5.2.1 Minimum Speed

Considering the average duration of the long GRBs[3] of around 30 s, the alert reaction time, measured from the stopping of the ongoing observation until the first recorded event from the new pointing position, should not greatly exceed this time span, as it would be otherwise relatively unlikely to observe the most interesting prompt phase of GRBs.

Assuming all hardware components of the H.E.S.S. array could be operated without delays, the time needed to slew the telescope to the target position still remains as a minimal reaction time. Taking into account the total annual H.E.S.S. observation time under good conditions and assuming a spatially and temporally isotropic distribution of gamma-ray bursts, it is possible to calculate an average annual number of GRBs R_{obs} occurring within a certain angular distance θ to the actual telescope pointing direction. As the H.E.S.S. alert response system currently only reacts to events from the Swift Satellite, the annual overall rate of GRBs R_{total} used in the calculation has been set to Swift's mean burst detection rate of 93.75 GRBs per year. The formula used to generate the respective graphs, shown in Figure 5.1, is:

$$R_{\mathrm{obs}}(\theta) = \frac{2\pi\,(1-\cos\theta)}{4\pi} \cdot R_{\mathrm{total}} \cdot f_{\mathrm{cond}} \tag{5.1}$$

Here, the first quotient is the fraction of a full sphere that is covered by a cone with opening half-angle θ and f_{cond} is the fraction of a year, in which H.E.S.S. can observe under chosen conditions. For Figure 5.1, the total observation hours used to calculate the fraction f_{cond} were 1 year, 1835 hours (total H.E.S.S. observation time in 2006) and 1086 hours (observation time under good weather and technical conditions in 2006).

As the maximum tracking speed of the telescopes, which due to rapid acceleration is reached in the order of a few seconds, is well known ($\approx 100^\circ$ per minute), the angular distances θ can easily be translated to tracking durations. The graphs show that within an angular distance of 30°, which corresponds to a pure tracking duration of about 20 s, an average of 0.78 GRBs per year could be observed by H.E.S.S. during good overall conditions.

Naturally, the telescope slewing alone is not the only time consuming operation between two runs. Even if the alert observation is already scheduled at the time the old run is interrupted, the HESSDAQ needs some time to reconfigure all required hardware components. The most time consuming operation is the fact, that the high voltage supply of the PMTs must be shut down before moving the telescopes and slowly powered up again after the target has been reached. Furthermore, the cameras and the tracking hardware usually undergo an extensive reconfiguration when a new run is started, which is done over a relatively slow serial interface and needs some time. Finally, the `CT/Tracking` *Controllers* normally do a fine-positioning at the end of the telescope movement, which is needed for final pointing accuracy improvements to the order of arc seconds.

[3] Short GRBs will not be considered here, as their duration in the millisecond regime makes observation of their prompt phases with IACTs practically impossible.

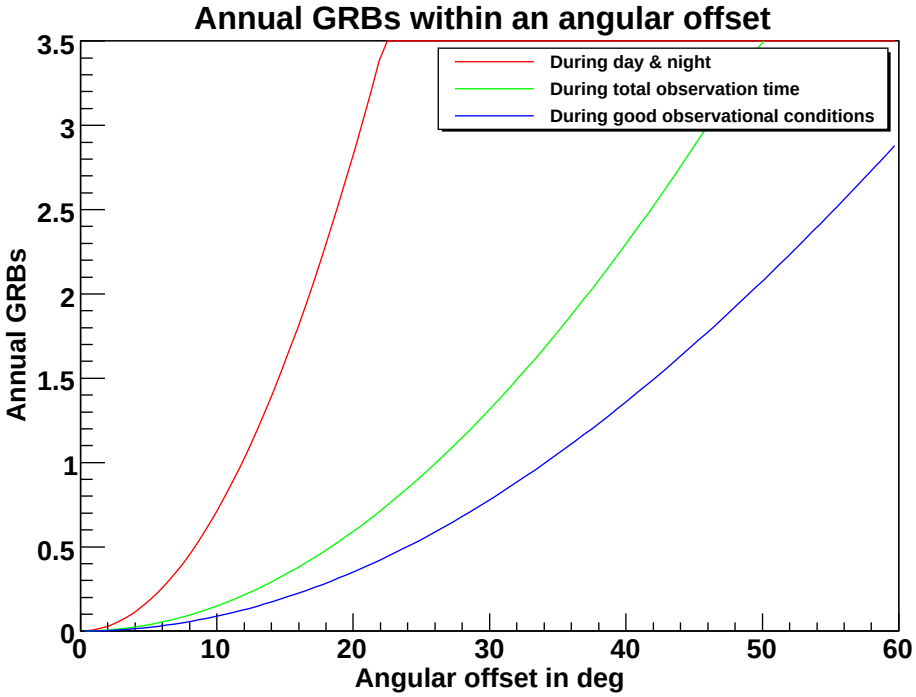

Fig. 5.1: *The average annual number of Swift detected GRBs occurring inside a certain angular offset to the actual observation position. The three graphs calculated for different observational conditions listed in the label, with f_{cond} set to 1, 1835 h/a and 1086 h/a in this order. The values for total and good H.E.S.S. annual observation time have been taken from the observation statistics of 2006.*

As already mentioned in the introduction, the manual procedure for a GRB alert observation applied by H.E.S.S. so far, which involves the stopping of the ongoing run, and subsequent starting of a newly schedules GRB observation run, needs around 150 s on the HESSDAQ side alone, depending on the angular distance of the GRB. Although the GRBARS will, with the elimination of the human decision time, already remove the largest delaying factor, a central requirement to its design has been to reduce the HESSDAQ's response time to an external alert to a value as low as possible.

5.2.2 Software Consistency

Another important requirement to the GRBARS was the seamless integration into the existing modular concept of the data acquisition software, without having to extensively modify essential parts of the system or change the initial idea behind one or more programs. This ensured the overall consistency and stable operation of the HESSDAQ. Moreover, it helped to minimize the diversions from the original concept, which allows a quick comprehension of the modifications by all responsible software experts.

5.2.3 Safe Operation

As a final prerequisite, the necessary modifications still have to allow the safe operation of all hardware parts of the telescope system and thus it had to be assured, that the existing possibilities for an emergency stop of the system still works after integration of the GRBARS. As an example, the initial idea of a permanent supply of the camera PMTs with high voltage to avoid the time delay origination from the slow reactivation

was discarded because the risk of damaging the PMTs when exposing them to the bright star light of the Galactic plane or other star concentrations during slewing to the target was too high.

5.3 Integration in the Software

The basic concept of how to integrate the GRBARS in the existing software while adhering to all requirements described above was to implement the possibility for a fast "alert stop" of an ongoing run, followed by an "alert start" of the meanwhile automatically scheduled GRB run. During this procedure only software actions that are unavoidable for either stability or functionality reasons are to be carried out. This provides a significant speedup over the conventional run stop and start method. This is because normally all involved processes are completely halted and reconfigured even when it is not necessary for the special case of GRB alert observation runs, where speed has the highest priority. For the implementation of this approach software modifications have been necessary, which will be described in the following.

5.3.1 Software Framework Modifications

This Section will describe the changes applied to the already existing framework of the HESSDAQ, comprising the process state management, the handling of GCN Notices, the Context and dependency management and finally the run and array management.

Process State Management

In the existing HESSDAQ framework, processes directly involved with telescope runs get sent to the Ready state via the Stop transition when a run is finished. For the starting of the next run, they undergo the Start transition to reach the Running state. Because during this transitions a number of actions are taken, which can be omitted for speed optimization in the special case of a GRB alert observation, the unchanged Start and Stop transitions were unsuited for use in the GRBARS.

In order to minimize the software changes needed and to make use of the existing HESSDAQ framework, the already available Paused state and the according transitions Pause and Resume were redefined for the purpose of the fast alert stop and start transitions respectively. As most HESSDAQ programs did previously not perform any special actions during these two transitions, this could be done without extensive changes.

An exception were the *CameraReaders*, which originally used the Paused state to indicate that they are ready for new camera data. This functionality was therefore shifted to a new state called Idle and an according pair of transitions called GotoIdle and UnIdle, which have been integrated in the `StateController` class. Figure 5.2 shows a sketch of the software states and transitions possible after the modifications.

Another change to the `StateController` class was to integrate a new CORBA interface called `SignalAlertObservation`. This interface is inherited by virtually every HESSDAQ process and each of them may redefine the actions taken when it is called from an external process. Thus, if requested, every HESSDAQ process can now perform state independent actions in response to an incoming alert. This possibility is used in a number of process which will be described in the upcoming Sections.

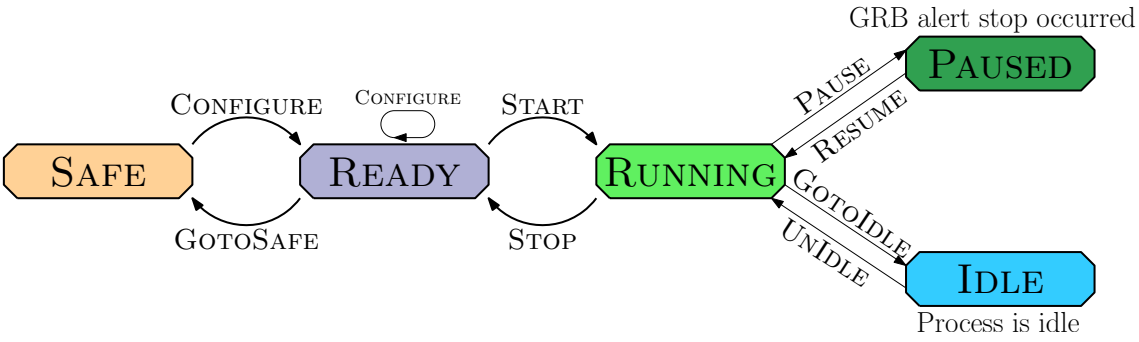

Fig. 5.2: *Process states and transitions after modifications for the GRB alert response system*

GCN Notice Handling

An import software change was also needed at the *GCN-Alerter* process. As mentioned in Section 4.3.6, its normal behavior is to display a warning window upon an incoming GCN Notice. Additionally it prints out a command, which the shift crew had to execute manually. This command uses another process (called *NewGRB*) to insert the GRB in the central database as a new top priority target for the ongoing shift period. When the *AutoScheduler* process is now manually executed by the shift crew, the GRB observation is scheduled with at least one run before anything else.

These two manual process calls had to be automated, which was done by implementing the execution directly in the *GCN-Alerter* at the same point where the shift crew warning message is printed out.

Context and Dependency Management

When a GRB alert is received by the *GCN-Alerter*, all processes involved in the ongoing run need to be informed through their `SignalAlertObservation` interface to trigger the necessary process specific actions. Because the processes of a Context are not visible from the outside, but only the respective Context *Manager*, the notification of all processes must be delegated to the latter. This is done by the *SubArrayManager*, whose list of active (i.e. affiliated) processes comprises all *Managers* of the Contexts involved in the run. When the *RunManager* requests the start of a new run marked as alert observation, it will call the `SignalAlertObservation` interface of all its *Managers*. In turn the *Managers* will inform their affiliated processes of the alert through the same interface. In this manner, the information about an upcoming alert observation gets distributed among all involved processes.

Furthermore, the *Managers* can now be instructed not to invoke certain state transitions on selected processes[4]. However, this possibility is not yet used with the current version of the GRBARS.

Another modification has been applied to the dependency scheme monitoring performed by the *Managers*. When Pausing and Resuming their processes, which only happens on an incoming alert, the normal dependency scheme is ignored. Instead, a special alert dependency scheme has been entered in the database[5], which will be used for this purpose. This has been done because during alert stopping and starting, several of the normal dependencies are not required any more. The process dependencies employed during alert

[4] At the moment this processes and transitions need to be hard-coded into the `ManagerBase.C` code.
[5] The new table is named `DAQ_AlertDependencies`.

transitions in this first version of the GRBARS are shown in Table 5.1, in which all processes are listed with their respective nameserver entries[6]. This table does not yet include all necessary dependencies for an operation of the GRBARS under real observation conditions and will be extended in the future.

Process	Depends On
`SubArray/Trigger/Connector`	`CT/CameraTrigger`
`CT/CameraTrigger`	`CT/CameraHV`

Table 5.1: *The modified dependency scheme employed for the alert transitions* PAUSE *and* RESUME

Run and Array Management

The most extensive software modifications were needed in the run and array management. In the unmodified software, the *RunManager* only reads its process schedule when it undergoes the CONFIGURE transition, which it does when started via the button on the DAQGUI. However, in case of a GRB alert, an updated run schedule is written through the *GCN-Alerter* and this schedule needs to be read by the *RunManager* as fast as possible to permit a swift reaction. Therefore, the *GCN-Alerter* also calls the `SignalAlertObservation` interface of the *RunManager*, which will then reconfigure itself and thus read the new schedule.

In general this will not lead to the interruption of the current run, unless the next run in the new schedule is marked as alert observation[7]. If that is the case, the *RunManager* will first check, if there is a currently processed run. If not, the alert observation run (AOR) will be marked as a normal run and its start-up will be continued as usual. If there is an ongoing run, the normal resource check is omitted, because the needed hardware is known to be in use. Instead, it is checked whether the ongoing run has enough assigned resources (e.g. at least two telescopes, and four *CameraReaders*). Again, if this is not the case, the AOR will be turned to a normal run, which will be next in schedule.

Only if there is a current run with enough occupied resources, the *RunManager* takes the necessary actions for the alert interruption of the ongoing run. First it spreads the information of an ongoing AOR through the `SignalAlertObservation` interface of the *SubArrayManager* and then it sends the AOR's run parameters through the `TakeRunParameters` interface of the same. In the *SubArrayManager*, the latter interface has been adapted to remember the run parameters of the interrupted run, as they are needed later for the entries of some database tables. The new run parameters are now distributed among all involved processes, as already described in Section 4.4.2.

When the above preparations have been taken, the PAUSE transition of the *SubArrayManager* and thus of all invoked processes is invoked. As a result every involved process performs the actions necessary for a fast alert stop. Additionally the *SubArrayManager* marks the interrupted run as finished in the database.[8]

When PAUSED state is reached by all members of the subarray, the *RunManager* invokes the RESUME transition of the *SubArrayManager*, which will then perform the alert start

[6] compare with Table 4.1

[7] The marking is done by a newly added `RunMode` column in the respective database tables, which can be either `normal` or `alert`. This column will now additionally be read out by the *RunManager*.

[8] This is done by adding an entry to the `RunEnd` table.

of the AOR. To do so, it first writes some information about the AOR to the database[9]. This is also needed to acquire the run number as most important run parameter of the AOR[10], which is afterwards distributed among the involved processes[11].

Finally the *SubArrayManager* resets the run duration to 28 minutes and invokes the RESUME transition of all affiliated *Managers*, which do the same with their processes until the whole subarray is running again. Upon resuming, the involved processes perform the actions necessary for starting the AOR as fast as possible. When this has happened, the operation proceeds as normal.

5.3.2 Hardware Behavior on Alert Observations

The modifications of the HESSDAQ framework described in the previous Section provide the state transitions PAUSE and RESUME for every process involved in a data-taking run. While most processes do not perform any specific actions during these transitions, they had to be implemented for a number of hardware *Controllers* to achieve the necessary speedup. The particular modifications will be described in this Section.

Camera High Voltage

During an alert stop of an ongoing run, the camera high voltage needs to be reduced to a low enough value to allow for the safe slewing of the telescopes. Otherwise, the sensitive photomultiplier tubes inside each camera may be permanently damaged when they get exposed to the light of too many bright stars at once, especially when passing the Galactic plane during the tracking.

In this first version of the GRBARS, the PAUSE transition just imitates the STOP transition, which will reduce the voltage to 400 V. Because this way of reducing the HV to a safe value has not been optimized for speed, it still needs a few seconds. An almost immediate alert shutdown of the HV is, however, possible and will be implemented by H.E.S.S. camera experts in the near future.

When undergoing the RESUME transition, the HV is slowly raised again until reaching its nominal value. The slow raising of the voltage is unavoidable due to technical reasons.

Camera Trigger

The internal trigger system of the cameras must be halted and resumed during an alert stop, because the system would get confused if still receiving trigger events after the ongoing run has been alert interrupted.

To do this, the PAUSE and RESUME transitions of the `CT/CameraTrigger` processes copies the behavior of STOP and START. Regarding the speed requirement, this is can be done without concert as these transitions are processed relatively fast.

Camera Nodes

In normal operation, when undergoing the STOP and START transitions, the *CameraReaders* finish their format conversion for the current bunch of camera raw data, empty their buffers, close their actual data files and open new ones. Because especially the finishing of the data processing can take quite a lot of time, it has been implemented that the

[9] The tables `RunStart` and `ProducedRunParameters` are filled here.

[10] The entry to the RUNSTART table will contain an auto-incremented row number, which will be used as "run number" to identify the run in all further interactions.

[11] Performed again by using the `TakeRunParameters` interface of all participants.

CameraReaders will not perform any actions when they undergo the PAUSE and RESUME transition. A disadvantage of this method is that there will be no dedicated camera data files for the AOR, but instead this information is contained in the files for the interrupted run.

The speedup gained by this approach, however, makes up for this and the files that contain data for two runs can be easily be cut into two separate files by an appropriate process called periodically.

Tracking

The *Controllers* responsible for the telescope tracking have been modified to slew the telescopes to the new target already when undergoing the PAUSE transition. Because state transitions of processes that do not depend on each other are performed simultaneously, this has the advantage that other involved processes can undergo their sometimes time consuming PAUSE transition when the tracking is commenced, thus not losing this time later. For safety reasons, the tracking system has to wait until all involved HV *Controllers* have reached the PAUSED state.

When later undergoing the RESUME transition no actions are performed, as the telescopes are already on target.

6 Analysis of Simulated Alert Runs

The first version of the GRB alert mode was integrated in a development copy of the H.E.S.S. data acquisition system on-site in July 2008. To ensure the stability, performance and functionality of the modified system, several test runs were performed with different hardware parts of the telescope system. For every test, run a new run type beginning with `AlertTest` was defined in the central database[1]. The results obtained, especially regarding the reaction speed to the simulated alerts, will be presented in the following Chapter and summarized in Section 6.2. A discussion of possible, but still unimplemented, optimizations to the GRBARS will be given in the conclusion.

6.1 Simulation Runs

In following Section, the simulated alert runs performed to test the automatic response system to gamma-ray bursts and their results regarding the alert reaction time of the system will be presented.

6.1.1 Manually Triggered Camera

For testing the behavior of the camera related processes during an alert triggered PAUSE and RESUME of the system, a new run type called `AlertTestSoftTrigger` was defined in the database. During a run of this type, the telescopes stay in parking position and the camera lid is closed. A trigger signal for the cameras is generated at hardware level, which will cause the readout of the pixel amplitudes. Because the telescopes do not move and the high voltage remains switched off during these runs, they provided a good way of testing the reaction time and proper functionality of the camera subsystem alone during an alert run. This includes the *CameraReaders*, the central and camera internal trigger.

A stable operation of the data acquisition system was possible during several test runs of the above described kind. The durations of the PAUSE and RESUME transitions of various camera related processes and for the whole subarray are shown in Table 6.1 for several `AlertTestSoftTrigger` runs. In this Table, the *CameraReader* values for the particular runs represent an average over all involved instances of this process. Furthermore, the values in the "`CT` Contexts" and the "*CameraTriggers*" columns are averaged over all four telescopes. The former represents the respective total transition time of all processes in the `CT` Contexts[2], while the latter shows the times for the camera internal trigger systems alone. The column for the total subarray shows the PAUSE and RESUME durations for the `SubArrayManager`, which corresponds to the time all involved processes needed for the transitions. The second last line shows the PAUSE and RESUME transition duration averages over all runs and the last line gives the sum of these two values for every listed component. All values used for the calculation of the displayed durations, with the exception of the durations for the *CameraTrigger*, which could only be extracted from the log files within 1 s precision, were accurate within milliseconds.

[1] in the table `DAQ_RunTypes`
[2] see Table 4.1

Run No.	CT Contexts		*CameraTriggers*		*CameraReaders*		Total Subarray	
	Pause in s	Resume in s	Pause in s	Resume in s	Pause in s	Resume in s	Pause in s	Resume in s
47100	4.29	6.04	1.25	5.00	0.00	0.00	6.41	9.88
47103	4.05	5.79	1.00	4.75	0.00	0.00	5.42	9.89
47107	4.30	6.04	1.25	5.00	0.00	0.00	6.44	10.90
47109	4.29	6.04	1.50	5.00	0.00	0.00	6.43	9.91
47111	4.04	6.30	1.00	5.25	0.00	0.00	5.42	10.87
47113	4.30	6.29	1.25	5.25	0.00	0.00	6.42	10.88
	4.21	6.08	1.2	5.0	0.00	0.00	6.10	10.39
	10.29		**6.2**		**0.00**		**16.49**	

Table 6.1: *Durations of the* Pause *and* Resume *transistions from several* `AlertTestSoftTrigger` *runs and various software components. The second last line shows the averages for the particular columns and the last line gives the average total reaction time for every component.*

The values in the table show that, after a GRB alert has been received, the GRBARS needs on average average 10.3 s to prepare the cameras for the changed observation conditions. Here, the Resume transition makes up the larger part, because while it is performed the cameras are reconfigured for the new run through a relatively slow serial connection. With a mean duration of 6.2 s, the pausing and resuming of the *CameraTrigger* accounts for most of the total duration. No contribution was made by the *CameraReaders*, which performed the transitions instantly because no actions are performed in them, as described in Section 5.3.2

The time all processes need for the alert transistions is equivalent to the Pause and Resume durations of the `SubArrayManager` and amounted to 6.1 s and 10.4 s respectively. Thus, the total alert reaction time of the manually triggered cameras with deactivated high voltage supply sums up to 16.5 s.

6.1.2 Tracking Only

For testing the stability of the telescope tracking during a simulated GRB alert, the `AlertTestTracking` run type was added to the database. In runs of this kind, the camera lid stays closed and all camera subsystems are switched off. Therefore, only the slewing of the telescopes is performed, which was used to test the speed and functionality of the tracking during an alert observation run.

To provide better statistics for the analysis presented in this Section, a number of normal `Tracking` runs[3] were also included. This does not invalidate the obtained results, because during the Pause and Resume transitions of the tracking *Controllers* the behavior of their Configure and Start transitions is essentially copied.

From the data of the performed test runs, the speed of the telescope tracking process could be extracted. The tracking duration over the angular distance for all test runs and some observation runs taken from July 24th until July 29th 2008 is shown in Figure 6.1 for all four telescopes. The tracking duration here refers to the duration of the particular Configure (for normal runs) or Pause (for alert runs) transitions, not to the pure slewing time of the telescopes.

[3] Conventional run type used to test the telescope tracking system, which has nearly the same parameters as the newly defined `AlertTestTracking` runs.

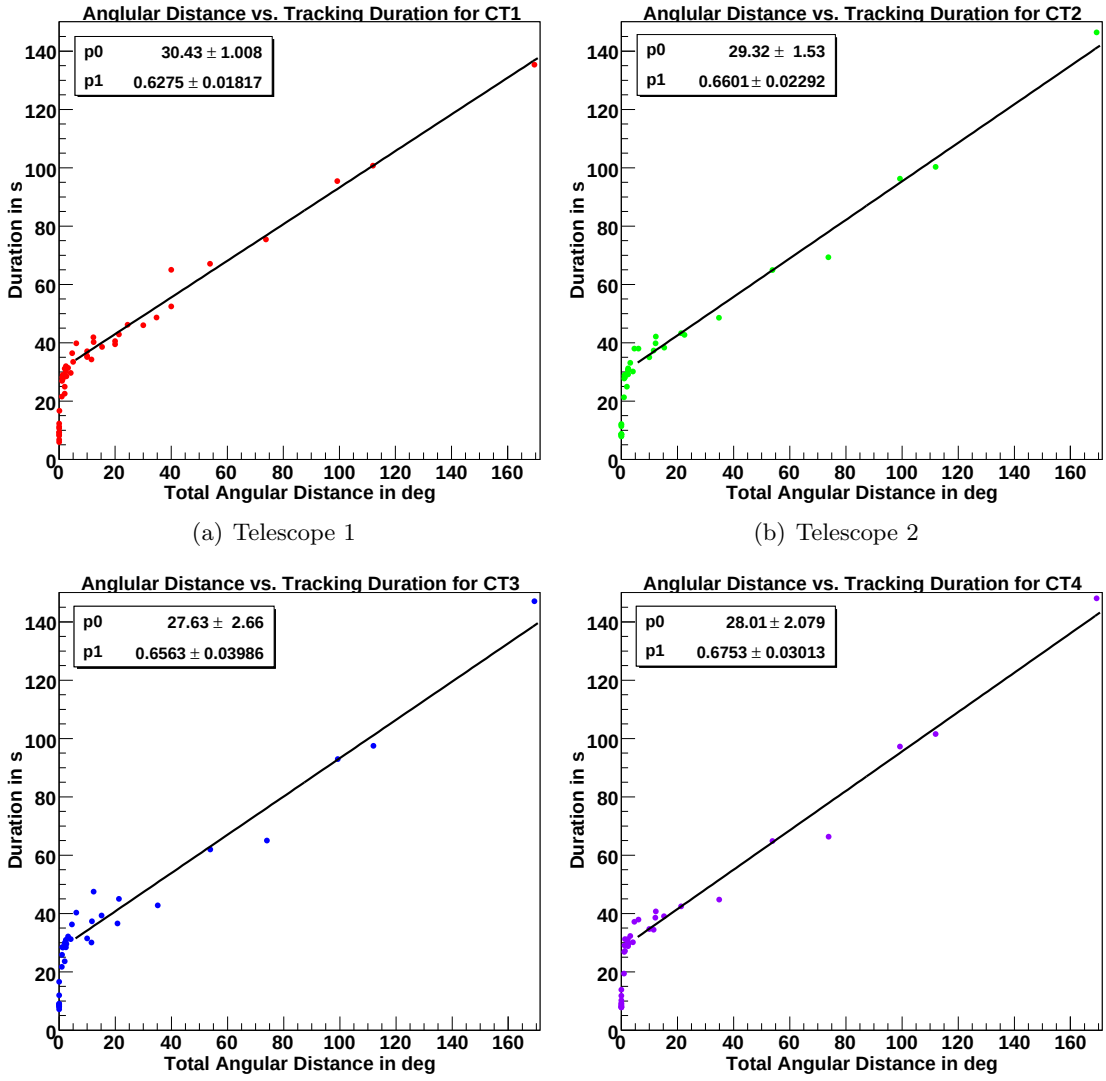

(a) Telescope 1

(b) Telescope 2

(c) Telescope 3

(d) Telescope 4

Fig. 6.1: *Tracking duration, i.e. the time of the* CONFIGURE *transition, for normal runs and the* PAUSE *transition for alert runs, over the total angular distance for runs between July 24th and July 29th 2008. The graphs additionally show a linear fit of the data beginning from 5°, where p0 and p1 are the intersection with the ordinate and the slope.*

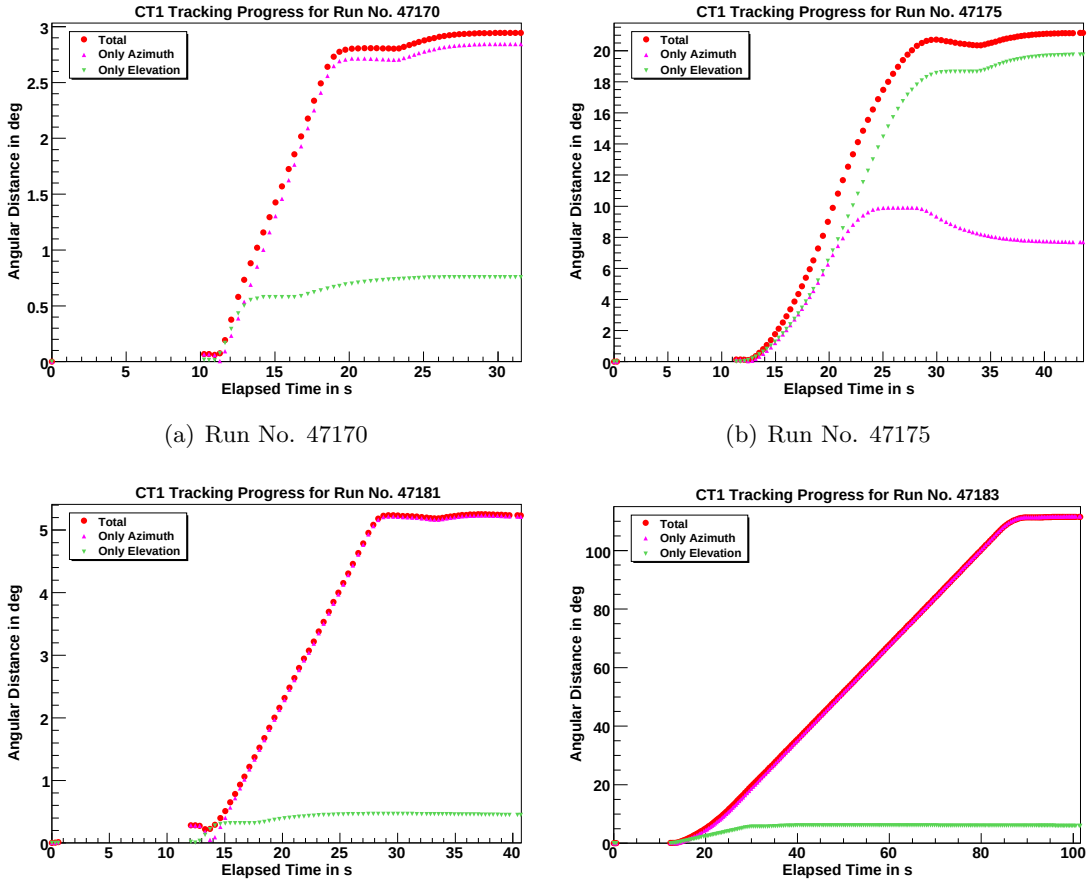

(a) Run No. 47170

(b) Run No. 47175

(c) Run No. 47181

(d) Run No. 47183

Fig. 6.2: *Tracking progress over time for several exemplary tracking test runs. The green triangles show the azimuthal, the violet triangles the attitudinal and the red discs the overall angular tracking progress.*

Because the telescope usually accelerate to their maximum speed of 100°/min in under 2 s, the graphs in Figure 6.1 should show a simple linear $v \cdot t$ dependence, assuming the angular distance is overcome without detours. Because the graphs display a linear function shifted in the positive y-direction, a time overhead, in which no slewing is done, can be concluded. The linear fits applied to the graphs for all telescopes, leaving out the values below 5°, show an average slope of 0.65 ± 0.3 s/deg. Taking into account the time needed for acceleration and deceleration, this is in good agreement with the actual maximal tracking speed of the H.E.S.S. telescopes of 0.60 s/deg. Thus the average y-intersection of the fits provides an estimate of the total non-slewing time, which amounts to an average of 28.8 ± 2.6 s. An exceptions to this were the runs, in which the telescopes were directly on target (0.0° distance) before the tracking started. Here, the total tracking transition time was considerably lower, with minimal values of around 6 s.

To demonstrate for which parts of the tracking-related state transitions the delays occur, the tracking progress over time has been extracted from data and plotted for several test runs. From the examples in Figure 6.2 it is apparent that a relatively constant delay of around 12 s precedes each slewing process. During that time, the telescope tracking hardware is configured.

The remaining overhead lies at the end of the CONFIGURE (or PAUSE) transitions. As it

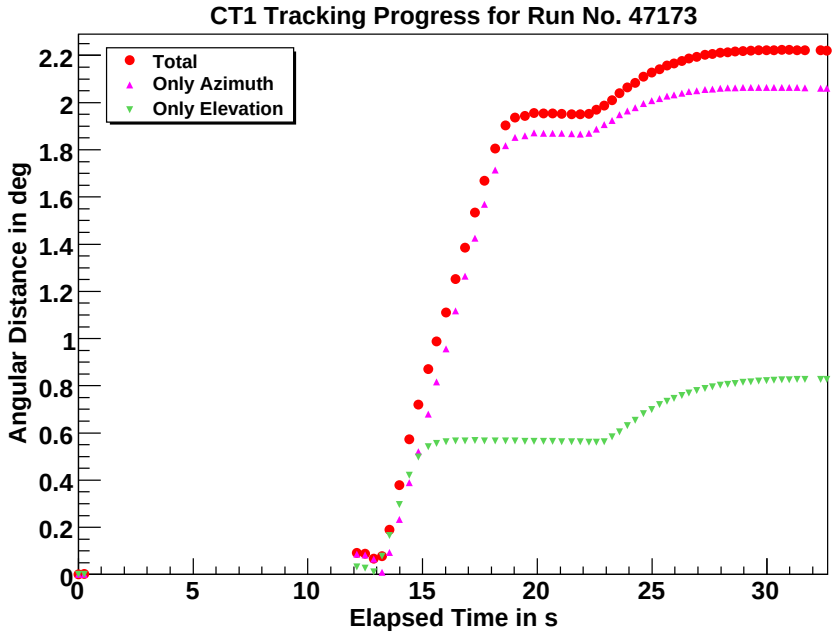

(a) Run No. 47173, Telescope 1

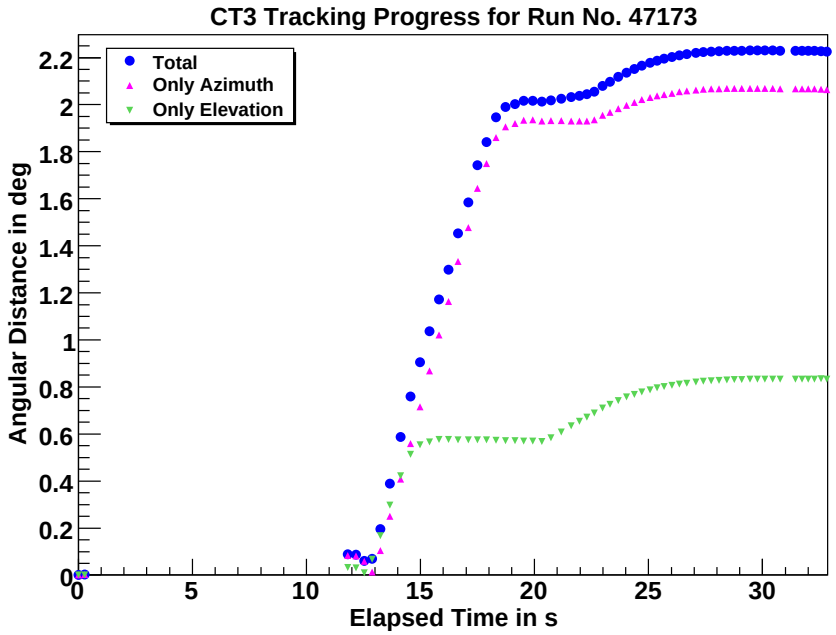

(b) Run No. 47173, Telescope 3

Fig. 6.3: *Comparison of the tracking progress of different telescopes. Shown is the tracking progress of run no. 47173 for CT1 and CT3.*

Run No.	Dist.	CT Contexts			*Tracking*		*CameraTriggers*		
		Pause	Resume	Total	Pause	Resume	Pause	Resume	Total
	in °	in s	in s	in s	in s	in s	in s	in s	in s
47050	3.06	32.16	5.28	37.44	31.68	0.00	1.00	5.25	6.25
47147	0.00	9.37	6.04	15.41	8.62	0.00	1.25	5.00	6.25
47149	1.00	20.87	5.79	26.66	20.18	0.00	1.25	4.75	6.00
47160	2.00	24.13	6.05	30.17	23.86	0.00	1.50	5.00	6.50

Run No.	Total Subarray		
	Pause	Resume	Total
	in s	in s	in s
47050	34.51	9.85	44.36
47147	11.46	9.86	21.32
47149	23.47	10.93	34.40
47160	26.47	9.58	36.05

Table 6.2: Pause *and* Resume *transistion durations of various software components for all performed* `AlertTestSoftTriggerTracking` *runs*

can be seen in the graphs, this delay, in which the telescopes are slewed only little, makes up an additional time of around 14 s. Together with the initial configuration delay this accounts for the total of 29 s overhead indicated by the graphs in Figure 6.1. A considerable part of this final overhead is caused by the fine-positioning procedure, which is done at the end of every telescope slewing to further increase the accuracy of the pointing. Other factors are deceleration and internal details of the tracking algorithms.

The progress graphs are all from data of the first telescope, because the tracking of the whole array is done nearly parallel, as the comparison between CT1 and CT3 in Figure 6.3 demonstrates. Though the tracking durations proofed to be larger than initially presumed, the tracking system operated stable with the GRBARS modifications.

6.1.3 Manually Triggered Camera and Tracking

The next step was to combine the manually triggered camera and the telescope tracking in a single test run type, which has been added to the database under the name `AlertTest-SoftTriggerTracking`. During runs of this type, the tracking is performed as usual and the cameras work as defined in the `AlertTestSoftTrigger` runs.

These runs were conducted to check the proper interaction of the two independent subsystems, i.e. the telescope tracking and the camera trigger and readout, during an alert observation run. Table 6.2 shows the Pause and Resume transition durations for various HESSDAQ components in the commenced `AlertTestSoftTriggerTracking` runs. The table columns for the whole `CT` Contexts and the *CameraTriggers* are averaged in the same way as in Table 6.1. The total angular distance of the tracking is shown additionally and the values for the *CameraReaders* are omitted here, as they amounted to 0.00 s without exception. Averages on all runs are not given in this table, as most transition times of this run type are now dependent on the angular tracking distance, which is also listed for every run.

The values for run no. 47047 again show, that only runs for which the target was already on the pointing position have a lower tracking overhead than even runs with an angular tracking distance of only 1°, which is an effect the algorithms controlling the tracking system. Since the telescope tracking does not influence the *CameraTrigger*,

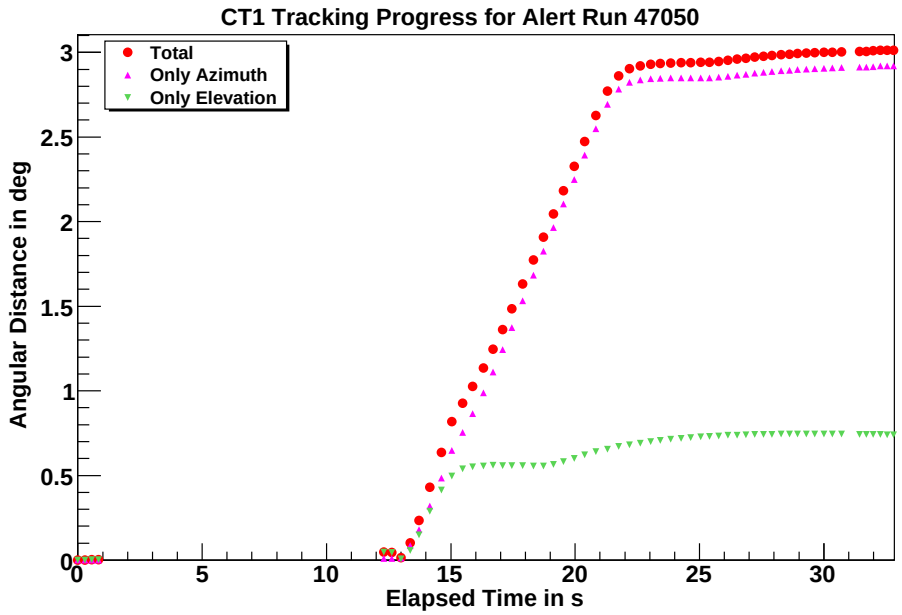

Fig. 6.4: *Tracking progress over time for the* `AlertTestSoftTriggerTracking` *run no. 47050 with an angular distance of 3.06°*

its PAUSE and RESUME durations are, within the given accuracy, the same as for the `AlertTestSoftTrigger` runs.

The total reaction time of the GRBARS for this run type, which corresponds to the total transition time of the *SubArrayManager* shown in the "Total SubArray" column, was under 45 s for all tested runs. Although this was partly the case because of the small angular distances, the situation would not change much for more distant targets, as the largest part of the tracking time overhead is already included (excluding run no. 47047). This is supported by the plot in Figure 6.4, which shows the tracking progress of `AlertTestSoftTriggerTracking` run no. 47050.

Taking into account the tracking speed from Figure 6.1 of 0.65 s/deg , it can be extrapolated that these kind of alert runs have a reaction time of under one minute for target distances of up to 35°.

6.1.4 High Voltage and Camera

As a last step, the camera high voltage supply needed to be tested to ensure proper functionality of the GRBARS when used during a real alert run. Because observation time was unavailable during the time of the tests, the camera had to be tested with closed lid in order to avoid damage to the PMTs. To do this, an alert run type called `AlertTestSinglePE` was defined. The non-alert version of this run is normally used for the calibration of the camera PMTs, as described in Section 3.4.1, and is done without moving the telescopes out of their parking position. Here, the equally parametrized alert version was used to test the behavior of both the high voltage and the trigger system of the cameras.

Another reason for these tests was to gain information about the time the camera HV needs for its PAUSE and RESUME transitions during an alert. During the former, the HV is reduced to its low state of 400 V and during the latter raised again to its nominal value. Because the telescope tracking has to wait for the reduction of the HV and the alert run

can only start, when the HV has been powered up again, the respective durations are crucial for the overall reaction speed of the system.

Run No.	CT Contexts		*CameraTriggers*		*CameraHVs*		Total Subarray	
	Pause in s	Resume in s	Pause in s	Resume in s	Pause in s	Resume in s	Pause in s	Resume in s
47089	18.10	36.23	2.00	4.00	12.00	31.00	20.46	40.99
47092	17.85	36.23	1.00	4.25	12.25	31.50	20.45	40.93
	17.98	36.23	1.5	4.1	12.1	31.3	20.46	40.96
	54.21		**5.6**		**43.4**		**60.42**	

Table 6.3: Pause *and* Resume *transistion durations of various components of the two performed* `AlertTestSinglePE` *runs. The second last line shows the averages for the particular columns and the last line gives the average total reaction time for every component.*

Table 6.3 shows the duration data for the two `AlertTestSinglePE` runs carried out in the test period. The columns regarding processes from the `CT` Contexts are again averaged over all four telescopes. In this process, the values for the *CameraTriggers* and the *CameraHVs* were only accurate within 1 s. As the transition durations for *CameraTriggers* are not expected to change, the small deviation of the average Resume duration of the *CameraTriggers* from the values of the previous test runs are probably only caused by this inaccuracy. As expected, the durations for the *CameraReaders* were again 0.00 s for all instances without exception and are therefore omitted.

It can be seen here, that the HV *Controllers* needed around 12 s to reduce the HV to a subcritical value and with ≈ 32 s nearly three times as long to turn it on again. Because the *CameraHV* subprocesses are dependent on the according *CameraTrigger* subprocesses, which themselves are again dependent on the *Connectors*, the Pause and Resume durations for the whole `CT` contexts are a few seconds longer and together needed around 55 s. For the whole `SubArray` Context, another 6 - 7 s of overhead resulted in a total reaction time of slightly over a minute for the `AlertTestSinglePE` run type.

6.2 Summary of Speed Results

The results on the total reaction durations obtained from the various simulated alert runs make it possible to give a good estimation of how long the reaction time to a GRB alert would be under realistic conditions.

From the transition duration of the `AlertTestSinglePE` runs, it can be concluded that the high voltage, trigger and readout systems of the telescope cameras will alone need around 61 s. This time already includes a duration overhead of 6-7 s, which comes from further involved processes not addressed in the previous Sections, e.g. from the *Receivers* in the `SubArray/Receiver` Context, which will all close and reopen their files during the alert transitions.

In a real alert run, the dependency scheme will force the alert stopping, i.e. the invoking of the PAUSE transition, of the involved processes in a certain order:

1. *Connector* (very fast)
2. *CameraTriggers* (1 - 2 s)
3. *CameraHVs* (around 12 s)
4. *Tracking* (22 - 30 s overhead + 0.65 s/deg)

The above list comprises the most time consuming elements, as most other processes will do the transition simultaneously and sufficiently fast. Nevertheless, they contribute to the total duration with around 6 - 8 s because of the way the *Managers* handle the dependency scheme adherence. This will be further discussed in the conclusion.

When the system has reached the PAUSED state, the high voltage is at a safe value of 400 V and the telescopes are on target. After that the RESUME transition is invoked on all involved processes and the list above is traversed in the opposite direction. Here, the *CameraTriggers* needs 5-6 s and the high voltage, which has to be raised slowly, around 32 s, while the telescope tracking *Controllers* and the *Connector* will do their transitions without delay.

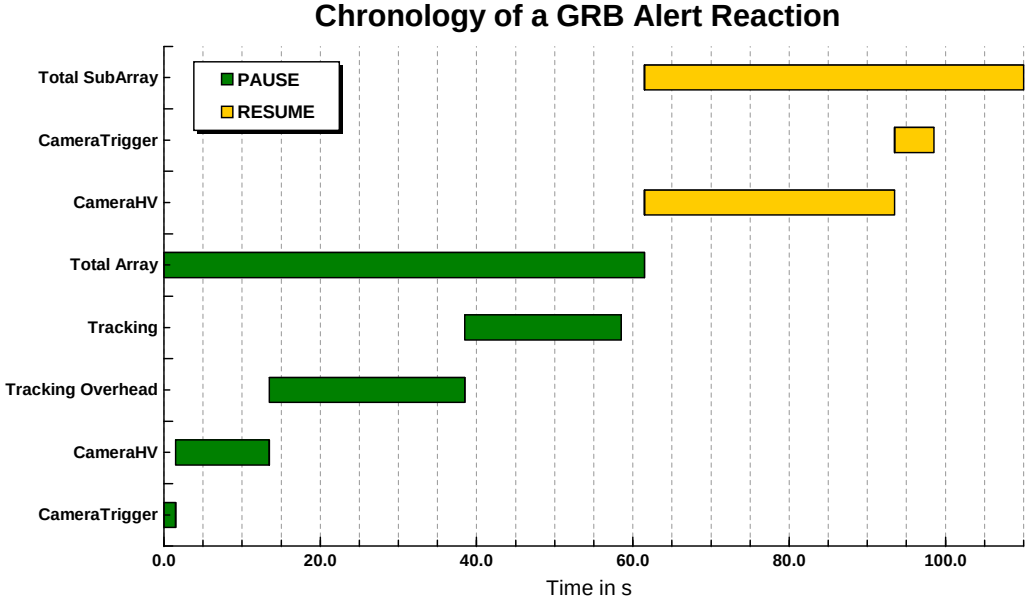

Fig. 6.5: *Chronology of a GRB alert reaction. The green bars represent the* PAUSE *and the orange the* RESUME *transition durations of the described processes.*

The floating bar chart in Figure 6.5, which shows the transition durations for the most

time consuming components, summarizes the above described chronology of the alert reaction. In the graph, it is assumed that the GRB occurred at an angular distance of around 33°, which would entail a pure telescope slewing duration of approximately 20 s. Furthermore, the tracking overhead has been set to a value of 25 s, half of which is the configuration time of the telescope drive system, while the other half is for fine positioning. Lastly, the PAUSE and RESUME times for the total subarray have been set to exceed all displayed transition times by 3 s and 4 s respectively in order to accommodate for the additional duration overheads observed in the test runs conducted.

From the example in Figure 6.5, which has been generated from the transition durations of the simulated alert runs, it can be concluded that the GRBARS has a minimal total alert reaction time of 80 s, if the telescopes are not already on target. In the latter case, the tracking overhead is much lower[4] and would make a total reaction time of under 70 s possible. Depending on the angular distance of the GRB, the slewing time of the telescopes has to be added to this minimal time. As GRBs with zenith angles above 45° would not be observed in a prompt reaction and normal observation is also rarely done with higher zenith angles, the worst possible angular distance would be 90°, resulting in a total slewing time of ≈ 56 s and a thus total reaction time of ≈ 136 s. The more average example shown in Figure 6.5 ends up in a total duration of 102 s.

[4] see Figure 6.1

7 Conclusion and Outlook

In this work, the integration of an automatic response system to gamma-ray burst alerts to the data acquisition software of the H.E.S.S. telescope system has been described in detail, alongside with an introduction to the phenomenon of GRBs. It has been shown, that the alert system works stable when operated with combinations of the individual hardware subcomponents of the telescope array. Due to the lack of granted observation time during the implementation of the system, a complete test of all hardware components under realistic conditions was unfortunately not possible. As, however, all necessary components have been tested individually, the systems is very likely to function also in a real alert observation run, which will be tested in the near future.

The current reaction time of the GRB alert system in the order of 100 s is likely to be significantly reduced by later optimizations which could not be implemented during the course of this work due to timing reasons. A list of possible optimizations is given in the following.

- The proper implementation of an immediate alert shutdown of the camera high voltage supply would reduce the PAUSE duration of the high voltage *Controller* from 12 s to almost zero.
- Code optimizations in the tracking *Controller* could reduce the time, that is needed to configure the drive system in case of an alert. Additionally, the fine-positioning of the telescopes could be omitted in case of a GRB alert, because the error boxes provided by Swift and other Satellites are typically much larger than the gained precision.
- The way the *Managers* enforce the dependency scheme and invoke their processes' state transitions could be improved. At the moment, the *Managers* only check the status of invoked transitions once per second. Furthermore, when a process cannot be started because another process it depends on is still in transition, the status of the first process is also only checked once per second. For the large number of transitions commenced during an alert observation, this can easily build up to a sizable overhead. As a possible solution, the mentioned waiting times could be reduced to a smaller value.
- The dependency scheme used during alerts could be changed in a way that would allow the simultaneous invocation of the PAUSE transitions of both the *CameraHV* and the *Tracking*, provided that the high voltage can be shut down in the time the tracking still needs for its initial configuration, during which no slewing is done.

Another advancement to the alert system comes with the recent start of the state-of-the-art gamma-ray observation satellite Fermi, which is already connected to the GCN and will soon distribute GRB alerts detected with all instruments. As a consequence, the annual number of observed GRBs will rise, increasing the number of GRBs observable with the H.E.S.S.. A small change in the filter criteria of the *GCN-Alerter* is the only thing necessary to permit a reaction to Fermi alerts. Finally, the usability of the alert response system is not limited to GRB alerts alone, as it has been designed for flexibility from the beginning. In the future, other types of alerts could be reacted on, e.g. when an AGN is flaring or a source shows a sudden change in flux.

8 Bibliography

[1] R. C. Hartman, D. L. Bertsch, S. D. Bloom, et al. The Third EGRET Catalog of High-Energy Gamma-Ray Sources. *ApJS*, 123:79–202, July 1999.

[2] R. W. Klebesadel, I. B. Strong, and R. A. Olson. Observations of Gamma-Ray Bursts of Cosmic Origin. *ApJ*, 182:L85+, June 1973.

[3] J. van Paradijs, P. J. Groot, T. Galama, et al. Transient optical emission from the error box of the γ-ray burst of 28 February 1997. *Nature*, 386:686–689, April 1997.

[4] T. J. Galama, P. J. Groot, J. van Paradijs, et al. GRB 970508. *IAU Circ.*, 6655:1–+, May 1997.

[5] R. Sari, T. Piran, and J. P. Halpern. Jets in Gamma-Ray Bursts. *ApJ*, 519:L17–L20, July 1999.

[6] C. Kouveliotou, S. E. Woosley, S. K. Patel, et al. Chandra Observations of the X-Ray Environs of SN 1998bw/GRB 980425. *ApJ*, 608:872–882, June 2004.

[7] N. Caldwell, P. Garnavich, S. Holland, T. Matheson, and K.Z. Stanek. GRB 030329, optical spectroscopy. *GCN GRB Observation Reports*, 2053, March 2001.

[8] T. Matheson, P. Garnavich, E. W. Olszewski, et al. GRB 030329: Supernova Confirmed. *GCN GRB Observation Reports*, 2120, March 2003.

[9] P.W. Schnoor, D.L. Welch, G.J. Fishman, and A. Price. GRB 030329 observed as a sudden ionospheric disturbance (SID). *GCN GRB Observation Reports*, 2176, March 2003.

[10] K. Pedersen, Á. Elíasdóttir, J. Hjorth, et al. The Host Galaxy Cluster of the Short Gamma-Ray Burst GRB 050509B. *ApJ*, 634:L17–L20, November 2005.

[11] G. Tagliaferri, L. A. Antonelli, G. Chincarini, et al. GRB 050904 at redshift 6.3: observations of the oldest cosmic explosion after the Big Bang. *A&A*, 443:L1–L5, November 2005.

[12] S. Campana, V. Mangano, A. J. Blustin, et al. The association of GRB 060218 with a supernova and the evolution of the shock wave. *Nature*, 442:1008–1010, August 2006.

[13] J. S. Bloom, D. A. Perley, W. Li, et al. Observations of the Naked-Eye GRB 080319B: Implications of Nature's Brightest Explosion. *ArXiv e-prints*, 803, March 2008.

[14] W. S. Paciesas, C. A. Meegan, G. N. Pendleton, et al. The Fourth BATSE Gamma-Ray Burst Catalog (Revised). *ApJS*, 122:465–495, June 1999.

[15] C. Kouveliotou, C. A. Meegan, G. J. Fishman, et al. Identification of two classes of gamma-ray bursts. *ApJ*, 413:L101–L104, August 1993.

[16] J. P. Norris, R. J. Nemiroff, J. T. Bonnell, et al. Attributes of Pulses in Long Bright Gamma-Ray Bursts. *ApJ*, 459:393–+, March 1996.

[17] D. Band, J. Matteson, L. Ford, et al. BATSE observations of gamma-ray burst spectra. I - Spectral diversity. *ApJ*, 413:281–292, August 1993.

[18] J. Hjorth, D. Watson, J. P. U. Fynbo, et al. The optical afterglow of the short γ-ray burst GRB 050709. *Nature*, 437:859–861, October 2005.

[19] D. A. Frail, E. Waxman, and S. R. Kulkarni. A 450 Day Light Curve of the Radio Afterglow of GRB 970508: Fireball Calorimetry. *ApJ*, 537:191–204, July 2000.

[20] G. Cavallo and M. J. Rees. A qualitative study of cosmic fireballs and gamma-ray bursts. *MNRAS*, 183:359–365, May 1978.

[21] T. Piran. Gamma-ray bursts and the fireball model. *Phys. Rep.*, 314:575–667, June 1999.

[22] M. J. Rees and P. Meszaros. Unsteady outflow models for cosmological gamma-ray bursts. *ApJ*, 430:L93–L96, August 1994.

[23] P. Meszaros and M. J. Rees. Relativistic fireballs and their impact on external matter - Models for cosmological gamma-ray bursts. *ApJ*, 405:278–284, March 1993.

[24] UK Swift Science Data Centre. `http://www.swift.ac.uk/grb.shtml`, 2008.

[25] J. S. Bloom, S. R. Kulkarni, and S. G. Djorgovski. The Observed Offset Distribution of Gamma-Ray Bursts from Their Host Galaxies: A Robust Clue to the Nature of the Progenitors. *AJ*, 123:1111–1148, March 2002.

[26] E. Berger, P. A. Price, S. B. Cenko, et al. The afterglow and elliptical host galaxy of the short γ-ray burst GRB 050724. *Nature*, 438:988–990, December 2005.

[27] S. E. Woosley. Gamma-ray bursts from stellar mass accretion disks around black holes. *ApJ*, 405:273–277, March 1993.

[28] A. I. MacFadyen, S. E. Woosley, and A. Heger. Supernovae, Jets, and Collapsars. *ApJ*, 550:410–425, March 2001.

[29] Z. B. Etienne, J. A. Faber, Y. T. Liu, et al. Fully general relativistic simulations of black hole-neutron star mergers. *Phys. Rev. D*, 77(8):084002–+, April 2008.

[30] R. C. Duncan and C. Thompson. Formation of very strongly magnetized neutron stars - Implications for gamma-ray bursts. *ApJ*, 392:L9–L13, June 1992.

[31] K. Hurley, S. E. Boggs, D. M. Smith, et al. An exceptionally bright flare from SGR 1806-20 and the origins of short-duration γ-ray bursts. *Nature*, 434:1098–1103, April 2005.

[32] B. D. Metzger, E. Quataert, and T. A. Thompson. Short-duration gamma-ray bursts with extended emission from protomagnetar spin-down. *MNRAS*, 385:1455–1460, April 2008.

[33] W. Heitler. *Quantum Theory of Radiation*. Dover Press, 3rd edition, 1954.

[34] D. Berge. *The gamma-ray supernova remnant RX J1713.7-3946 with H.E.S.S.* PhD thesis, Ruperto-Carola University of Heidelberg, February 2006.

[35] K. Bernlöhr. CORSIKA and sim_ hessarray – Simulation of the Imaging Atmospheric Cerenkov Technique for the H.E.S.S. Experiment. *H.E.S.S. Internal Notes (unpubl.)*, April 2002.

[36] J. Davies and E. Cotton. Design of the quartermaster solar furnace. *Journal of Solar Energy*, 1:16–22, April 1957.

[37] S. Funk, G. Hermann, J. Hinton, et al. The trigger system of the H.E.S.S. telescope array. *Astroparticle Physics*, 22:285–296, November 2004.

[38] H. E. S. S. Collaboration. Calibration of cameras of the H.E.S.S. detector. *Astroparticle Physics*, 22:109, 2004.

[39] H. E. S. S. Collaboration. Observations of the Crab nebula with HESS. *A&A*, 457:899–915, October 2006.

[40] A. M. Hillas. Cerenkov light images of EAS produced by primary gamma. In F. C. Jones, editor, *International Cosmic Ray Conference*, volume 3 of *International Cosmic Ray Conference*, pages 445–448, August 1985.

[41] T.-P. Li and Y.-Q. Ma. Analysis methods for results in gamma-ray astronomy. *ApJ*, 272:317–324, September 1983.

Danksagung

Bei der Entstehung dieser Arbeit habe ich von vielen Verwandten, Freunden und Kollegen Unterstützung erhalten, weswegen ich mich auf diesem Wege bei allen Beteiligten für ihre Hilfe und Geduld bedanken möchte.

Besonderer Dank gilt hierbei:

- Meinem Betreuer Prof. Christian Stegmann, der auch im Urlaub nicht vor stundenlangen gemeinsamen Software-Debugging-Sitzungen zurückgeschreckt ist und mir dieses interessante Thema erst ermöglicht hat.
- Ira Jung, die sich auch kurz vor Abgabe noch die Zeit zum Korrekuturlesen genommen hat und verantwortlich ist für viele Verbesserungen.
- Fabian Schöck für das schnelle und engagierte Korrekturlesen dieser Arbeit und für seine vielen hilfreichen Vorschläge.
- Athina Meli, die mir bei der Durchsicht des GRB Kapitel ihr Fachwissen zur Verfügung stellte.

Erklärung

Hiermit bestätige ich, dass ich diese Arbeit selbstständig und nur unter Verwendung der angegebenen Hilfsmittel angefertigt habe.

Erlangen, den 20. Oktober 2008

(Tristan Nowak)